The Effects of Microstructural Features and Process Parameters on the Hot Tearing in Direct Chill Cast Aluminum Alloys

by

M.A.M. Nasim Jamaly

B.Sc, Materials & Metallurgical Engineering, Bangladesh University of Engineering and Technology, 2008

A THESIS SUBMITTED IN PARTIAL FULFILLMENT
OF THE REQUIREMENTS FOR THE DEGREE OF

Master of Applied Science

in

The College of Graduate Studies

(Mechanical Engineering)

THE UNIVERSITY OF BRITISH COLUMBIA

(Okanagan)

September 2012

Abstract

Hot tearing is an irreversible failure that occurs above the the solidus temperature of an alloy during casting, in the presence of a liquid phase. These cracks possess serious quality implications in industrial direct chill (DC) casting process. During solidification, thermal stresses are induced due to the heterogeneous temperature distribution, which causes variations in thermal strain and may result in cracks if these stresses are large enough. In order to investigate the occurrence of hot tears in DC casting, a DC casting finite element process model for round billets was incorporated with (1) a new semi-solid constitutive law for aluminum alloy AA5182 that takes into account cooling rate, grain size and porosity, and (2) a model for cooling rate induced grain size variation. A hot tearing index was calculated from the semi-solid strain predictions from the model. This hot tearing index, along with semi-solid stress predictions from the model, was used to link hot tearing with microstructural features (i.e. grain size and coalescence temperature) as well as process parameters (e.g. casting speed). It was found that grain refinement plays an important role in the formation of hot cracks. In addition, lower assumed coalescence temperature and slow casting speeds were found to improve hot tearing resistance. In addition to simulation of DC casting, experimental studies on an as cast AA5182 ingot (DC cast) were made in terms of grain size, chemical composition and solidification kinetics. Samples for these experiments were collected from the steady state region of the ingot. The results of these experimental investigations show that, (1) grain size increases from surface to centre of the ingot, (2) there is considerable macrosegregation of the alloying elements along the cross section of the ingot, and (3) the solidification kinetics

vary as a function of both position and cooling rates. These experimental observations influence the hot tearing susceptibility of the DC cast product. Thus, for the process model to be more accurate in predicting hot tears, inclusion of these factors, along with an improved model for grain size variation is suggested.

Table of Contents

List of Tables

List of Figures

Acknowledgments

Chapter 1

Introduction

1.1 Aluminum Alloys

Aluminum is the most abundant metal found in the earth's crust. Despite its apparent availability, it was not one of the early metals used by humankind, since it is always found as a compound with oxygen in nature, owing to its high chemical reactivity. Industrial refinement of aluminum began in the late 1800's when Charles Hall in USA and Paul Heroult in France independently developed an electrolytic process for transforming alumina to elemental aluminum. This process, known as the Hall-Heroult Process, is still used today. The main cost when producing Al is the cost of electricity, as it consumes 500 Kilo-Watts per kg, enough to power 5 standard households for a day. As aluminum can be reprocessed effectively several times without deteriorating its properties too much and the cost of producing recycled metal is only 5% as compared to virgin ore, it is only desirable to recycle aluminum. The additional pressures related to sustainable industrial practices also make recycling of Al quite desirable. Consequently, the amount of aluminum recycled has more than doubled between the early 1990's to 2005 (EAA 2005).

Aluminum alloys demonstrate good physical properties such as electrical and thermal resistance. However, the most important properties of Al are its lightness (density of 2.7 g/cc, whereas steel has 8 g/cc) and high specific strength. Its lower density,

good corrosion resistance, along with moderate mechanical properties (such as the tensile strength and elastic modulus) have enhanced the use of aluminum and its alloys in many applications over the past few years. Currently, the use of aluminum alloys in the automotive, rail, marine and aerospace transportation industries occupy the majority of the total usage of aluminum around the world (about 36%) (EAA 2005). Aluminum alloys are especially appreciated in the transportation industries due to their low density, corrosion resistance, shock absorption capabilities, and strength.

1.2   Fabrication of Aluminum Components

Based on their fabrication method, aluminium alloys are classified into two principal groups: cast alloys and wrought alloys. Cast alloys are used in processes where the liquid metal is directly solidified in a mold that is similar in geometry to the end use component. Cast aluminum alloys, such as A356 (Al - 7%Si) have properties such as a low melting point, high fluidity, and attractive as-cast solidified structures. The advantages of this process are: (1) it can produce finished or nearly finished products; (2) it is suitable for complex geometries; (3) it is economical for both small and large number of parts.

On the other hand, wrought alloys are those that are shaped for use by plastic deformation through rolling/forging/extrusion etc. Wrought alloys are suitable for components with simple geometry, such as blocks, sheets and wires. The relevant forming techniques requires the wrought alloys to be designed to have attractive mechanical properties, such as low yield strength in the as-cast state, high ductility, good fracture resistance, and excellent strain hardening. Wrought aluminium is also produced as $Alclad_{TM}$ material, in which a thin layer of corrosion resistant commercial purity aluminium is bonded to one or both surfaces of a high strength alloy during rolling and the material is further processed as a composite. Aluminum alloys of series 1xxx, 2xxx, ..., 7xxx are examples of wrought alloys.

1.3   DC Casting of Aluminum Alloys

As was discussed in the previous section, components made from wrought aluminum alloys need to go through some sort of deformation processing to create their final shape. The primary input for these processes are aluminum alloy as-cast billets (cylindrical shape, typical dimensions of $L = 10$ m, $D = 50$ cm) and sheet ingots (rectangular cross section, typical cross-sectional dimensions of 2 m $\times$ 1 m), i.e. castings with at least one plane of symmetry. Wrought aluminum alloy billets and ingots must possess a constant cross section, have good surface quality and be defect free in order to produce high quality products in downstream processes. Since the 1940's, the standard technique for producing wrought aluminum alloys has been the semi-continuous Direct-Chill (DC) casting process (Emley 1976, Stefanescu 1988). In figure 1.1, DC cast billets and ingot are shown.

In the DC casting process, a mold consistent with the desired cross section shape is paired with a vertically movable starter block at the bottom. Sometimes, the mold is covered with a hot-top to alter the cooling conditions. A schematic of the typical DC casting process is shown in figure 1.2. The process is as follows. First, the alloy is melted in a holding furnace and the molten metal is poured into the closed space created by the bottom block and the mold. Grain refiners are added to control the final microstructure. Second, the molten metal solidifies in contact with the mold and the bottom-block to form a solid shell. Third, once the solid shell has achieved sufficient strength to support the liquid pool, the bottom block is moved downwards with a velocity generally referred to as the casting speed. Molten metal is continuously fed into the mold from the top. The casting speed may be constant over the whole process, or it may vary with time. Finally, once the casting has reached the desired length, the casting velocity is reduced to zero and the billet/ingot is allowed to fully solidify. It is then removed from the casting pit and the process is started again.
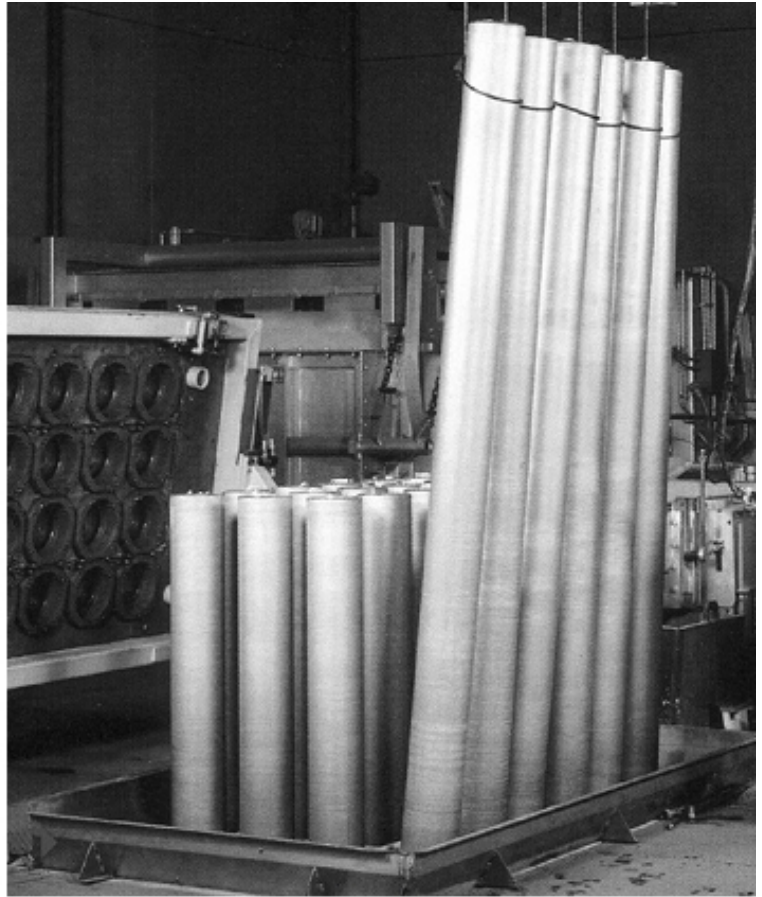
Figure 1.1: DC casting process for production of (a) ingots; (b) billets (Grasso 2004)

From a phenomenological stand point, the process can also be divided into three regions. In the "start-up phase", there exists a thermal field throughout the casting. In this stage, the thermal fields are not yet stationary but vary both with position and with time. The "steady state" is achieved after the casting length has reached about 0.5 m, and is characterized by thermal fields that are constant with respect to position. After this, the casting can be continued for several metres with good casting quality. In the "final stage", the thermal fields again become transient as the feeding is stopped and the bottom block is arrested.
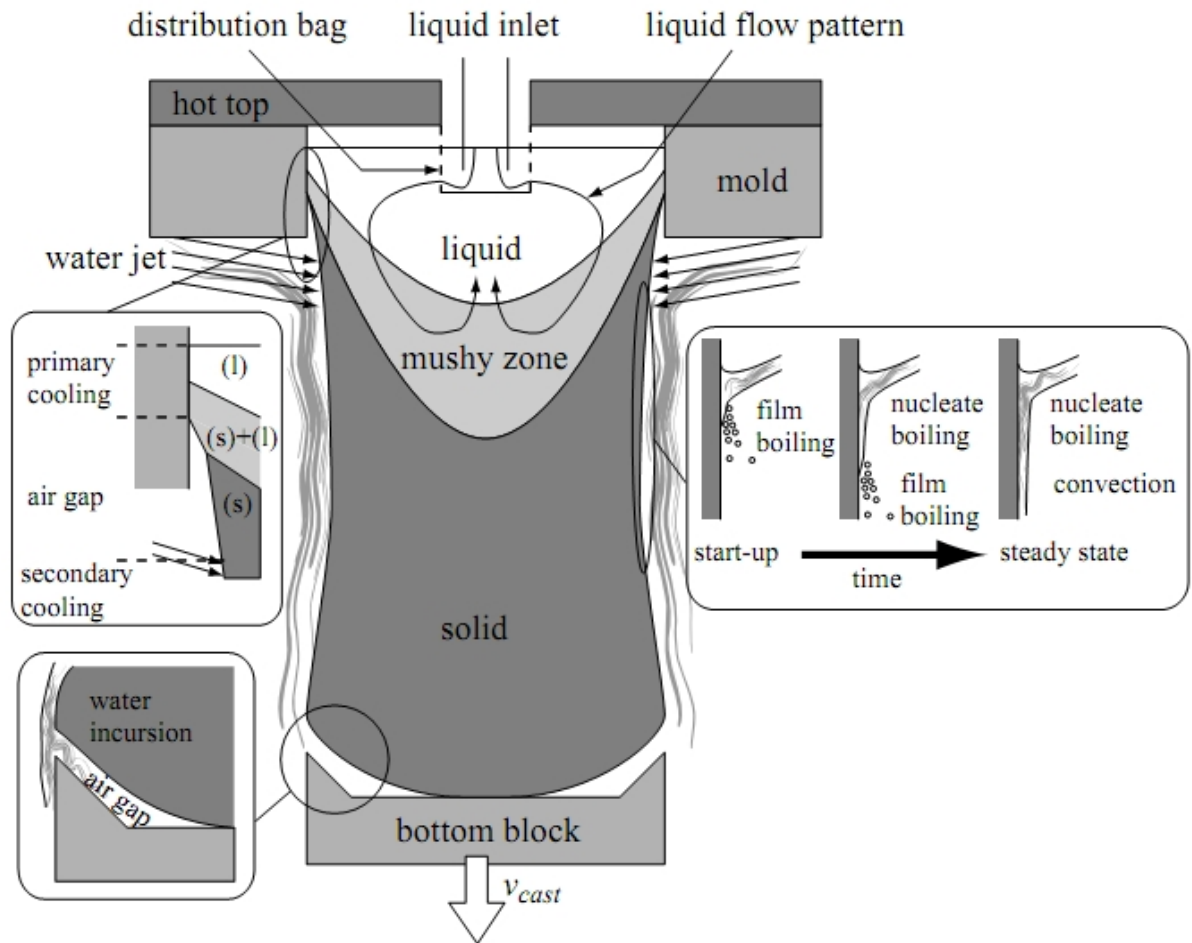
Figure 1.2: Schematic representation of the DC casting process (Larouche et al. 1998)

Although the DC casting process has gone through numerous optimizations over the years (Emley 1976), it remains identical in principle to the original process first introduced in the 1940's. One of the important features of the DC casting process is the differential cooling conditions experienced by the cast surface as it descends into the casting pit (Sengupta et al. 2004). Firstly, the casting is in contact with the mold and heat is extracted at a high rate from the molten metal. The cooling of metal from direct contact with the mold is termed primary cooling. As the metal solidifies, it then shrinks due to thermal contraction and consequently loses contact with the mold. Concurrently with the formation of this "air gap", heat transfer is significantly reduced, which may lead to partial re-melting due to heat flow from within the molten metal pool to the surface.

Secondly, the casting is cooled via water sprays below the mold, termed secondary cooling. This cooling can be subdivided into several regimes, depending on the turbulence of the water jets and the temperature of the surface where the water impinges onto the casting (Caron and Wells 2006, Collier and Thome 1994, Larouche et al. 1998, Sengupta et al. 2004). Therefore, the convective heat transfer coefficient (h) at different regimes of primary and secondary cooling will vary considerably. Thirdly, the casting is cooled through the bottom block. As a result of thermal contraction, the contact between the bottom block and the end of the casting is lost close to the ingot lip. In this case, the efficiency of cooling depends on the size of the air gap formed at the bottom block/casting surface. Note that an interesting phenomenon, known as water incursion, may occur if the secondary cooling spray water runs into this air gap (Sengupta et al. 2004). In the ingot case, the heat transfer in this air-gap is strongly affected by the flow of water from the rolling face side. As can be seen, there are complex heat transfer phenomena associated with the DC casting process. An understanding of these processes is crucial for improving casting quality.

1.4   Summary

In this chapter, an overview of aluminum alloys, along with the Direct Chill casting technique used for fabricating wrought alloys, has been presented. Now, it is worthwhile to mention that the DC casting process is subjected to considerable defects. In fact, many of the high-strength aluminum alloys recently developed to compete against traditional materials are not currently viable due to the high costs associated with defect formation. The current masters project involves the study of the formation of a specific defect, hot tearing, during DC casting through the use of a process model based on finite elements. In the next chapter, relevant literature of this defect and measures taken to minimize it will be discussed in detail.

Chapter 2

Literature Review

2.1 Introduction

In this chapter, an overview of the defects that arise during DC casting is presented. In this discussion of defects, special attention is given to those that form during solidification. An important phenomenon occurring during solidification is the transition from the semi-solid behaving like a liquid to one where the behaviour is like a solid and capable of transmitting long-range stresses. This transition, known as mechanical coalescence, is a large factor influencing the extent to which defects occur. In order to predict and reduce defect formation, computer simulation of the DC casting process has increasingly been utilized over the past few decades. These computer simulations are termed process models. The past research and present trends of the development of these DC casting process models and associated topics available in the published literature is critically reviewed. Now, the mechanical behavior of the alloy during solidification is the most important matter to understand for study of defect formation during solidification. Models developed by researchers for semi-solid mechanical behavior of aluminum alloys are thus discussed in detail, as are the relationships between processing variables and the occurrence between casting defects. Finally, the available defect formation criteria that exist to assess the susceptibility of a casting to the formation of defects are summarized.
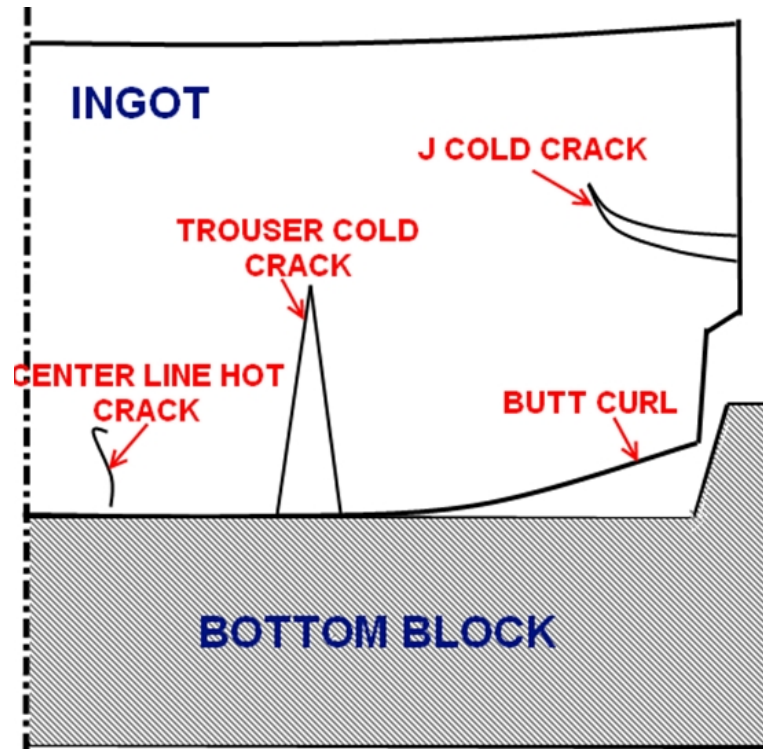
Figure 2.1: Schematic representation of common defects that may arise in a DC cast ingot

2.2   Defects in DC Cast Products

There are numerous defects that may arise during the DC casting process. Some of the industrially relevant defects include: macro / micro segregation, loss of dimensional stability, inclusions, porosity, and the formation of hot tears and cold cracks. Some of the typical defects that can arise in a DC cast ingot are shown schematically in figure 2.1. Hot tearing is a failure that occurs above the the solidus temperature of the alloy, in the presence of a liquid phase. Conversely, cold cracking is a failure that occurs below the solidus temperature. The cooling of the billet in the DC casting process is achieved mainly by the cooling water jet and partially by the bottom block. These differential cooling conditions at different locations of the billet results in dissimilar contraction and ultimately causes thermal stresses to arise within the billet (Grandfield and McGlade 1996, Yu 2002). Process parameters for DC casting, such as water flow rate (Matsuda et al. 1996) and casting speed (Commet et al. 2003, Matsuda et al. 1996) can exacerbate

8

the cold cracking problem by modifying the thermal stress levels in the billet. Other factors that can affect the cold cracking susceptibility are geometry and size of the billet (Grandfield and McGlade 1996). Loss of dimension of the billet bottom (butt curl) and appearance of surface cracks are also considered to be due to the aforementioned thermal stress, particularly in the 'start-up phase' of the casting process. The stress levels in the start-up phase are a strong function of the shape of the bottom block (Benum et al. 2002). Droste et al. (2002) experimentally measured butt curl in DC casting and found that butt curl increases when the border area of the tail of the billet is cooled by water jet (secondary) cooling. Experimental quantification of butt curl in DC casting of alloy AA5182 by Sengupta et al. (2004; 2005a) revealed that increasing the water flow rate increased distortions of the ingot-base and vice versa.

The variation of chemical composition along the cross-section of the DC cast billet, or macrosegregation can be both positive (increasing solute content from surface to center) or negative. The incipience of grain cells close to the centerline of the billet is attributed to the centerline or negative macrosegregation (Eskin and Katgerman 2009). Low casting speeds enhance positive segregation in DC cast billet, independent of its size (Eskin and Katgerman 2009). Moreover, billets can be cast at higher speeds with positive segregation, if a proper level of grain refinement is ensured (Eskin et al. 2008).

The present study is related to the defect known hot tearing or solidification cracking. A brief overview of the hot tearing defect within the context of DC casting is presented below.

2.2.1 Hot tearing in DC casting

Hot tearing is one of the key defects that may arise during DC cast aluminum alloys. During solidification, thermal stresses are induced due to the heterogeneous temperature
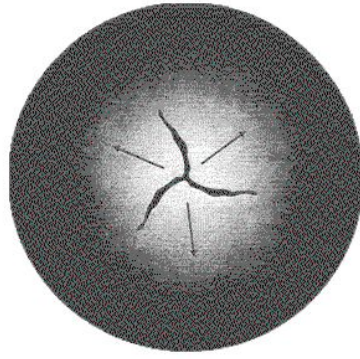
Figure 2.2: Hot tearing crack at the centre of a DC cast AA6063 billet (star crack) (Thevoz et al. 2002)

.

distribution, which causes variations in thermal strain and may result in cracks if these stresses are large enough (Drezet and Rappaz 2001, Drezet et al. 1996a, M'Hamdi et al. 2002, Sengupta et al. 2004). Hot tearing occurs not only in DC casting but in other casting processes including shape casting and welding as well. Example of a hot tearing defect is shown in figure 2.2. In these cases, the cracked section of the billet must be cut off before the casting can be used for subsequent deformation processing. Often, the formation of a hot tear leads to component rejection. So, if present in any extent, hot tearing will substantially reduce productivity. Campbell (1991) describes the salient features of hot tearing as follows:

1. Hot tears are found often in the hot spots of the casting or at locations where strains are concentrated.

2. Hot tears mainly propagate in an inter-granular fashion.

3. Hot tears visually appear to be ragged and branching cracks.

4. The onset and extent of hot tearing may vary even if the processing conditions are kept constant.

Hot taering is closely linked to semi-solid ductility. Since the early 1950's, researchers have been experimentally measuring semisolid ductility, with the finding that there is
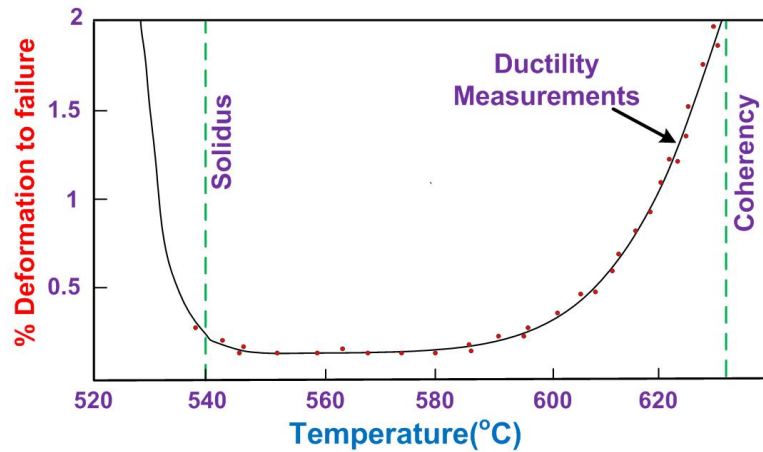
Figure 2.3: Ductility in the semi-solid state for an Al-4.5%Cu alloy, after Magnin et al. (1996)

a critical temperature range in the semi-solid region where the ductility of the alloy is extremely low. For example, Singer and Cottrel (1946) showed that Al-Si alloys exhibit a sharp decline in ductility at just above T_{sol} and a corresponding change in morphology of the fractograph. In the same year, Pellini studied the solidification of aluminum and steel plates and reported a steep decline in ductility just above T_{sol}. Later, Magnin et al. (1996) executed tensile tests for an Al-Cu alloy in the semi-solid state for a range of temperatures between solidus and the mechanical coherency point. It was observed that there is a brittle temperature range, between 540 and 580°C where the ductility of the alloy is virtually zero as shown in figure 2.3. Similar observations were made by Zhi-ming et al. (2010), on a study focused on the as-deformed A250 aluminum alloy, but within the context of semi-solid processing.

More recently, Twite et al. (2004) conducted tensile tests on AA6061 alloys in the semi-solid regime, and found that the tensile strength of the alloy dropped to zero between 560-570°C, depending on the source of the alloy. In the same year, Colley et al. (2004) conducted tensile tests on alloy AA5182 at high temperatures (500 - 580°C) to determine mechanical properties of the alloy in the semi-solid state. These tensile tests revealed that, in the semi-solid state, ductility of the alloy decreases sharply at around a volume

fraction solid (f_s) of 0.95. Moreover, the f_s at which the alloy looses its ductility is strongly dependent on the applied strain rate, a conclusion drawn by both Colley et al. (2004) and Twite et al. (2004). Haaften et al. (2002) also conducted semi-solid regime tensile tests on alloy AA5182 and AA3004 in the as cast state. They also observed the strain rate sensitivity on the tensile strength, and found that strength dropped to a very small value above 550°C. From the works of Singer and Cottrel (1946), Pellini (1952), Magnin et al. (1996),Van Haaften et al. (2002), Colley et al. (2004), Twite et al. (2004), Zhi-ming et al. (2010), it is evident that in aluminum alloys, there is a range of temperature at the semi-solid state where the ductility/strength of an alloy in minimum. In DC casting, as previously discussed, thermal stresses are generated due to differential cooling conditions experienced by different parts of the casting billet. If these stresses are high enough at the low ductility/strength range in the semi-solid state, cracks may appear. These cracks are termed hot cracks if they have first appeared in the semi-solid regime.

2.3   DC Casting Process Models

DC cast products encounter numerous solidification defects. In order to increase productivity and reduce scrap, these defects must be properly understood. The study of solidification defects in DC casting is generally simulated with small scale experiments within the laboratory. But it is challenging to compare the results obtained from these simulations with the industrial scale, simply because factors causing solidification defects are sensitive to casting geometry and processing conditions. Another choice is to study solidification defects in-situ during production. But performing hot tearing experiments on an industrial scale by 'playing' with the process parameters is time consuming and expensive.

The limitations concomitant with the experimental work has necessitated the development of DC casting process models. Using the finite element (FE) method, researchers

can estimate both the thermal field and stress-strains in the cast body throughout the casting process. Well described and experimentally validated models allow one to vary the process parameters within the model domain. The effect of changes in casting parameters can then be understood by observing the changes in the predicted stress, strain and temperature contours given by the model. The evolution of stresses and strains at different location of the casting can be used to develop an idea of when and where the defects (e.g. hot tearing) may occur.

Many researchers have worked extensively on developing DC casting thermal and stress models for aluminum alloys. Most of these efforts have focused on only one aspect of the DC casting process, either the thermal, e.g. (Sengupta et al. 2001; 2003) or thermo-mechanical analysis, e.g. (Drezet et al. 1996a). Also, the models have been mainly one-dimensional, e.g. M'Hamdi et al. (2002) or axi-symmetric (Weckman and Niessen 1982), although the process model developed by Sentupta was three-dimensional. In order to simplify the simulation, most researches focused on round-shaped and small billets.

In one of the earliest works on process models, Weckman and Niessen (1982) used the thermocouple data of DC cast AA6063 ingots to develop a thermal model of DC casting. They observed that the use of a set of previously determined effective heat transfer coefficients in the model induces errors in predicted temperature profile. They combined the existing nucleate boiling, forced convection and film boiling heat transfer concepts to propose a novel routine for defining boundary conditions for surface regions of the ingot below the mold cooled by a water stream running down the surface. A thermomechanical DC casting process model for alloy A6063 was proposed by Fjaer and Mo (1990). In this work, residual stresses generated after the ingot has been cooled was calculated and these values were shown to agree quantitatively with the available data in the literature.

Wiskel and Cockcroft (1996) used one-dimensional and two-dimensional thermal mod-

els to investigate heat flow within the casting. They showed that their simulations could generate cooling curves that conform well with the known cooling curves of the system, through a validation against experimentally-obtained data from an industrially cast AA5182 sheet ingot.

In the 1990's, Drezet and colleagues developed finite element thermomechanical models of DC casting to forecast dimensional instability of ingots (Drezet and Rappaz 1996a) and influence of mold shape on ingot distortions (Drezet et al. 1996b). Experimental work to determine the alloy thermophysical properties and to fine tune the boundary conditions for these models were carried out during this time (Drezet et al. 2000b). These models (Drezet and Rappaz 1996a, Drezet et al. 1996a;b) were validated by comparing the results from these models with experimental data (Drezet et al. 1995).

Sengupta et al. (2004) proposed a comprehensive three dimensional FE thermal model containing phenomena including primary cooling at the mold, secondary cooling by water jet, and cooling by the bottom-block during the startup phase of the DC casting process. This work considered the air gap formation between the ingot and the bottom block due to thermal contraction at the base of the casting, and entrapment of water into these air gaps dripping from the surface of the ingot (termed water-incursion). The model was extensively validated by comparing the predicted temperature evolutions with thermocouple measurements made in the full scale industrial DC casting experiments. In a companion work (Sengupta et al. 2005a), the stress-strain simulation was validated by comparing the amount of base deformation known as "butt curl" with the same quantity in the model. Good agreement was found between the two results.

Further work was done to develop industrially-relevant process models of DC casting by Grealy et al. (2001), who proposed methods for optimization of the metal distribution system, solidification, and heat transfer mechanism in large commercial ingots. This work

demonstrated that such models have also found frequent use in industrial practice, in addition to being an academic exercise. Williams et al. (2003) presented a three dimensional DC casting model for AA1201 alloy. Their model was a multi-physics model since melt flow, stress and heat transfer were coupled for early stages of DC casting. On the other hand, the majority of the literature relating to DC casting process simulations relates to thermo-mechanical models, where the fluid flow is ignored and the mush is considered as a solid body of lower strength. The major weakness of Grealy's model was that it was not experimentally verified. They also used an idealized bottom block shape and thus the predicted butt curl appears to be underestimated, contrary to the work of Sengupta et al. (2004). In the model developed by Bagnoud and Plata (2000), the discrepancy in the results with regards to butt-curl (as compared to Sengupta et al. (2004)) is probably related to their assumption of ideal plasticity as the effect of strain hardening is ignored.

More recently, Drezet and Phillion (2010) developed an 2D axi-symmetric billet model to estimate residual stresses in billet. They used the POLDI neutron diffraction (ND) facility at the Paul Scherrer Institute in Villigen, Switzerland, to estimate the residual stresses in an industrially cast AA6061 billet, and found a fairly good agreement between the predicted and the measured values. Similar experimental work was performed by Hao et al. (2010) to validate a DC casting process simulation of Mg alloy AZ31. The results indicate that the stress-strain predictions show the same trend as the residual strain measurements using neutron diffraction techniques.

From the above references, it has been found that the research community has been able to develop a series of DC casting simulations which are capable of predicting the evolution in thermal and displacement fields during industrial processing. To some extent, these simulations have been successful in also predicting casting defects such as ingot distortions (Drezet and Rappaz 1996a, Drezet et al. 1996a;b), butt curl (Sengupta et al. 2004; 2005a), residual stresses (Drezet and Phillion 2010), hot tearing (Suyitno et al.

15

2005), etc. However, much work remains. One of the main challenges in the development of the DC casting process models that are capable of quantitatively predicting defects is a description of the mechanical behavior of aluminum alloys in the semi-solid state.

2.4 Semi-Solid Mechanical Behavior

2.4.1 Concept of Coalescence Temperature

Before discussing the mechanical behavior of aluminum alloys in the semi-solid, it is logical to discuss a very important phenomenon that occurs during the solidification of aluminum alloys, namely mechanical coalescence. This mechanical coalescence happens at a temperature between the solidus and liquidus, and is strongly effected by numerous casting parameters and the composition of the alloy. The mechanical response of semi-solids to applied loads is quite different at temperatures above and below this coalescence point.

The concept of mechanical coalescence can be understood by studying the various stages of solidification in metallic alloys. Clyne and Davies (1981) proposed four stages of solidification of metallic alloys within the semi-solid based on the permeability of the solidifying network - mass feeding, interdendritic feeding, interdendritic separation and interdendritic bridging. These feeding mechanisms are shown in figure 2.4, and further described below:

1. Mass Feeding

   In the mass feeding regime, the microstructure is essentially solid particles contained in liquid, moving freely under mechanical loading and contraction stresses.

2. Interdendritic Feeding

   In this regime, the free movement of the solid is restricted by grain size and shape. The solid loses its ability to move freely in response to mechanical load and the
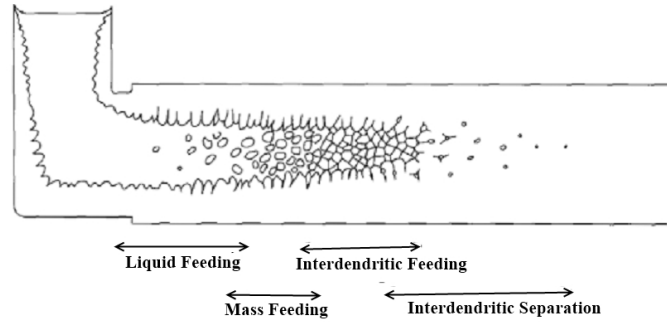
Figure 2.4: Schematic representationist of all 4 feeding mechanisms active within a casting,after Campbell (1991)

remaining liquid is forced to flow through the dendritic network to accommodate stress.

3. Interdendritic Separation

At higher fraction solids, a continuous and interconnected liquid film exists that surrounds the dendrites. Stress is released by the formation of micro-pores and hot-cracks because the dendrites have not yet bridged to take the load and yet the low permeability of the structure prevents liquid flow. The semi-solid is able to transmit stress, but cannot accomodate strain.

4. Interdendritic Bridging

At this terminal stage of solidification, the cast structure attains considerable strength as dendrites bridge and the solid network can transmit long range stresses and strains.

The transition between each of the four stages is generally assumed to be a function of factors including alloy composition, cooling rate, grain shape and grain density. When the solidification process transitions from interdendritic feeding to interdendritic bridging, the dendrite arms tangle with each other to form a continuous solid network. This point, or stage of solidification, is referred to as mechanical coalescence (Backuerud et al. 1990), with the temperature, time, and fraction of solid at this point given the corresponding names coalescence temperature, coalescence time, and coalescence fraction solid (Chai

et al. 1995, Jiang et al. 1999). For the last few decades, the mechanical coalescence has been accepted as a critical characteristic in cast aluminum alloys (Veldman et al. 2001). This transition causes the solid network to attain structural integrity and prohibit mass feeding. As a result, the remaining liquid metal must flow through the solid network of the dendrites to compensate for the solidification shrinkage (Jiang et al. 1999). The combination of applied stress and limited feeding at temperatures below mechanical coalescence can result in a hot tear. At temperatures above mechanical coalescence, the liquid will simply flow in response to the applied load.

2.4.2 Constitutive law: Semi-solid

The constitutive behaviour of semi-solids is complex due to the significant transitions occurring within the permeability of the mushy zone during solidification process as shown in the experimental work presented in section 2.2.1. Modeling the semi-solid constitutive behaviour has always been a challenge to researchers because of the large range of viscosity between $0 < f_s < 1$, and the stochastic nature of the solidification process. As shown in table 2.1, a number of different constitutive laws have been developed for semi-solids. One successful approach, initiated by Drezet and Eggeler (1994), was to use a modified creep law to describe the semi-solid behavior of aluminum alloys. The justification behind using this type of creep law is that at high fraction solid the liquid exists as isolated pockets in-between the continuous solid network. Any mechanical failure is thus almost exclusively dependent on the solid network. Hence, at high fraction solids, the mechanical response of the alloy with increasing temperature would be somewhat like a completely solid body. Consequently, it was assumed that the load is entirely carried by the existing solid network as the liquid can not bear any load. With this in mind, Drezet and Eggeler (1994) proposed that the area of load carrying is proportional to f_s as shown in equation 2.1, where $\dot{\varepsilon}_{min}$ is the minimum creep rate, σ_0 is applied stress, Q is the activation energy for creep, A is a material-dependent constant, T is the temperature, and R is the universal gas constant.

Table 2.1: Summary of semi-solid constitutive laws found in the literature

Proposed by	Alloy system	Features	Equation
Ludwik Equation	N/A	Inclusion of strain harden-ing and high temp creep	2.4
Modified Ludwik Equation	N/A	Introduction of offset con-stants for ease of FE simu-lation	2.13
Haaften et al. (2002)	N/A	Plastic strain based	2.2, 2.3
Ludwig et al. (2005a)	N/A	Accounts for anisotropic be-havior of Semi-solid	2.4
Drezet and Eggeler (1994)	N/A	Creep based law	2.1
Lu et al. (2008a)	Al - Cu	Valid at lower f_s	2.5, 2.6, 2.7
Phillion et al. (2009)	Al - Mg - Mn	Inclusion of microstructural features	2.8 - 2.12

$$\dot{\varepsilon}_{min} = A \left(\frac{\sigma_0}{f_s(T)} \right) exp \left(\frac{-Q}{RT} \right) \tag{2.1}$$

The constitutive relationship by Drezet and Eggeler was refined, in the work of Haaften et al. (2002), by considering the critical term to be $(1 - f_{LGB})$, where f_{LGB} is the fraction of grain boundary area covered by the liquid, instead of the fraction solid term f_s. They argued that the low melting (eutectic) phases present at the grain boundaries are the dominant factor for semi-solid deformation. The proposed law is shown in equation 2.2 and 2.3. In these equations, A, σ_0, and n_H are constants related to material properties and σ_{ss} is the steady state stress.

$$\dot{\varepsilon} = A \left[sinh \left\{ \frac{\sigma_{ss}}{\sigma_0} \right\} \right]^{n_H} exp \left\{ \frac{-Q}{RT} \right\} \tag{2.2}$$

$$\dot{\varepsilon} = A \left[\frac{\sigma}{1 - f_{LGB}} \right]^{n_H} exp \left\{ \frac{-Q}{RT} \right\} \tag{2.3}$$

A further refinement, to utilize an internal variable, C, to represent the state of cohesion of the mush, was proposed by Ludwig et al. (2005a) as shown in equation 2.4. The variable C was introduced to account for the fact that the semi-solid body is much weaker in tension as compared to compression.

$$\dot{\varepsilon}_s^p = \frac{\dot{\varepsilon}_0}{(Cs_0)^n} \left[\frac{A_2}{3}\bar{P}_s\boldsymbol{l} + \frac{3}{2}A_3 S_s \right] \left[A_2 \bar{P}_s^{\,2} + A_3 \bar{\sigma}_s^{\,2} \right]^{\frac{n-1}{2}} \tag{2.4}$$

where, $\dot{\varepsilon}_s^p$ is the plastic strain rate tensor, $\dot{\varepsilon}$ is the reference strain rate, n and s_o describe the rheology of the fully solid state, A_2 and A_3 are solid fraction functions, $\bar{P}_s$ is the effective pressure (taken positive on compression), σ_s is the von-mises stress, $\boldsymbol{1}$ is the unit tensor and S_s is the solid phase deviatoric effective stress tensor.

More recently, Lu et al. (2008a) carried out a study on the semi-solid deformation behavior of an Al-4%Cu-Mg alloy at very low fraction liquid. They concluded that deformation in the semi-solid regime is influenced strongly by deformation induced evolution of microstructure in this regime. Based on the experimental results, they established that the flow stress (σ) is linked to process parameters and microstructural characteristics as described in equations 2.5-2.7.

$$\sigma = F_1.F_2 \tag{2.5}$$

$$F_1: \ \sigma = \varepsilon^m \dot{\varepsilon}^n (a - bt)(1 - \beta f_1)^k \tag{2.6}$$

$$F_2: f(d) = A_0 + A_1\left(\frac{d}{d_0}\right) + A_1\left(\frac{d}{d_0}\right)^2 \tag{2.7}$$

where, F_1 is a function related to the process parameters, F_2 is a function dependent on the microstructural evolution during deformation of the semi-solid mush, d_0 (μm) is the grain size at the commencement of semi-solid deformation, d (μm) is the average grain size at the temperature of deformation (calculated based on an artificial neural network model provided in reference (Lu et al. 2008b)). Finally, A_0, A_1, A_2 are functions of the Zenner-Holloman constant (Z), deformation rate and material constants.

In the context of DC casting, an alternative methodology to model the semi-solid behavior has been to extend the constitutive law used in the fully solid regime up to the temperature corresponding to the fraction solid for mechanical coalescence (Drezet and Phillion 2010, Sengupta et al. 2005a) and then to assume a low elastic modulus and high yield stress rheology above this point. Although this methodology is relatively easy to implement within the context of process models and has the advantage of minimizing false strain accumulation in the partially liquid state, its main drawback is that there is no link to the microstructural features of the solidifying semi-solid. Recently, a new constitutive equation for semi-solid AA5182 has been proposed by Phillion et al. (2009) that takes advantage of the benefits of the Ludwik equation (see section 2.4.3) within an a FE simulation, while also including microstructural features.

For this work, a 2 dimensional finite element model was developed which can predict mechanical behavior of the semi-solid mush (Phillion et al. 2008). This FE model included the following key microstructural complications: liquid filled grain boundaries, liquid trapped at the triple junctions of grains, variable grain size and porosity. This model is valid for the range $0.75 < f_S < 0.95$, since the authors believe that hot tearing phenomenon occurs at this range. To validate this model, semi-solid tensile tests were performed with samples of aluminum alloy AA5182 that were (1) hot isostatic pressing (HIP) cast and (2) in the as cast state. A novel technique in terms of strain and temperature control were used for these semi-solid tensile tests. The HIP cast alloys contain zero porosity, while there was considerable porosity in the as cast alloy. By comparing the tensile test results of these 2 types, the effects of porosity on semi-solid deformation and in turn on the occurrence of hot tearing was illustrated. The constitutive law proposed by Phillion et al. is illustrated below:

$$\sigma(f_s, f_p, \bar{d}) = K_p(f_s \sigma_s)(\varepsilon_p + \varepsilon_0)^{n(T)}(1 - \frac{f_p}{1 - f_s}) \qquad (2.8)$$

with,

$$\sigma_s = (483.5 - 0.77T)\dot{\varepsilon}_p^{(0.205+0.00006T)} \tag{2.9}$$

$$h = \bar{d}(1 - f_s)^{\frac{1}{3}} \tag{2.10}$$

$$n = -6.35e^{-4}h^2 + 0.0202h \tag{2.11}$$

$$K_p = K_p(f_p) \tag{2.12}$$

where K_p is a parameter related to the fraction porosity, f_p, σ_s is the solid flow stress (MPa) of type elastic-perfectly-plastic, and $\bar{d}$ is the average grain size, h is the thickness of the liquid channels between grains, and n is a strain hardening parameter related to the grain size of the solid skeleton. The phenomenological expression for n has been determined based on a regression analysis of semi-solid tensile deformation experiments and microstructure simulations.

2.4.3 Constitutive law: Fully Solid

In addition to the semi-solid, the mechanical properties of the fully solid are needed when simulating the DC casting process since the metal in the external shell will solidify and cool long before the center-line is solid. Also, the mechanical properties of a semi-solid at high fraction solid infiltrated with liquid are related to the mechanical properties of the fully solid phase at high temperatures close to the solidus. In this section, different models of high temperature mechanical behavior that have been used for "computer simulations of DC casting" will be discussed. In one of the earliest works Moriceau (1975) used a elastic-plastic constitutive behavior in a continuous DC casting simulation. This type of constitutive law ignores the effect of variable strain-rates. On the other hand, the pure creep based equations (e.g. Drezet et al. (1996a)) do not take into account the effects of strain hardening at low temperatures. Other researchers have utilized a plastic strain based equation for alloys AA1050, AA3104, and AA5182 (Haaften et al. 2002), a power-law creep-based equation for alloy AA3103 (Farup and Mo 2000), and a combination of the two (Mathew and Brody 1976). In a unique study, Mo and colleagues (Mo

22

and Holm 1993) developed an internal state variable approach that included a term for microstructure evolution during cooling below the solidus temperature in order to capture different constitutive behaviour in different regions of the casting as a function of cooling rate.

Now-a-days, the generally-accepted practice for simulating the fully solid constitutive behaviour of aluminum alloys is to include the effects of strain hardening and strain rate sensitivity through the use of the so-called extended Ludwik equation (Fjaer and Mo 1990, Haaften et al. 2002, Magnin et al. 1996), as shown in equation 2.13. This formulation allows a single equation to be used for predicting the constitutive behaviour throughout the 'fully solid' temperature regime of DC casting.

$$\sigma(T, \varepsilon, \dot{\varepsilon}) = K(T)(\varepsilon_p + \varepsilon_{P_0})^{n(T)}(\dot{\varepsilon_p} + \dot{\varepsilon_{P_0}})^{m(T)} \tag{2.13}$$

where σ is the stress (MPa), K is a material constant related to the strength of the material, n is the strain hardening exponent, m is the strain-rate sensitivity exponent, ε_p is the plastic strain, and $\dot{\varepsilon}_p$ is the plastic strain rate (s^{-1}). The values of K, m and n are generally determined by curve fitting method from the experimental results and are unique to each alloy. The two offset constants ε_{p_0} and $\dot{\varepsilon}_{p_0}$ are incorporated into the equation to circumvent convergence issues.

2.5   Processing Effects on Hot tearing

2.5.1   Casting Speed

Of the parameters responsible for solidification defects in DC casting billets/ingots, casting speed is considered most important (M'Hamdi et al. 2002, Nagaumi et al. 2000). The other parameters, e.g. pouring temperature of the molten metal and water flow rate from the water-jet are industrially considered to be less important (Nagaumi et al. 2000). Zheng et al. (2011) showed that increasing casting speed increases the size of columnar grains

at the center of the billet and also increases the amount of macrosegregation in a Mg-Nd-Zn-Zr alloy. So, it is expected that an increase in casting speed would have similar detrimental effects on the condition for hot-tearing in DC cast products. This is actually seen generally in the casting industry and has been demonstrated through both simulation (Drezet and Rappaz 2001, Hao et al. 2010, M'Hamdi et al. 2002, Suyitno et al. 2005) and through experimental observations (Hao et al. 2010). Based on the RDG criterion presented in section 2.7, Drezet and Rappaz (2001) calculated the depression pressure within DC casting billets and found that higher casting speeds result in larger pressure drops and consequently a higher hot tearing tendency. According to the RDG criterion, this drop in pressure increases the hot tearing susceptibility. (Hao et al. 2010) also used the RDG criterion with a DC casting simulation of alloy AZ31 to reach the same conclusion. Suyitno et al. (2005) implimented several hot tearing criteria (see section 2.7) to a DC casting simulation, and found that all the criteria indicated exacerbation of hot tearing scenario at higher casting speeds.

2.5.2 Pouring Temperature and Water Flow Rate

Pouring temperature and water flow rate have some effect on hot tearing tendency in DC casting. Increasing pouring temperature increases hot tearing tendency and vice versa (Li 2010). The reason behind this could be two fold. First, the higher pouring temperature decreases the cooling rate, and thus results in larger grain sizes (Li 2010). This in turn, reduces the structure's ability to withstand thermal stresses generated during DC casting, and increases the hot tearing tendency. The second reason could be the thickening of liquid films due to large grain size. Thicker liquid films between grains tend to increase the hot tearing tendency (Suyitno et al. 2002) Although, increasing water flow rate increases the cooling at the surface of the billet, this has the disadvantage of increasing the differential thermal contraction, i.e. the surface cools and thus contracts faster than the center. This increases the possibility of hot tearing in DC casting of aluminum alloys, particularly at the solidification front. (Sengupta et al. 2005b).
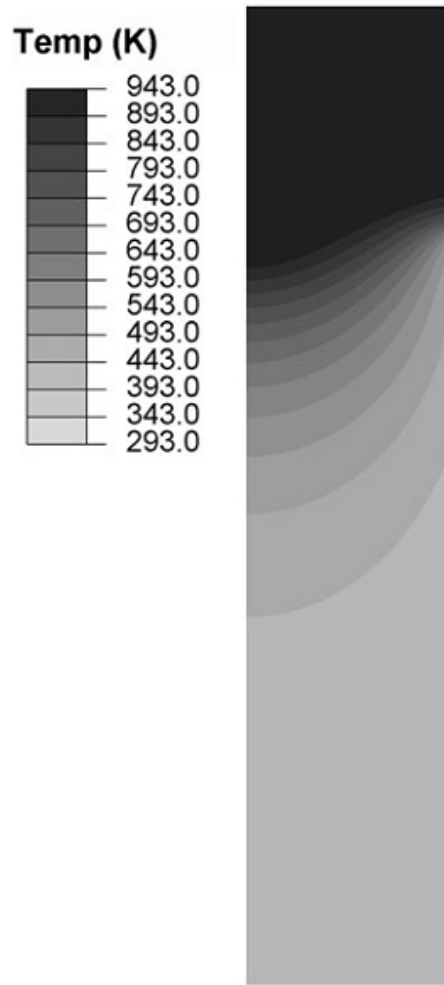
Figure 2.5: Temperature contour of a DC cast billet 1000 sec after start-up predicted by an axi-symmetric DC casting process model (Drezet and Phillion 2010)

2.6 Effect of Cooling Rate on Microstructural Features

Because hot tearing occurs in the semi-solid regime, the mechanical properties at this region are critical. As we have seen in section 2.4.2, the microstructural features play an important role in the mechanical properties of the semi-solid aluminum alloys (Lu et al. 2008a, Phillion et al. 2009). During the DC casting process, there exists a variety in temperature at different locations of the billet. A typical temperature profile is shown in figure 2.5 which was predicted by a DC casting process model for AA6061 billets, $1000sec$

after start of the casting (Drezet and Phillion 2010). From figure 2.5, it it obvious that the side walls and the base of the casting cools very fast while the center of the casting remains at high temperatures. As a result, the different parts of the billet cools at different rates. The cooling rate is known to strongly influence the microstructural features and solidification path in aluminum alloys. In the following subsections, the effect of cooling rate on various microstructural features and volume fraction solid in DC casting process are discussed.

2.6.1 Grain Size

Grain size is an important microstructural feature, especially when hot tearing is considered since the columnar grains are highly susceptible to hot tearing whereas equiaxed grains are known to reduce hot tearing tendency. Moreover, hot tearing is less likely to occur in highly grain refined cast aluminum alloys (Campbell 1991, Easton et al. 2004, Grandfield et al. 2005, Granger 1998). Other researchers such as Lin et al. (2007), Campbell (1991) also observed this phenomenon to some extent in wrought aluminum alloys. Grain refinement is thought to improve hot tearing by reorganizing the eutectic distribution and reducing the scale of the liquid channels. As grain refinement increases the grain boundary area, it will also increase the amount of eutectic at the grain boundaries. It is well established (Lin et al. 2007) that the presence of low melting eutectic material at the grain boundaries helps to compensate for the solidification shrinkage and thus failure to compensate for this shrinkage may result in hot tearing. However, in some alloys, such as AA5182, the act of grain refinement alone cannot prevent hot tearing since there is simply not enough eutectic material to reduce hot tearing susceptibility. In these cases, variation in processing parameters is also needed (Grandfield et al. 2005, M'Hamdi et al. 2002).

As is well known, there is an inverse relationship between cooling rate and grain size. Larger cooling rates lead to increased grain nucleation and smaller grains. For example, Dobrzanski et al. (2007) recently showed that an increase in the solidification rate

decreased the grain size, secondary dendrite arm spacing (SDAS), and also the secondary precipitates. Since, as shown in figure 2.5 there is a variation in cooling conditions within the billet, we can expect grains of assorted sizes to form the length of the casting. One method that can be utilized to relate grain size and cooling rate is based on the growth restriction factor as developed by Easton and StJohn (2001). This factor, Q, is a function of the alloying elements and grain refiners that are added to the alloy and can be used to predict grain size as shown in equation 4.13, where the average grain size, $\bar{d}$ is expressed as an inverse relationship with Q and a and b are constants related to cooling rate, $\dot{T}$. The equations for a and b are given in equations 4.14 and 4.15.

$$\bar{d} = a + \frac{b}{Q} \tag{2.14}$$

$$b = 281 + \frac{381}{\dot{T}^{\frac{1}{2}}} \tag{2.15}$$

$$a = -22.08\dot{T} + 222.88 \tag{2.16}$$

From equations 4.13- 4.15, it can be concluded that increasing the cooling rate decreases the grain size in two ways. First, by increasing the number of nucleation cites, and second, by introducing constitutional undercooling. To the author's knowledge, the DC casting process models available in the literature have not considered the provision for variable grain size as a function of the differential cooling conditions across the DC cast billet or ingot. The variation in cooling conditions is the key here, because now-a-days high amount of grain refiners are used during the industrial DC casting process. Consequently, the effect of grain refinement should be similar in all parts of the casting, and thus any grain size variation is only due to cooling conditions.

2.6.2 Volume Fraction Solid (f_s)

DC casting models also require the relevant solidification path of the alloy being simulated. Is it important to accurately describe the start and termination of solidification process and how the fraction solid evolves in the semi-solid regime as a function of temperature, because these parameters are linked strongly with semi-solid mechanical properties (Braccini et al. 2000, Lu et al. 2008a, Phillion et al. 2009). Thus, for good semi-solid stress-strain predictions, an accurate description solidification path of the alloy need to included in the model.

The solidification path or the evolution of fraction solid of the aluminum alloys during casting have been estimated by different researchers over the years. In the series of books (Bäckerud and Tamminen 1986, Bäckerud et al. 1990), the solidification characteristics of all the common foundry (Bäckerud et al. 1990) and wrought (Bäckerud and Tamminen 1986) aluminum alloys have been compiled. In this magnum-opus, the solidification paths were determined based on thermal analysis of the alloys in a differential thermal analyzer (DTA). The effect of cooling rate on the temperature of commencement of the solidification reactions as well as grain size, liquidus and solidus temperatures have been presented in these books. The results show that these parameters vary strongly as a function of the cooling rate. Jeng and Chen (1996) obtained cooling curves of aluminum alloy A356.2 using a differential thermal analyzer (DTA). A mathematical model was then used to postprocess these DTA cooling curves to obtain the solidification path of the alloy. Solidification path of a complex Al-Mn-Be alloy was determined by Markoli et al. (2010). They conducted a series of experiments using differential scanning calorimeter (DSC), and thermogravimetric analysis (TGA) at temperatures between 500 and 1100^oC. The samples were simultaneously imaged using scanning electron microscopy (SEM). They estimated the solidification path of the alloy at a fixed cooling rate conjoining the results from DSC, TGA and SEM. Solidification path of 3 ternary mono-eutectic aluminum alloys were studied by Mirkovic et al. (2008) on the basis of thermodynamical description of the

solidification and precipitation reactions. Similar work was done by Chang et al. (2004) who experimentally examined the solidification path of multi-component aluminum alloys and found that the experimental results are in good agreement with the fraction solids predicted by the Scheil's model coupled with phase-diagrams. Thompson et al. (2004), in their work on on alloys A356 and AA5182, determined the temperature of all the transformation reactions occurring during solidification, as well as the solidification path. Probably the most important contribution of this article is to demonstrate the variation of all transformation temperatures due to variation in cooling rate.

The authors referenced above have estimated the solidification path of aluminum alloys as a function of temperature alone. Most of them have ignored the effect of cooling rate on evolution of fraction solid (f_s). But from the work of Thompson et al. (2004) and Bäckerud and Tamminen (1986), Bäckerud et al. (1990) and some other researchers, it is evident that the solidification path of an alloy is highly sensitive to the cooling conditions.

2.7   Hot Tearing Criteria

Over the last 60 years, a considerable amount of research has been undertaken to relate hot tearing with casting parameters in order to find a hot tearing criterion. These hot tearing criteria can be divided into two broad classes: mechanical criteria (i.e. ones based on a failure of the material) and non-mechanical criteria (i.e. ones based on casting and/or solidification parameters). An additional class of hot tearing criteria, which combines both the mechanical and non-mechanical criteria has also been discussed. The mechanical criteria can be further subdivided into stain based, strain rate based and critical stress based criteria. Non mechanical criteria are based on brittle temperature range, processing conditions and phase diagrams. The various hot tearing criteria relevant to DC casting are discussed below.

2.7.1 Mechanical Criteria

Pellini in 1952 (Pellini 1952), was the first to propose a hot tearing criterion, by postu-lating that that if the total strain accumulated is greater than some critical strain, hot tears would form. The more recent criterion by Yamanaka et al. (1992), also relies on the same principle, but limits the strain accumulation specifically to the brittle temperature region (BTR). Won et al. (2000) further modified Pellini's criterion by including strain rate term to the BTR, in addition to the total strain accumulation.

Prokhorov (1962) proposed a criterion that included the parameters of shrinkage and 'apparent' strain rate in the semi-solid structure as a predictor for hot tearing. These parameters were compared with the fracture strain of the coherent semi-solid body to assess hot tearing susceptibility. The proposed relationship of strain rates by Prokhorov et al. is shown in equations 2.17, where $\dot{\varepsilon}_{min}$, $\dot{\varepsilon}_{free}$ and $\dot{\varepsilon}_{app}$ are strain rates for minimum fracture strain, linear free shrinkage and apparent strain, respectively. Moreover, $\dot{\varepsilon}_{min}$ is the strain rate for reserve of hot tearing strain in the brittle temperature region (BTR). A hot tear is thus likely to occur when $\dot{\varepsilon}_{min} \leq 0$ or when equation 2.17 is satisfied.

$$\Delta\dot{\varepsilon}_{res} \leq \dot{\varepsilon}_{min} - \dot{\varepsilon}_{free} - \dot{\varepsilon}_{app} \tag{2.17}$$

$$HCS = \frac{t_{0.99} - t_{cr}}{t_{cr} - t_{coh}} \tag{2.18}$$

Another strain based criterion was proposed by Magnin et al. (Magnin et al. 1996), through a calculation of the hot tearing susceptibility as the ratio of plastic hoop strain ($\varepsilon_{\theta\theta}^{pl}$) measured at solidus to the measured fracture strain at high fraction solid (ε_{fr}). Therefore,

$$HCS = \frac{\varepsilon_{\theta\theta}}{\varepsilon_{fr}} \tag{2.19}$$

where HCS is the susceptibility to hot tear formation and thus hot tearing is likely to form when $HCS \geq 1$. Braccini et al. proposed a critical strain rate ($\dot{\varepsilon}^C$), shown in

equation 2.20 which can also be used as an indication of hot tearing susceptibility.

$$\dot{\varepsilon}^C = \left[1 - \frac{e}{l}\right]\left[\frac{\lambda - a}{\lambda}\left\{\frac{\frac{2}{3}P_C - P_M}{K(T, f_s)}\right\}\right]^{1/m} + \frac{e}{l}\frac{2\kappa}{(\lambda - a)^2}\frac{P_C}{\eta_L} \qquad (2.20)$$

where l is gauge length, e liquid film thickness, λ is half of grain size, a is the length of the crack, P_C is cavitation pressure, P_M is the metallostatic pressure, K is a material parameter and a function of T and f_s, m is strain rate sensitivity, κ is the permeability of the mush and η_L is the liquid viscosity.

2.7.2 Non Mechanical Criteria

Feurer (1976) attributed hot tearing as influenced by alloy composition and solidification conditions. Two terms were defined: liquid volumetric flow rate per unit volume (SPV) and solidification front (SRG). When $SRG < SPV$, hot tearing occurs, with (SRG-SPV) being deemed the driving force for hot tear formation. Clyne and Davies (1981) proposed their hot tearing criterion based on the 4 stage response of the solidifying casting to stress. According to their studies, hot tearing sensitivity is related to the ratio of time spent in the vulnerable region (t_v) to the time period during stress relief (t_R), as shown in equation 2.21. Here, t_s corresponds to the time when volume fraction solid is f_s.

$$HCS = \frac{t_v}{t_R} = \frac{t_{0.99} - t_{0.9}}{t_{0.9} - t_{0.4}} \qquad (2.21)$$

An improvement to original criteria by Clyne and Davis was proposed by Campbell (Campbell 1991) by introducing the solidification interval (ΔT), the coefficient of thermal expansion (α_{CTE}) and casting dimensions into the index. The proposed equation is shown below:

$$CSC_b = \frac{\alpha_{CTE}\Delta T dt_v}{l^2 t_r} \qquad (2.22)$$

where L is the overall length of the casting, d is the grain size, l is the length of the hot spot measured in the direction of the strain for a 1-dimensional case.

2.7.3 Combined (Mechanical and Non Mechanical) Criteria

Hot teaming criteria based on both mechanical and non mechanical influences include Rappaz-Drezet-Gremaud (RDG) criterion (Rappaz et al. 1999). According to RDG criterion, if the pressure in the mushy zone becomes larger than a critical pressure, hot tears form. According to the criterion, the depression pressure in the mushy zone is calculated using equation 2.23, where Δp_{sh} and Δp_{mec} are the drop in pressure of the mush related to the solidification shrinkage and the fluid flow due to deformation, respectively. ρ is the density, h is the distance below molten metal level, and g is the gravitational constant. When $\Delta p \geq \Delta p_c$, hot tears will form. It seems that critical pressure Δp_c is alloy dependent and is assumed to be 2 KPa (Rappaz et al. 1999).

$$\Delta p = \Delta p_{sh} + \Delta p_{mec} - \rho g h \tag{2.23}$$

To calculate the pressure drop contributions, a mass balance was performed on a small volume of the mush by relating the pressure drop and the velocity of the liquid required to maintain this pressure drop using Darcy's law. This mass balance is shown in equation 2.24.

$$f_l v_l = \frac{-K}{\mu} \frac{dP}{dx} \tag{2.24}$$

where v_l is liquid velocity, μ is the liquid viscosity and K is the permeability of the mushy zone. The classical Carman - Kozeny relation was used by the authors for formulation of K, as shown in equation 2.25.

$$K = \frac{\lambda_2^2}{180} \frac{(1 - f_s)^3}{f_s^2} \tag{2.25}$$

where λ_2 is the secondary dendrite arm spacing. Two assumptions were made at this point for mass balance calculations, (1) liquid flows only in the direction of heat flow, and (2) deformation of solid occurs perpendicular to the heat flow. The resulting mass

balance is shown in equation 2.26.

$$\frac{\partial}{\partial t}(\rho_l f_l + \rho_s f_s) + \frac{\partial}{\partial x}(\rho_l f_l v_{l,x}) + \frac{\partial}{\partial y}(\rho_s f_s v_{s,y}) = 0 \tag{2.26}$$

where, $v_{l,x}$ and $v_{s,y}$ are liquid and solid velocities in their respective directions. The RDG criterion was able to relate transverse strain rate with solid deformation by the relation $\dot{\varepsilon}_p = \frac{\partial v_{s,y}}{\partial y}$. Finally, the hot cracking sensitivity (HCS) was proposed as per equation 2.27.

$$HCS = \frac{1}{\dot{\varepsilon}^{max}} \tag{2.27}$$

where $\dot{\varepsilon}^{max}$ is the maximum allowable strain rate before hot tears form at a given critical pressure. The challenge of incorporating the RDG criterion in a DC casting process model is the value of $P_{critical}$, which seemed to have been arbitrarily chosen as 2 MPa for aluminum alloys. Furthermore, the role of total strain has been ignored in this criterion (as opposed to total strain criterion by Pellini). Lastly, the void formation has been assumed to be the staring point of hot tearing. Since it is well known that voids may also give rise to microporosity, this criterion fails to distinguish between porosity formation and the formation of hot tears.

Braccini et al. (2000) modified the RDG criterion to calculate the pressure drop in the mushy zone by proposing that the permeability term should be calculated according to the percolation theory, instead of the traditional Karmen-Cozeny relationship, as shown in equation 2.28.

$$K = \frac{1}{32}(1 - f_s)^3(f_s^c - f_s)^\mu {\lambda_1}^2 \tag{2.28}$$

where f_s^c is the coalescence fraction solid, λ_1 is the the primary dendrite arm spacing, and μ is the viscosity. A solution to the the arbitrary assumptions of the critical pressure was proposed as well. In this case, P_c was calculated based on the liquid-vapour interfacial energy (σ_{lv}) and the wetting-angle (θ), as shown in equation 2.29.

$$P_c = \frac{4cos\theta\sigma_{lv}}{(1 - f_s)\lambda_1} \tag{2.29}$$

To resolve the ambiguity of whether voids will develop into microporosity or into hot tears, Suyitno et al. (2002) modified the RDG criterion. Similar to the RDG approach, a mass balance was done with a small volume element in the mushy zone, but instead of the Darcy's law, liquid feeding term from Feurer's criterion (Feurer 1976) was used. The Griffith crack propagation theory was then applied to estimate the relationship between the minimum stress for crack propagation and diameter of void, as shown in equation 2.30.

$$d_{crit} = 4\gamma_e \frac{E}{\pi\sigma_m^2} \tag{2.30}$$

where d_{crit} is the crack length, γ_e is the surface tension of the liquid metal, E is the modulus and σ_m is the minimum stress. If σ_m is larger than the casting stress state, any pore of diameter larger than d_{crit} would become a hot tear.

In this context, less amount of work has been done to propose a hot tearing criterion based on microstructural features such as grain size, coalescence temperature, etc. The criterion proposed by Campbell (1991) included the grain size (d). From this criterion (equation 2.22), it is seen that the hot tearing susceptibility increases with increasing grain size and vice versa, provided that the other parameters of the criterion remain unchanged. Similarly, work by Lin et al. (2007) suggests that hot tearing susceptibility increases with decreasing grain size. A hot tearing susceptibility (HTS) index as a polynomial function of grain size (d) is proposed, as shown in equation 2.31. In this equation, d is in μm. By plotting HTS against d, it can be shown that below $d \approx 200\mu$m, HTS is relatively independent of d. The authors also noted that it is important to take coalescence temperature into account when comparing HTS for different alloys.

$$HTS = 6 \times 10^{-5}d^2 - 0.014d + 3 \tag{2.31}$$

2.7.4 Application of Hot Tearing Criteria into DC casting Process Models

Drezet and Rappaz (2001) calculated the depression pressure within a DC casting process model and found that higher casting speeds result in larger pressure drops and consequently a higher hot tearing tendency according to the RDG criterion (Rappaz et al. 1999). The authors also calculated the cracking sensitivity index based on (Clyne and Davies 1981), and found the opposite trend, i.e. lower casting speeds produce higher sensitivity to hot tearing. Thus, that the application of the criterion by Clyne is not appropriate for DC casting process models. Suyitno et al. (2005) applied 8 hot tearing criteria(Feurer (1976), Clyne and Davies (1981), Katgerman et al., Prokhorov (1962), Novikov, Pellini (1952) and Rappaz et al. (1999)) criterion into a DC casting process model for Al-4.5%Cu alloy and investigated the effects of casting speed on hot tearing phenomenon. Of the 8 criteria, only the RDG criterion was in a position to explicitly decide if the crack is going to form or not, the other 7 were just able to access relative susceptibility of hot tearing at different locations of the billet and for different casting speeds. Additionally, predictions from the RDG criterion were most successful in matching with the common industrial practice.

2.8 Summary

In this chapter, the DC casting process models developed so far have been discussed and their advantaged and limitations have been critically reviewed. The main challenge for the development of DC casting process models is how to describe the mechanical properties of the semi-solid mush. The semi-solid material models proposed by different researchers have been presented in this chapter. The models that include microstructural features of the mush seems to be the most comprehensive ones. To enable hot tearing study, the model must valid for the range of solid fractions(f_s) where it is most likely to occur. Other challenges include the problem of strain accumulation within the liquid which will overestimate the predicted strains within the cast body at high fraction solid.

Chapter 3

Scope and Objective

For the past 60 years, hot tearing has been an active field of study amongst the researchers concerned with metal casting. Both experimental and theoretical research have led to significant advances in the understanding of this complex phenomenon. However, quantitative prediction of the occurrence and extent of this defect remains very difficult, due to the great complexity of the problem. Several physical phenomena such as heat flow, liquid flow and deformation are occurring simultaneously. In addition, hot tearing is typically a multi-scale problem in which solid grains of typically 100μm are grouped in mushy zones that are a few cm thick and experience constraints imposed by an industrial process at the meter scale. Moreover, mushy alloys have properties that are neither easy to measure, nor straightforward to model. With these issues in mind, the main objective of this research project is to investigate occurrence of hot tearing in direct chill cast Aluminum alloy AA5182 with respect to microstructural features and process parameters. In order to successfully achieve this goal, the following subgoals have been identified:

1. Develop a DC casting process model that incorporates a robust constitutive law for semi-solid behaviour. In this project, a thermo-mechanical process model has been developed based on the previous work by J-M. Drezet (Drezet et al. 2000a) and Joydeep Sengupta (Sengupta et al. 2005a) and incorporationg new semi-solid constitutive model proposed by Phillion et al. (2009). This constitutive law is

particularly useful to study hot tearing with respect to microstructural features because it takes into account the grain size of the semi-solid mush.

2. To analyze the relative susceptibility to hot tearing of castings with various microstructural features and cast under various processing conditions. In order to achieve this, a quantitative index for hot tearing susceptibility has been proposed that takes into account the semi-solid stress strain predictions from the process model.

3. To characterize various aspects of the structural features and solidification behaviour of AA5182 in the as cast state. This work has been accomplished via optical microscopy, scanning electron microscopy, and differential scanning calorimetry.

The organization of this thesis follows these goals. In chapter 4, the development of the finite element process model is discussed. In this chapter, the casting geometry, boundary conditions, and material properties for the model have been described in detail. In chapter 5, the development of the quantitative index has been presented. The relative hot tearing susceptibility DC cast products with respect to the structure and processing conditions is presented and discussed in this chapter using this quantitative index. In chapter 6, the experimental methodology for observing microstructural features and solidification behavior of as cast AA5182 has been presented. In the following chapter, the results from the experiments run on a DC cast AA5182 ingot has been presented and compared with the theory and available literature. In chapter 8, new findings from this research project, along with its limitations and possible future research on this topic have been registered.

Chapter 4

Development of Direct Chill Casting Process Model

4.1　Introduction

To study the formation of hot tearing defects in Direct Chill casting of aluminum alloys, the evolution in the thermal as well the displacement fields must be known. The displacement field provides information relating to the strain and stress tensor at the startup and steady state regimes of the casting. The corresponding thermal field is required to determine the solidification sequence. The alloy chosen for this study is an aluminum alloy AA5182 (Composition : Mn 0.35%-Mg 4.5%-Al balance). This alloy is primarily used for the production of beverage can lids, and is prone to hot tearing.

　　The development of a direct chill casting process model requires the following :

- Finite element analysis formulation

- Thermophysical properties of the material

- Constitutive properties

- Initial and boundary conditions

A general purpose finite element software **ABAQUS version 6.10** has been chosen for the current research project. ABAQUS is a well known commercial platform that is highly capable of solving transient and highly non-linear mechanical and heat transfer problems. The process model that was used in this work is based on a earlier model developed by Dr. J.-M. Drezet (Drezet and Phillion 2010, Drezet and Rappaz 2001, Drezet et al. 2000a). In this earlier work, both the thermal fields and residual stress fields were validated against thermocouple data from industrial DC casting trials and strain measurements obtained via neutron diffraction.

4.2 Finite Element Analysis Formulation

Finite element modeling of the DC casting process involves the solution of both the partial differential equations for heat transfer and force-displacement in matrix form. The governing equation for the heat transfer analysis of the model is shown in equation 4.1.

$$\bigtriangledown \left[k(T) \bigtriangledown T \right] + \dot{Q} = \rho C_p \frac{\partial T}{\partial t} \tag{4.1}$$

where ρ is the density in kgm^{-3}, C_p is the specific heat in $\text{Jkg}^{-1}\text{K}^{-1}$, k is the thermal conductivity in $\text{Wm}^{-1}\text{K}^{-1}$, $\dot{Q}$ is the latent heat of solidification in Wm^{-3}, and T is the temperature in K. For the mechanical simulation, ABAQUS solves for the force and momentum equilibrium on the whole domain by linking force fields and nodal displacements using the stiffness matrix. The strain tensor is then calculated from these nodal displacements. The stress-strain state at each elemental integration point can then be calculated using the strain-displacement relation. The elements of the elastic stiffness matrix, $[D^{el}]$ are related to the elastic modulus and Poisson's ratio. Within the elastic limit, total stress and total strain maintain a linear relationship (i.e. Hook's law) as shown in equation 4.2.

$$(\sigma) = [D^{el}](\varepsilon^{el}) \tag{4.2}$$

where (σ) and (ε^{el}) are the stress and elastic strain tensors, respectively. In the plastic regime of material behavior, the plastic stiffness matrix, $[D^{ep}]$ is used to relate between current increment of stress tensor $(d\sigma)$ and current increment of the plastic strain tensor $(d\varepsilon^{ep})$ as per equation 4.3. The constitutive law used to describe the stress-strain relationship of the material is described in a later section.

$$(d\sigma) = [D^{ep}](\varepsilon^{ep}) \tag{4.3}$$

For studying hot tearing in a DC casting process model, a fully coupled thermal-mechanical analysis is required. The coupled thermal-displacement analysis solves the thermal and mechanical equations simultaneously, rather than sequentially. Potential sources of coupling include the formation of an air gap between both the solidifying metal and the mold and the solidifying metal and the bottom block. In a fully coupled thermal mechanical analysis, the thermal and mechanical equations are simultaneously solved as per equation 4.4.

$$\begin{bmatrix} K_{uu} & K_{u\theta} \\ K_{\theta u} & K_{\theta\theta} \end{bmatrix} \begin{Bmatrix} \Delta u \\ \Delta\theta \end{Bmatrix} = \begin{Bmatrix} R_u \\ R_\theta \end{Bmatrix} \tag{4.4}$$

where, $[K_{ij}]$ are the submatrices of the fully coupled Jacobian matrix, Δu and $\Delta\theta$ are corrections for displacement and temperature, respectively, and R_u and R_θ are residual vectors for thermal and mechanical analysis, respectively. In ABAQUS, a backward difference method is utilized for the transient solution and Newton's method is implemented to solve the fully coupled system.

4.2.1 Geometry

A round billet has been chosen for analysis, of dimensions 800 mm in height and 320 mm in diameter. The computational domain is reduced to an axi-symmetric geometry as a result of symmetry and thus the dimensions of the simulation are 160 mm and 800 mm in the radial and axial directions, respectively, as shown in figure 4.2.
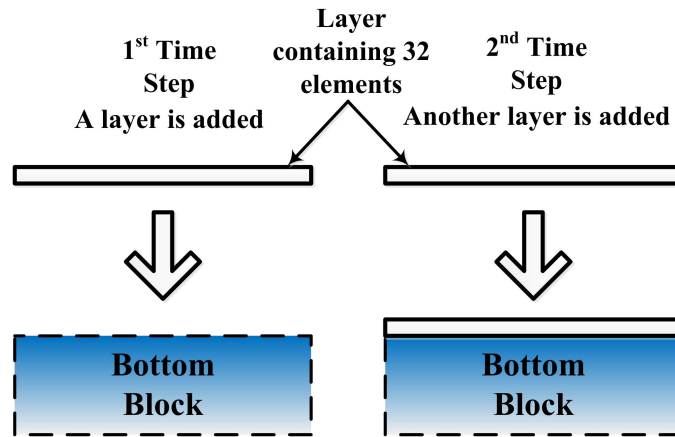
Figure 4.1: Schematic presentation of the incremental addition of layers adopted in the model

4.2.2 Mesh

The domain is made up of 200 layers, each of 4 mm height. Each layer consists of 32 elements, with dimensions 4 mm in height and 5 mm in width. The elements are of type CAX4T, which are four-node bilinear temperature and displacement elements. As a result, the FE mesh of the domain consists of a total of 6400 elements and 6633 nodes.

4.2.3 Addition of Layers

A Lagrangian approach is adopted to simulate the DC casting process. In addition, the thermal boundary conditions are gradually moved upwards at a rate compatible with the billet withdrawal speed. To simulate the mold filling and gradual increase of billet height, horizontal layers each containing 32 elements were added incrementally into the domain as shown in figure 4.1. In the 1st time step, one horizontal layer is added, then another layer is added in the 2nd time step, and so on. This approach is used in order to simulate the overall heat input into the system as a function of time. The casting simulation is finished when all 200 layers have been added in 200 time steps. The time steps are calculated based on the height of each element layer and the casting speed.

4.3 Thermal Initial Conditions

In a transient heat transfer problem such as the DC casting process, an initial thermal condition must be known to solve the heat equation. The initial temperature of the domain was set to 650°C, which is the typical pouring temperature of AA5182 during DC casting. The ambient temperature was assumed to be 25°C.

4.4 Boundary Conditions

Both mechanical and thermal boundary conditions are imposed onto the calculation domain.

4.4.1 Thermal Boundary Conditions

The thermal boundary conditions for the model were set to reflect different modes of cooling taking place in different regimes of the billet. Each surface of the axi-symmetric domain was subject to thermal boundary condition(s), as shown schematically in figure 4.2. These boundary conditions are reviewed below:

- Centerline (Γ_1)

- Top Surface (Γ_2)

- Open Side (Primary Cooling) (Γ_3)

- Open Side (Secondary Cooling) (Γ_4)

- Bottom Block Interface (Γ_5)

Both the centerline (Γ_1) and top surface (Γ_2) were assumed to be adiabatic because of symmetry. The billet surfaces (Γ_3 and Γ_4) were subjected to Cauchy type boundary conditions during primary (mold) cooling and secondary (water) cooling. The bottom surface of the billet, in contact with the bottom block, was also subjected to a Cauchy type boundary condition.
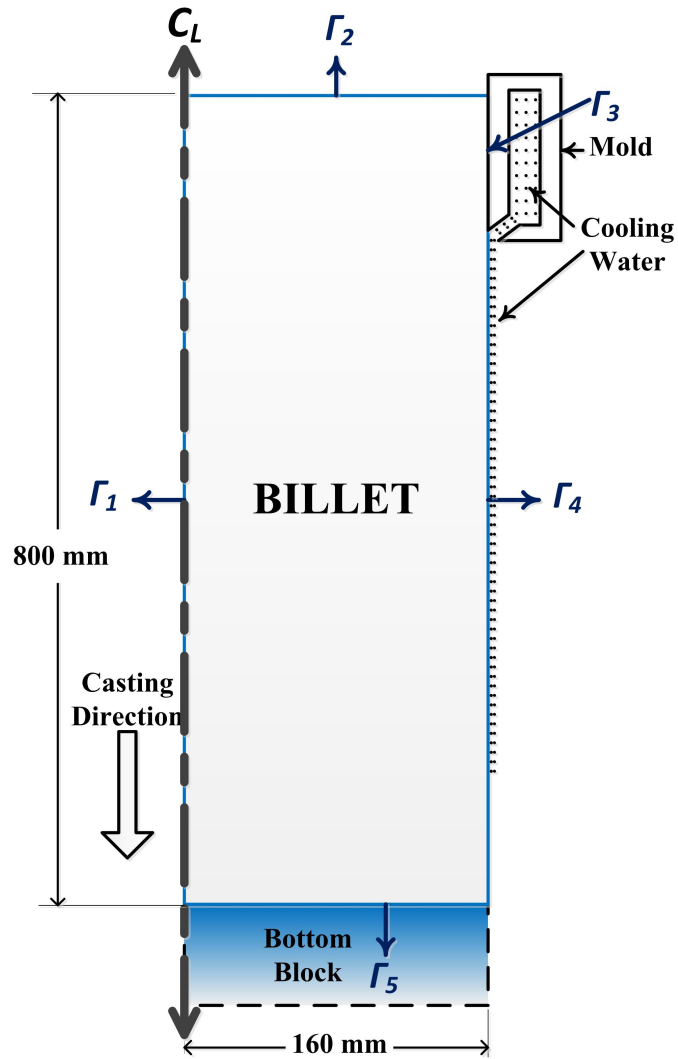
Figure 4.2: Thermal boundary conditions applied in the process model.

Cauchy Type Boundary Condition (at Γ_3, Γ_4 and Γ_5)

A Cauchy type boundary condition is used in order to make the resulting heat flux a function of both the surface and surrounding temperatures. As the surface temperature (T) approaches the surrounding value (T_∞), the heat flux (q) reduces to zero as shown below in equation 4.5, where h is the heat transfer coefficient.

$$q = h(T - T_\infty) \tag{4.5}$$

During DC casting, heat transfer on the open side of the billet is complicated due to the fact that the billet first passes through the mold, then an air gap, and then cooled by

water sprays. The high temperatures of the billet surface result in the need to use complex heat transfer coefficients during secondary cooling, i.e. boiling water heat transfer relationships. The resulting heat transfer coefficients are non-linear in nature.

At Γ_3

As the liquid metal comes in contact with the mold, it starts to solidify and shrink away from the mold. So, as the temperature of the casting surface decreases, contact between the mould and the billet also decreases, an air gap between the surface of the casting and mold is created and increased. To account for this change in contact pressure, the heat transfer coefficient is varied as a function of volume fraction solid of the solidifying metal, since $f_s \propto T$. At first, when there is a good contact between mold and metal, h is high, i.e, $h_{contact}$=2000 W/m²K (Fjaer et al. 1999). At the point when solid shell exits the mold, there is a considerable air gap between mold and casting surface. Thus, a low h is assumed for the air gap cooling ($h_{gap} = 50$W/m²K) (Fjaer et al. 1999). Since the air gap is not known "a priori", it is assumed that the air gap is a function of volume fraction solid as shown in equation 4.6.

$$h_{\Gamma_3} = h_{contact}(1 - f_s) + h_{gap} * f_s \tag{4.6}$$

At (Γ_4)

The secondary cooling on the billet surface by the cooling water jet can be further divided into 2 zones. First, the impingement zone where the water jet first comes into contact with the surface and second, the free falling zone where the sprayed water runs down the surface. In these two zones, the main mode of heat transfer is the boiling water heat transfer. Empirical boiling water curves were used in this model to determine the heat transfer coefficient (HTC) at the surface (Drezet and Rappaz 2001, Drezet et al. 2000a). The model calculates HTC at the surface depending on the temperature of the surface, the water flow rate and the 'current' vertical distance below the impingement point. The model only considers nucleate boiling regime of the boiling curve. At higher temperatures

of the surface, a lower rate of heat transfer happens due to a phenomenon called the film boiling. However, this is not included in the model, for simplicity.

At (Γ_5)

Cooling between the billet and bottom block is simulated using a constant heat transfer coefficient of 1000 $\text{Wm}^{-2}\text{K}^{-1}$. Although more complex conditions can arise, this constant value is sufficient to investigate hot tearing formation.

4.4.2 Boundary Conditions - Mechanical

A mechanical boundary condition is required to prevent separation of the bottom block and the billet at the centerline, as well as horizontal motion of the centerline itself. These boundary conditions prevent rigid body motion in order to avoid convergence issues during the simulation. The application of this boundary condition is simply to pin the bottom node at the centerline along the r and z directions.

4.5 Material Properties

The alloy chosen for the simulation in this work is the aluminum alloy AA5182. AA5182 is a non heat treatable aluminum wrought alloy with nominal compositions of Mn 0.35%-Mg 4.5%-Al balance. During solidification, AA5182 spends more time in the brittle temperature region than many other aluminum alloys because it has a large solidification window ($T_{sol} = 523^oC$ and $T_{liq} = 637^oC$). Thus it is well-known to be prone to hot tearing.

4.5.1 Thermophysical Properties

The thermophysical properties that must be included in a thermal-mechanical finite element simulation are density, latent heat, heat capacity and thermal conductivity. The temperature dependent thermophysical properties are listed in table 4.1 and are taken from Mondolfo (1976). For ease of analysis, the latent heat was varied linearly between solidus and liquidus temperatures. In addition, the density of the domain is kept con-

Table 4.1: Summary of thermophysical properties used in the process-model

Property	Temperature Range	Equation
Conductivity $(Wm^{-1}K^{-1})$	$T<T_{coal}$	$119.2 + 0.623T$
	$T_{coal} \leq T \leq T_{liq}$	$594 - 0.484T - 0.00048T^2$
	$T>T_{liq}$	$69 + 0.033T$
Specific Heat $(Jkg^{-1}K^{-1})$	$T<T_{coal}$	$897 + 0.452T$
	$T_{coal} \leq T \leq T_{liq}$	$-994.8 + 8T - 0.0074T^2$
	$T>T_{liq}$	1097
Density(kgm^{-3})	N/A	2400
Latent Heat		$\dot{Q}_{LH} = 397.1 kJkg^{-1}$
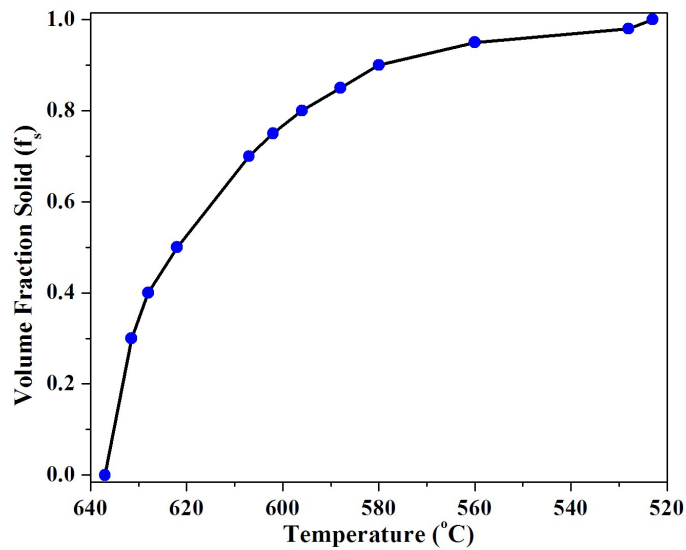
Figure 4.3: Solidification path of AA5182 used in the model (after Thompson et al. (2004))

.

stant to conserve the volume since the inclusion of a temperature-dependent density would change the heat balance of the system. The solidification path for this alloy is taken from the work of Thompson et al. (2004) as shown in figure 4.3. The change of solidification sequence with cooling rate is not accounted for in this study. Finally, as fluid flow is ignored in this simulation, the thermal conductivity of the semi-solid metal is artificially increased to account for the convection of heat in the liquid. In the liquid state, the thermal conductivity value was increased to four times its actual value to take into account this convective transport.

4.5.2 Mechanical Properties

The model requires a number of mechanical properties including Poisson's ratio, coefficient of thermal expansion (α), Young's modulus (E) for deformation in the elastic region, and a constitutive law for deformation in the plastic regime. The Poisson's ratio is assumed to be a constant value of 0.3. The Young's modulus is temperature-dependent Mondolfo (1976), and is given in figure 4.4. As can be seen, the value of E varies from 71 GPa at room temperature to 10 GPa at T_{sol}, and is then reduced to 0.1 GPa at $T = T_{coal}$. Finally, at $T = T_{coal} + 5$K, E is again reduced to 0.01 GPa. Linear interpolation is used between the various points on the graph. This step-wise transition in the semi-solid is used in order to simulate the transition from a coherent semi-solid at temperatures below T_{coal} to one that is dominated by viscous-like flow at temperatures above T_{coal}.

The variation in the coefficient of thermal expansion, shown in figure 4.5, requires further explanation. The Abaqus FE code requires the use of a temperature dependent total thermal expansion coefficient. This can be thought of as the average or equivalent thermal expansion coefficient over the range of interest as shown below:

$$\alpha(T) = \frac{\alpha'}{T - T^0} \int_{T^0}^{T} \alpha(T) dt \tag{4.7}$$

where α is the effective thermal expansion, α', the temperature-dependent thermal CTE, and T^0 a reference point specifying the temperature where the material is assumed to have zero strain. In the simulation, it is assumed that the reference temperature corresponds to T_{coal}.

Constitutive Law for Deformation in the Plastic Regime

In order to simulate the evolution in σ and ε during DC casting, a constitutive law is needed to relate deformation (ε) to the material response (σ). The constitutive law is divided into 3 segments as a function of temperature. These segments are described below:
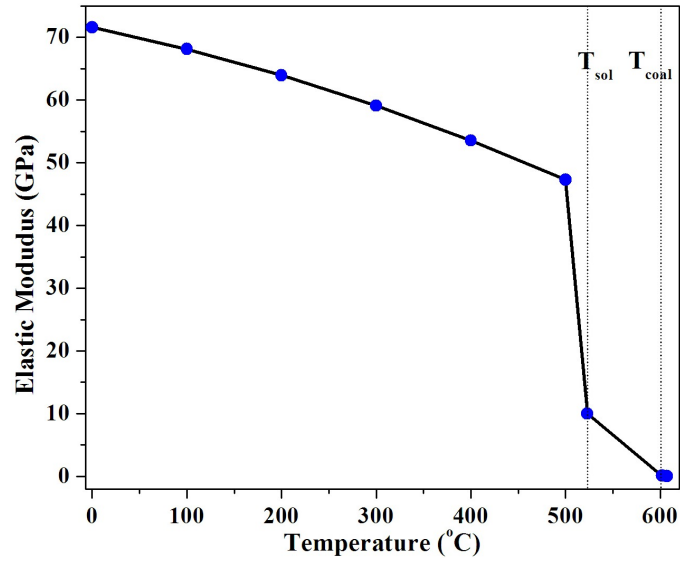
Figure 4.4: Variation of elastic modulus (E) as a function of temperature for $T_{coal} = 602^oC$
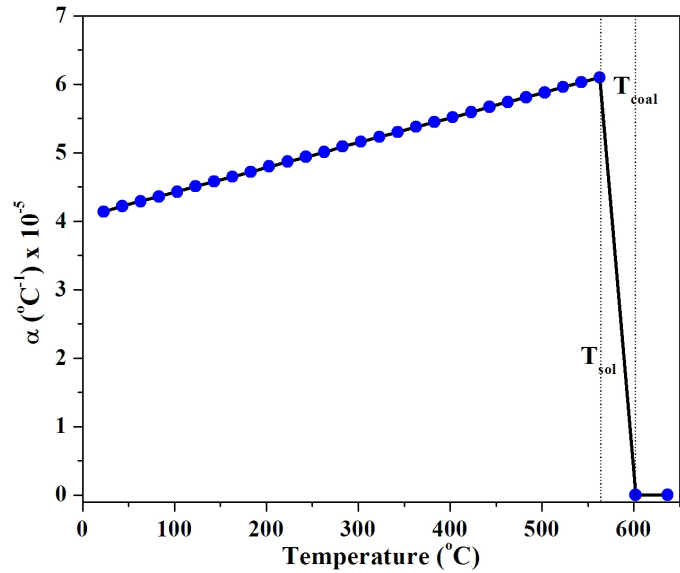
Figure 4.5: Variation of thermal expansion coefficient (α) as a function of temperature for $T_{coal} = 602^oC$
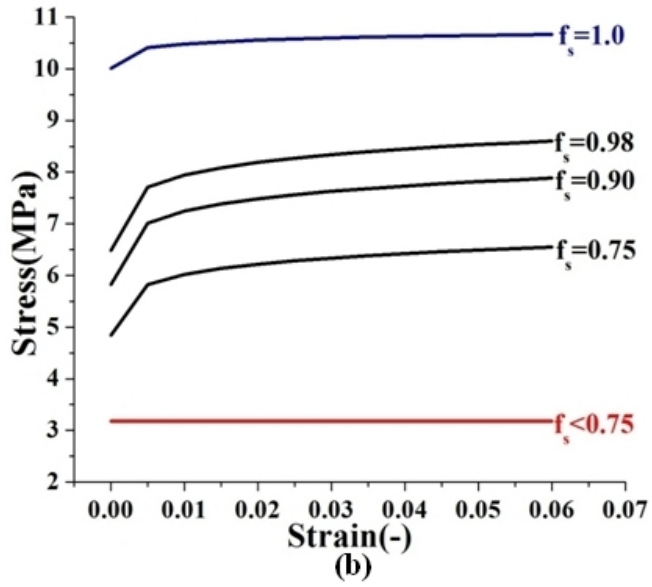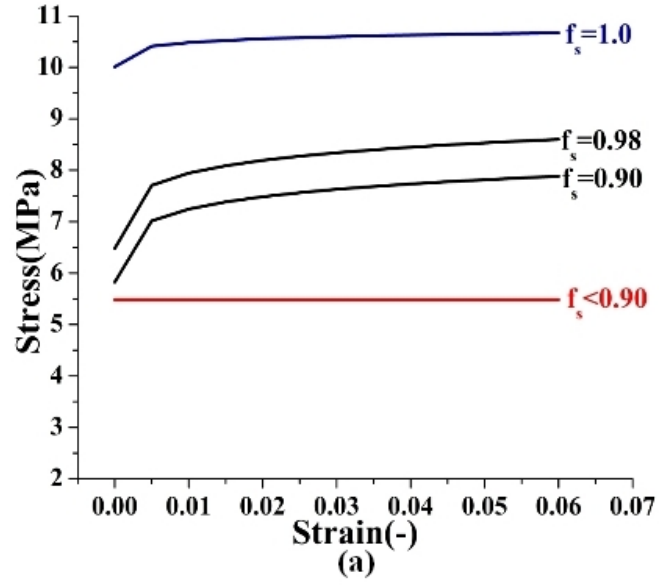
Figure 4.6: Semi-solid stress/strain response used in the simulation at different f_s, (a) for $f_{s,coal} = 0.90$ (b) for $f_{s,coal} = 0.75$. For both (a) and (b), $\bar{d} = 150\mu m$ and $\dot{\varepsilon} = 10^{-3}$ (Equation 4.9-4.12)

Table 4.2: Parameters of the modified Ludwik equation

Parameter	Temperature range(^{o}C)	Temperature dependent equation
K (MPa)	$25 \leq T < 331$	$-0.3409T + 361.83$
	$331 \leq T \leq 500$	$-1.1015T + 613.59$
n	$25 \leq T < 206$	$-0.0003T + 0.170$
	$206 \leq T < 361$	$-0.0007T + 0.252$
	$361 \leq T \leq 500$	0
m	$25 \leq T < 183$	0
	$183 \leq T < 361$	$0.001T - 0.183$
	$361 \leq T \leq 500$	$0.0003T + 0.069$

Constitutive Law Below Solidus

At temperatures below T_s, the modified Ludwik equation developed by Alankar and Wells (2010) was chosen to simulate the constitutive behavior of the alloy, as shown in equation 4.8. This equation is well suited to describe the transition from time independent plasticity at low temperatures (strain hardening) to time-dependent plasticity (visco-plasticity) at high temperatures, since the rheological parameters $K(T), n(T)$, and $m(T)$ are continuous functions of temperature. The values for these parameters are shown in table 4.2. Note that, the equation 4.8 is only valid only up to 500°C. Between temperatures 500 and T_{sol}, the constitutive behaviour is assumed to be a linear interpolation between values obtained by equation 4.8 at 500°C and equation 4.9 at $T_{sol} = 523^{o}$C (from the semi-solid deformation behaviour).

$$\sigma(T, \varepsilon, \dot{\varepsilon}) = K(T)(\varepsilon_p + \varepsilon_{P_0})^{n(T)}(\dot{\varepsilon}_p + \dot{\varepsilon}_{P_0})^{m(T)} \tag{4.8}$$

Constitutive Law Between Solidus and Coalescence Temperature

Within the temperature range $T_s < T < T_{coal}$, the constitutive behavior is modeled according to the model proposed by Phillion et al. (2009) as shown below:

$$\sigma(f_s, f_p, \bar{d}) = f_s \sigma_s (\varepsilon_p + \varepsilon_0)^{n_{ss}(T)} K_p (1 - \frac{f_p}{1 - f_s}) \tag{4.9}$$

with,

$$\sigma_s = (483.5 - 0.77T)\dot{\varepsilon}_p^{(0.205 + 0.00006T)} \tag{4.10}$$

$$h = \bar{d}(1 - f_s)^{\frac{1}{3}} \tag{4.11}$$

$$n_{ss} = -6.35e^{-4}h^2 + 0.0202h \tag{4.12}$$

where K_p is a parameter related to the fraction porosity, f_p, σ_s is the solid flow stress (MPa) of type elastic-perfectly-plastic, $\bar{d}$ is the grain size, h is the thickness of the liquid channels between grains, and n_{ss} is a strain hardening parameter related to the grain size of the solid skeleton. The phenomenological expression for n_{ss} has been determined based on regression analysis of semisolid tensile deformation experiments and microstructure simulations. This formulation enables a link between the semisolid microstructure and the resulting constitutive behavior. The resulting semisolid stress-strain relationships for AA5182 are presented graphically in figure 4.6 (a) for various fractions of solid, and (b) for various grain sizes. As can be seen, the semisolid strength increases with increasing f_s and yet decreases with increasing $\bar{d}$. The strain hardening that occurs is a phenomenon of semisolid deformation has been previously observed both experimentally (Ludwig et al. 2005b) and through simulation (Phillion et al. 2008).

Constitutive Law Above the Coalescence Temperature

Above the coalescencente temperature (T_{coal}), a low constant yield strength is specified . This constant yield strength is the stress calculated by the equations 4.9- 4.12 for $T = T_{coal}$. Examples of these can be seen graphically in figure 4.6.
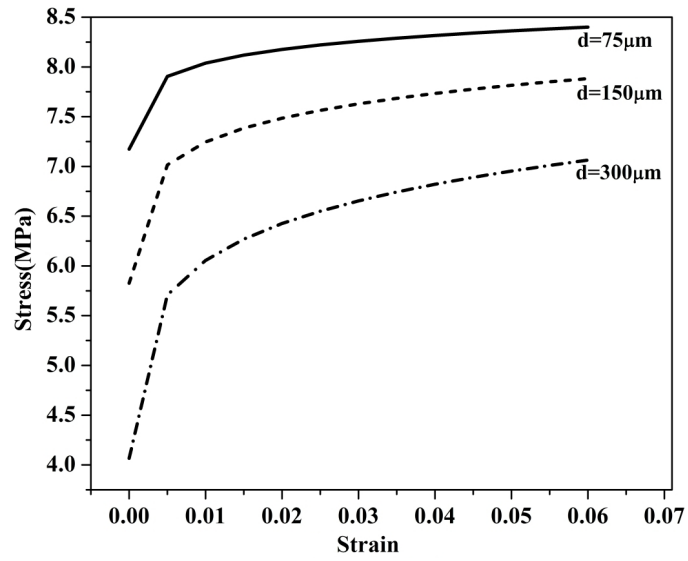
Figure 4.7: Semi-solid stress/strain response according to Phillion et al. (2009) for different $\bar{d}$, at $f_s = 0.98$ and $\dot{\varepsilon} = 10^{-3}$

.
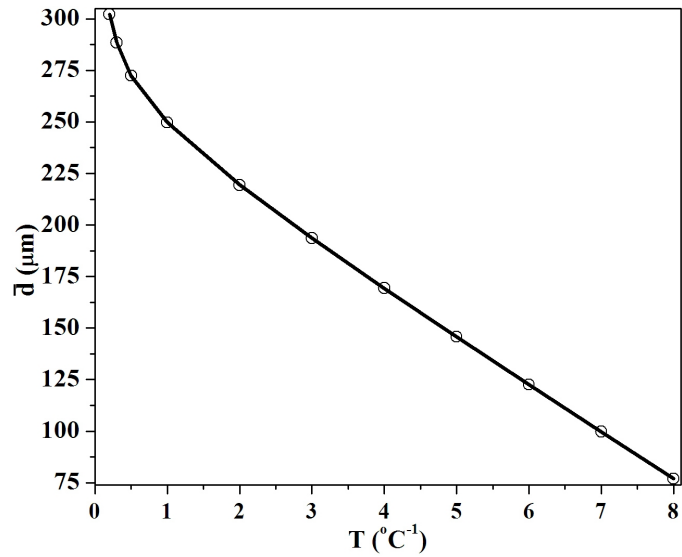
Figure 4.8: Effect of cooling rate on grain size $(\bar{d})$ in AA5182, after Easton et al. (2010).

4.6 Simulation Parameters

4.6.1 Microstructural Features

Grain Size

The constitutive law used for semi-solid deformation includes the effects of microstructure and its evolution, i.e. average grain size ($\bar{d}$). The variation of the semi-solid stress/strain response as a function of $\bar{d}$ is shown in figure 4.7. The presence of variable cooling conditions as the cast surface results in different zones of the casting domain solidifying at different rates and hence different grain sizes. The main driving force behind gradient in grain size across the casting domain is taken to be the average cooling rate between temperatures T_{coal} and T_{liq}. Other factors influencing grain size are ignored. Thus, the local average grain size can be calculated using the methodology of Easton et al. (2010), which is based on the growth restriction factor, and equations 4.13, 4.14 and 4.15. The growth restriction factor (Q) for alloy AA5182 is calculated using the nominal composition of the alloy. The fitting parameters 'a' and 'b' are dependent on the cooling rate($\dot{T}$) and taken from Easton et al. (2010). The variation of average grain size with cooling rate for aluminum alloy AA5182 is shown in figure 4.8.

$$\bar{d} = a + \frac{b}{Q} \tag{4.13}$$

$$b = 281 + \frac{381}{\dot{T}^{\frac{1}{2}}} \tag{4.14}$$

$$a = -22.08\dot{T} + 222.88 \tag{4.15}$$

Variation in Mechanical Coalescence Temperature

The model predictions are also highly sensitive to the choice of coalescence temperature. This parameter directly affects many of the mechanical properties including the thermal

expansion coefficient as this will affect the onset of thermal contraction, the elastic modulus as this will affect the onset of the stiffness, and the semi-solid constitutive law. In this model, two T_{coal} are used, 580°C (0.90) and 602°C (0.75). The corresponding volume fraction solids (f_s) are shown in the parentheses. Campbell (1991) reported that if there is any deformation induced to the semi solid due to thermal stress, etc. above T_{coal}, cracks occurring due to strain will be healed by interdendritic flow of liquid. Thus, temperatures above (T_{coal}) should not be considered for hot tearing study. In the current model, when a T_{coal} of 602°C is assumed, a low constant σ_y is used below the corresponding $f_s = 0.75$ as shown in figure 4.6 (a). The same approach is followed when using a T_{coal} of 580°C, as shown in figure 4.6 (b).

4.6.2 Casting Parameters

Casting parameters play an important role in the formation of solidification defects such as hot tearing. These parameters include :

- Pouring temperature

- Cooling water flow rate

- Casting speed

Among these casting parameters, only casting speed is taken as a variable in this study to observe its effect on hot tear formation since this parameter is the only one to have been found industrially to be relevant for hot tearing. Two casting speeds are investigated: 66 mm/minute, and 40 mm/minute, i.e. values that are typical of fast and slow casting speeds.

4.7 Summary

In this chapter, the details of the process model that has been used to simulate the DC casting process for round billets have been presented. The novelty of the simulation developed for the current masters project are the inclusion of a semi-solid constitutive

law containing stress/strain dependence on grain size, and the prediction of this grain size based on cooling rate effects. The details of these have also been provided in this chapter. Using this process model, simulations were run with the commercial FE package ABAQUS varying different parameters. The stress-strain and hot tearing predictions from this process model under different conditions will be presented in chapter 5.

Chapter 5

Hot Tearing Predictions

5.1 Introduction

We now have an axisymmetric DC casting process model for round billets coupled with a semi-solid constitutive model which includes microstructural features and cooling rate effects. Using this process model, numerous simulations have been run varying the microstructural features and casting parameters using the finite element software ABAQUS (version 6.10). The next task is to relate the stress-strain predictions from this thermo-mechanical process model to hot tearing. To access the relative hot tearing susceptibility as a function of location in the round billet and with respect to casting parameters and microstructural features, a quantitative hot tearing criterion must be applied to the simulation data. This index must be calculated according to the factors known to influence hot tearing. For the current work, a term named "hot tearing strain" is proposed as the index for hot tearing susceptibility and is described in the next section in detail. In the later sections of this chapter, the hot tearing defect in DC casting of round billets is discussed with the help of the simulation data and the hot tearing index.

5.2 Hot Tearing Criteria

For the current project, a term called the "hot tearing strain" is taken as the hot tearing criterion. An overview of the hot tearing criteria available in the literature was summarized in chapter 2. The concept of this hot tearing strain is based on already available strain-based hot tearing criteria in the literature, namely Pellini's total strain criterion (Pellini 1952), Yamanaka's criterion (Yamanaka et al. 1992), observations by M'Hamdi et al. (2002), and Prokhorov's criterion (Prokhorov 1962). All of these researchers have concluded that if the strain accumulated in the semi-solid regime goes above a critical value, then hot tears will form. Hot tearing can then be assessed quantitatively by comparing the strain accumulated in different regions of the casting with a critical value or qualitatively with the philosophy that the higher the hot tearing strain, higher the susceptibility for hot tearing. In this work, hot tearing strain is calculated as the strain accumulated in the brittle temperature region, between the mechanical coalescence f_s^{coal} and the point at which continuous liquid films disappear from the mushy zone ($f_s = 0.98$). In this range, the ductility is very low (Magnin et al. 1996) and thus the semi-solid material is most prone to hot tearing. During the last 2% of the solidification, dendrites have already bridged and thus the structure is able to withstand mechanical loading and resist hot tears. Furthermore, observation made by M'Hamdi et al. (2002) indicated that only the plastic strain is important for hot tearing.

The hot tearing strain is computed as the sum of (1) component of the plastic strain tensor (ε_{ij}^{pl}) normal to the thermal gradient and in the axi-symmetric plane, and (2) the out of plane plastic hoop strain (ε_{zz}^{pl}). The hot tearing strain is calculated as shown in equations 5.1 - 5.5 through a rotation to an angle corresponding to the direction of heat flow.

$$\varepsilon_{ij}^{pl} = \begin{bmatrix} \varepsilon_{11} & \varepsilon_{12} \\ \varepsilon_{21} & \varepsilon_{22} \end{bmatrix} \tag{5.1}$$

$$T = \begin{bmatrix} \cos(\frac{\pi}{2} - \gamma) & \sin(\frac{\pi}{2} - \gamma) \\ -\sin(\frac{\pi}{2} - \gamma) & \cos(\frac{\pi}{2} - \gamma) \end{bmatrix} \tag{5.2}$$

$$A = T \times \varepsilon_{ij}^{pl} \times T' \tag{5.3}$$

and,

$$\varepsilon_{HT} = A_{11} + \varepsilon_{zz}^{pl} \tag{5.4}$$

$$\varepsilon_{HT}BTR = \varepsilon_{HT}(@f_s^{coal}) - \varepsilon_{HT}(@f_s = 0.98) \tag{5.5}$$

Where, γ is the rotation angle between the X-axis and the direction of the thermal gradient, T is the transformation matrix, ε_{HT} is the hot tearing strain, and $\varepsilon_{HT}BTR$ is the hot tearing strain accumulated in the brittle temperature region (BTR).
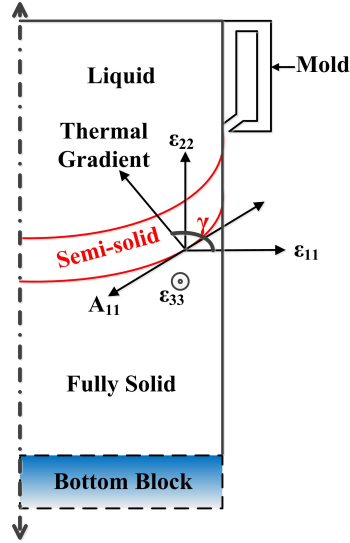
Figure 5.1: Schematic presentation of the strain perpendicular to heat flux in a DC casting billet.

5.3 Simulations for Different Processing Conditions

The process model was simulated for two fixed grain sizes of 300 and 75 μm, for two different mechanical coalescence temperatures of 580 and 602°C, and at two different

Table 5.1: List of simulated processing conditions

Case	Casting Speed	T_{coal}	$\bar{d}$
	mm/min	^{o}C	μm
A	66	602	Eq.4.13
B	66	580	Eq.4.13
C	40	602	Eq.4.13
D	66	602	75
E	66	602	300

casting speeds of 40 and 66 mm/min. With variable grain size (described in chapter 4), 3 additional simulations were run. These 3 simulations are termed cases A, B and C. The simulations run with fixed grain sizes are termed Cases D and E. In total, 5 processing conditions have been modeled to investigate the effects of casting speed, coalescence temperature, and grain size, as outlined in table 5.1. In this table, $\bar{d}$ is the grain size, and T_{coal} is the mechanical coalescence temperature. From here on, case A will be termed as the 'base case'.

5.4 Results and Discussion from the Base Case

The results and discussion of this section will be based on the base case (Case A).

5.4.1 Evolution of Temperature and Hoop-Stress

The FE simulation can be used to provide a detailed description of the evolution of stresses, strains, and temperature during the casting process. In this study, a reference $f_s = 0.98$ is selected to study this evolution of hoop stress. In figure 5.3, the predicted evolution of hoop stress and temperature is provided as a function of time for two different locations within the casting domain for comparison purposes. The hoop stress is shown since it is considered to be the major driving for hot tear formation. Location X is 60 mm above the bottom block and at the centerline, while Location Y is at the same height but just below the cast surface as shown in figure 5.2. As can be seen from figure 5.3, point Y cools much faster as compared to X, owing to the presence of

boiling water heat transfer boundary condition at the surface. Although the evolution of hoop stress at point X is approx. three times slower as compared to Y, the evolution follows the same trend, i.e. close to zero up to T_{coal}, then through a compression followed by an increasingly tensile regime towards the end of solidification and in the solid state.

5.4.2 Contour Plots

In figure 5.4, two contour plots are provided to show the distribution of $\bar{d}$ and $\varepsilon_{HT}BTR$ during casting. The section shown is 400 mm in height and 160 mm in radius. As can be seen in figure 5.4a, $\bar{d}$ varies from 175 to 275 μm, with the largest grains predicted to form just above the base of the casting. These predictions agree relatively well the results found experimentally by Suyitno (2005) for billets that have not been grain refined. The contour plot of $\varepsilon_{HT}BTR$, shown in 5.4b indicates that only a small portion of the billet actually undergoes tensile strain in the brittle region, near the base of the billet and both along the centerline and at the surface. Thus, once the casting has successfully completed the start-up region, hot tearing is not an issue. The compressive strains seen further up are a result of the combination of thermal contractions upon cooling and the aggressive surface cooling.

Figure 5.5a shows the temperature contour plot of the billet cross-section at the end of the simulation (728 seconds). The pool of liquid has a red appearance in figure 5.5a. The hoop stress distribution is shown in the billet cross section is shown in figure 5.5b, which was also taken at the end of the simulation. Hoop stress is very high at the surface and the center as shown by the figure, ranging between ¬249 and +251 MPa. Moreover, there is only a slight variation in the distribution of the hoop stress except at the ends which is an indication that the casting has reached the steady state. The billet center is in tension but high compressive stresses have concentrated at the surface. This type of tension and compression stress regime arises due to the high cooling rates imposed during the process. This effect is also known as the "skin-core" (Drezet and Rappaz

1996b). The cooling conditions applied at the surface cools the surface down very fast and creates an external shell. The interior is still hot, whereas the shell has cooled. This solidified shell counteracts the contraction of the hot core and results in the high tensile stresses at the centre (251 MPa). This effect has also been reported to have appeared during the quenching of heat treatable alloys (Heymes et al. 1997) and considered to be one of the causes of crack formation during casting (Boender et al. 2004, Lalpoor et al. 2009).

5.4.3 Identifying the Startup and the Steady-State Regions

In chapter 1, the DC casting process was divided into three regions from a phenomenological point of view. The first stage is the startup phase, where the thermal fields are not stationary, but can vary with position and time. At higher distances from the bottom block into the casting, there exists the steady state, where the thermal and other fields are stationary, i.e. invariant with respect to time and location. From a hot tearing point of view, it is critical to identify the startup and the steady state regions of DC casting. The reason behind this is two-fold. First, hot tearing is seen industrially to occur in the startup phase of the casting process. Second, the set of casting parameters needed to avoid hot tearing for the startup and the steady state region are different.

The DC casting simulation model developed for this project is well described both in terms of thermal and mechanical considerations. In order to distinguish between the startup and the steady state in this simulation, the temperature profile of different locations need to be examined. For the base case, temperature vs. time data at different distances along the centerline have been extracted from the simulation, as shown in figure 5.6. Note that, for each location, the time t = 0 sec corresponds to the time when the corresponding layer has been added (activated) in the simulation. In this figure, it is seen that the temperature profile of the first 2 locations (0, 100 mm) are farthest apart from each other. This range denotes the startup stage of the casting process. As the

61

distance from the bottom block increases, the temperature profiles start to come closer to each other. At and beyond 400 mm distance from the bottom block, the temperature profiles start to overlap each other. Thus, after the billet has been cast for about 400 mm height, it reaches a steady state at the centerline.

Now, lets turn our attention towards what happens along the chill surface of billet in the simulation. The temperature profiles of different locations along the chill surface of the billet from the simulation are summarized in figure 5.7. A very interesting difference as compared to the temperature profiles for the centerline is revealed in this figure. The temperature profiles at the points on the surface start merging at around 100 mm away from the bottom block. Thus, the steady state is achieved only within 100 mm away from the bottom-block. The thermally transient state lasts for only the first 100 mm for points on the surface. It seems that, faster cooling regimes (surface) tend to shift the steady state region to much lower heights. This variation of attainment of steady state has important implications with respect to the hot tear formation in the DC casting process.

The steady state regime can also be identified from a mechanical point of view. The evolution of hoop stress (σ_H) in the vertical direction as a function of distance from the bottom-block is shown in figure 5.8. The hoop stress values at different locations have been taken at the time when the point has reached a fraction solid of 0.98. Close to the bottom-block, the stress is negative (-10 MPa), and as the distance from the bottom-block increases, the hoop stress starts to increase towards the positive side. At around 80 mm distance from the bottom block, the hoop stress becomes zero. The stress keeps increasing and reaches a maximum value of +2.5 MPa at 100 mm distance. Beyond this point, the stress starts decreasing again, and shifts again to the negative regime after 160 mm. The stress decreases steadily, before reaching a negative plateau of about -13 MPa at and beyond 400 mm distance. The hoop stress field remains relatively constant after

a distance of 400 mm from the bottom block. This distance (400 mm) was identified as the start of the steady state region from the thermal fields shown in figure 5.6. Thus, in addition to the thermal field, the (hoop) stress field also becomes stationary in the steady state.

The hoop stress in the horizontal direction as a function of the distance from the centerline at 12 mm distance from the bottom block is shown in figure 5.9. Similar to figure 5.8, the hoop stress values are taken at the time when the fraction solid of the point is 0.98. At this height, the casting is still in the startup stage. In this startup stage, the hoop stress is compressive near the center of the billet. The hoop stress remains relatively constant at a value of about -9.5 MPa up to 90 mm distance from the center. Further away from the center, the stress gradually increases, and is highly tensile. The stress is highly tensile (+9 MPa) on the surface. This occurs because the surface solidifies rapidly to the cooling of the mould, which tends to 'squeeze' the material within. This squeezing action results in the compressive stresses close to the center.

The variation in hoop stress along the horizontal direction at different distances from the bottom block are shown in figure 5.10. In figure 5.10a (100 mm away from the bottom block), the stress is highly tensile at the center up to about 80 mm from center, but shifts to compressive close to the surface. Similar observations are made at a distance 200 mm from the bottom-block (figure 5.10b). If we compare the maximum tensile stresses achieved in figures 5.10a and 5.10b, we see that the maximum tensile stresses achieved in both cases are similar. But location of maximum stress for these 2 cases are different. The maximum stress at x = 100 mm is observed at the center, but at x = 200 mm, it is seen at 40 mm from the center. Thus, the maximum tensile hoop stress moves away from the center as we go further up the billet. Moreover, at the center, the hoop stress decreases as the top of the billet is approached (compare with figure 5.8).

5.4.4   Evolution of Hot Tearing Strain

In this project, a 'hot tearing strain', as discussed in section 5.2, has been used as the criterion for hot tear evaluation in DC casting billet. Tensile (positive) hot tearing strain would mean susceptibility to hot tearing. But, compressive (negative) hot tearing strain would mean no susceptibility to hot tearing. In fact, compressive hot tearing strain should help to heal the hot tears by directing the fluid flow into areas where feeding is inadequate. The variation of hot tearing strain as a function of distance from bottom block along the centerline of the billet is shown in figure 5.11. As seen in the figure on the top, the hot tearing strain is compressive close to and also further away from the bottom block. Only at 4 to 8 mm from the bottom block, the strain goes through a tensile region, which can be seen in the magnified bottom (blue background) figure. Thus, this region (4-8 mm distance) close to the bottom block at the centerline is most prone to hot tearing. The hot tearing susceptibility reduces considerably further away from the bottom block.

Another salient feature of this curve is the noise associated with it, which is seems to have exacerbated after 100 mm distance from the bottom block. The main reason behind this noise is the incremental addition of layers. The addition of a layer causes the bulk stiffness of the structure to change, and thus acts to induce fluctuations in the value of the strain tensor. Another cause of this fluctuation could be addition of layers from another aspect. The layer being added has a flat surface, but the layer added in the previous time step has cooled and is no longer flat due to contraction. So, the addition of the flat surfaced layer on the contracted surface could also contribute to this noise.

Hot tearing strain in the horizontal direction 8 mm away from the bottom block is shown in figure 5.12. The hot tearing strain is tensile at the center, but gradually decreases to zero at around 10 mm from center. Further away from the center, hot tearing strain is compressive. But, between 100 - 160 mm from the center (close to and at the surface), the hot tearing strains have small tensile values. From these two observations of

tensile strains, it can be concluded that the center of the billet close to the bottom block is highly susceptible to hot tear formation. Furthermore, to a lesser degree the surface close to the bottom block may also be susceptible to hot tearing.

So far, we have looked at variation in hot tearing strain in the horizontal direction very close to the center. Now, lets look at hot tearing strain along horizontal lines higher up the billet. The horizonal evolution in hot tearing strain at different heights are shown in figure 5.13. If we look at the strain further into the casting, at both x = 100 mm (figure 5.13a) and at x = 200 mm (figure 5.13b), the strain regime is exclusively compressive. So, at these heights, the casting is not susceptible to hot tearing at all. Similar trends are seen in both these figures, i.e. the strain is highly compressive at the center and gradually changes to a less compressive value close to the surface of the billet. From these figures, it can be concluded that only the region close to the centerline and bottom block of the billet are susceptible to hot tearing. At higher distances from the bottom block, the hot tearing tendency diminishes. The other important feature of the strain evolution at x =100 and 200 mm, are there is considerable noise in the evolution in hot tearing along the cross-section. As discussed earlier, this is most probably due to the changes in stiffness every time a layer is added. Moreover, along the horizontal direction, the noise level seems to be higher at larger heights of the casting.
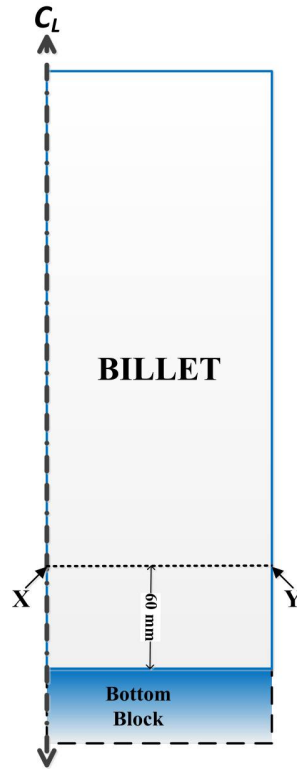
Figure 5.2: Location of X and Y in the casting domain.
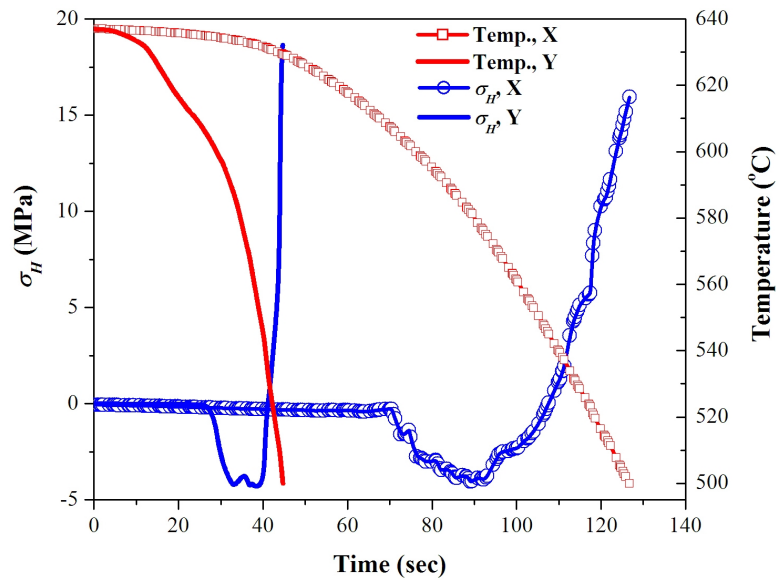
Figure 5.3: Evolution of Temperature and σ_H at locations X and Y with time. For X (Y), t=0 sec. corresponds to t=78.33 (57.50) sec. after the start of casting.
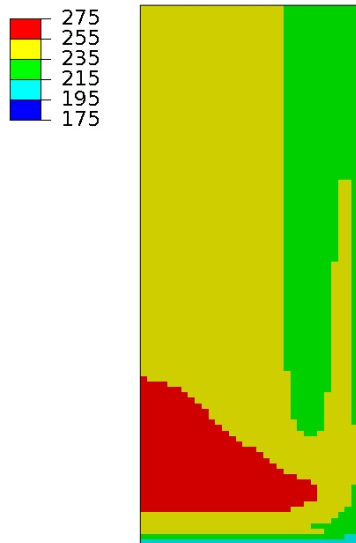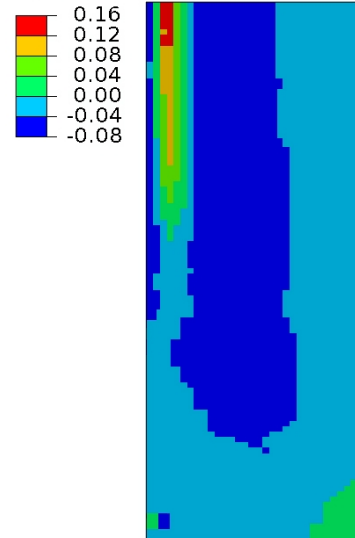
(a) Grain Size

(b) Hot Tearing Strain

Figure 5.4: Contour plots from Case A showing (a) Grain size, and (b) Hot tearing strain
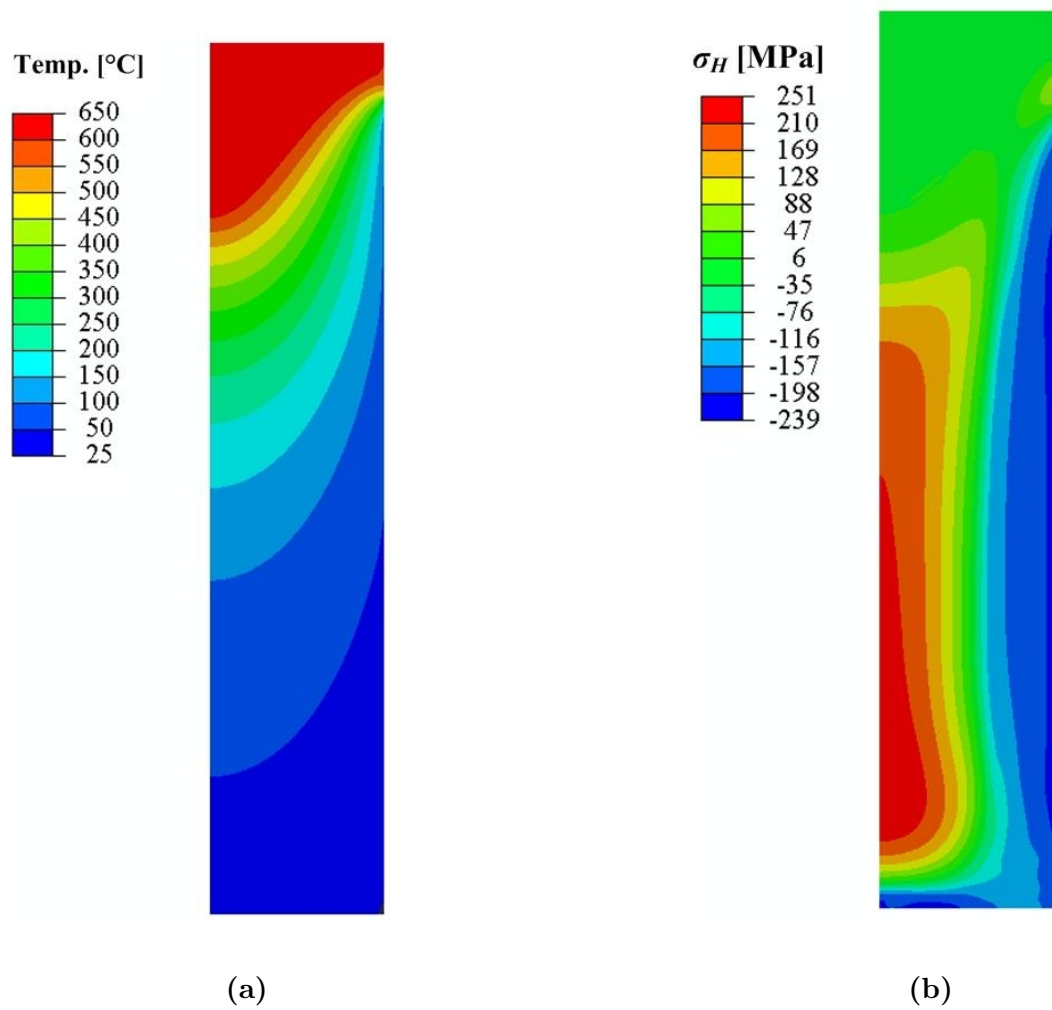
Figure 5.5: (a) Temperature field of the billet, and (b) Contour plot of hoop stress (σ_H) at the end of the simulation (after 728 seconds)
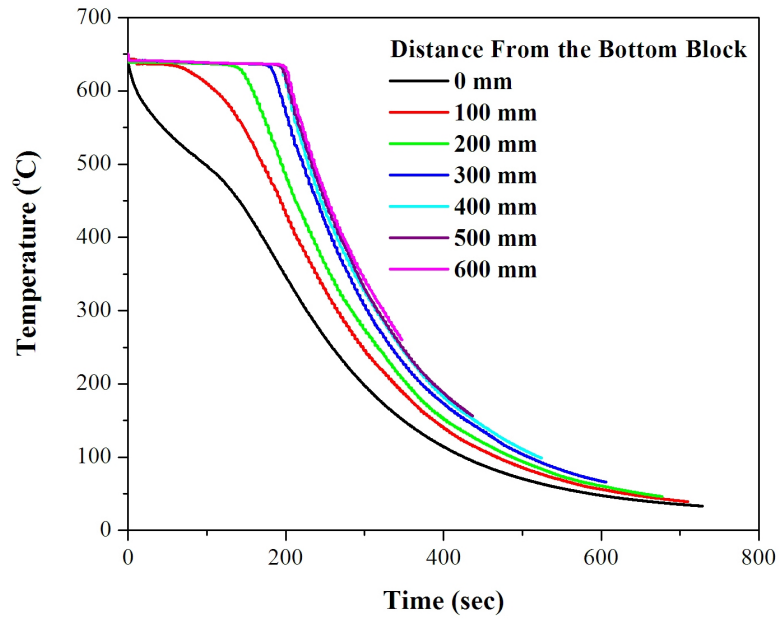
Figure 5.6: Temperature profile at different locations along the centerline of the billet
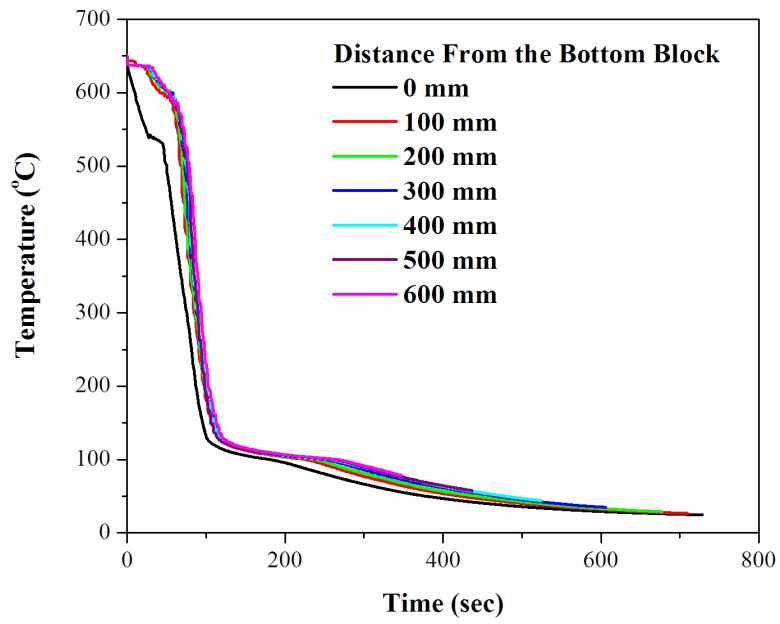
Figure 5.7: Temperature profile at different locations along the chill-surface of the billet

69
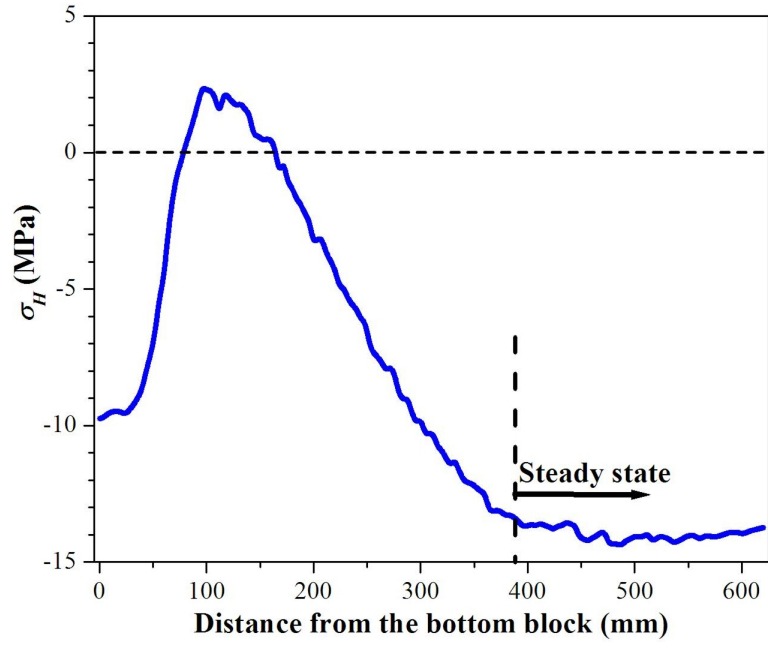
Figure 5.8: Variation of σ_H as a function of distance from the bottom block along the centerline
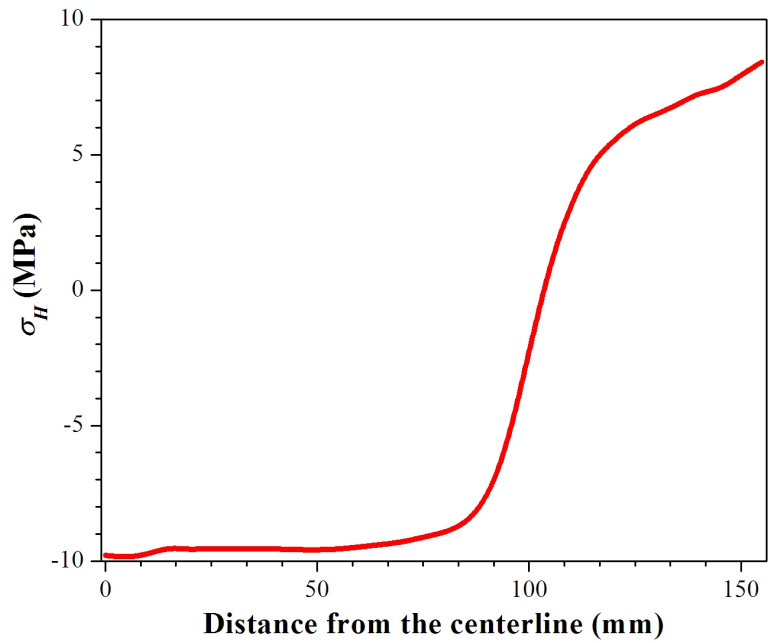
Figure 5.9: Variation of σ_H in the horizontal direction as a function of distance from the centerline at 12 mm distance from the bottom block

(a) x = 100 mm
(b) x = 200 mm
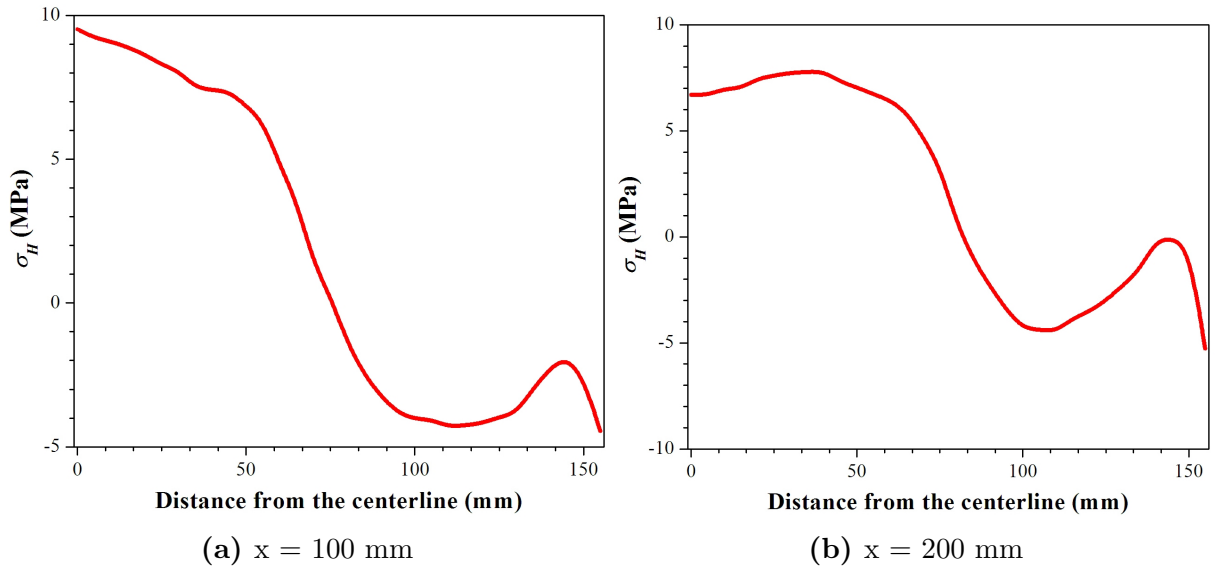
Figure 5.10: Variation of σ_H in the horizontal direction as a function of distance from the centerline at different distances from the bottom block, where x = distance from the bottom block
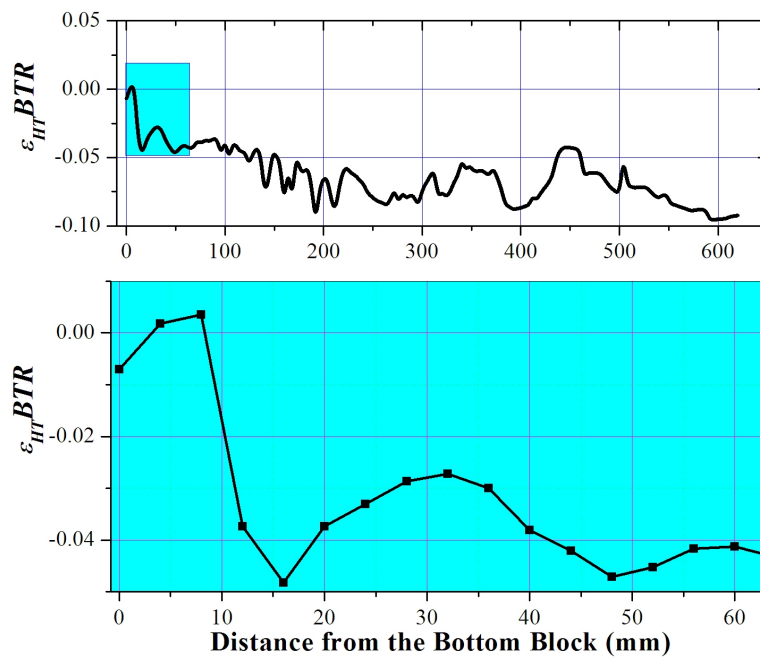
Figure 5.11: Variation of hot tearing strain as a function of distance from the bottom block along the centerline of the billet
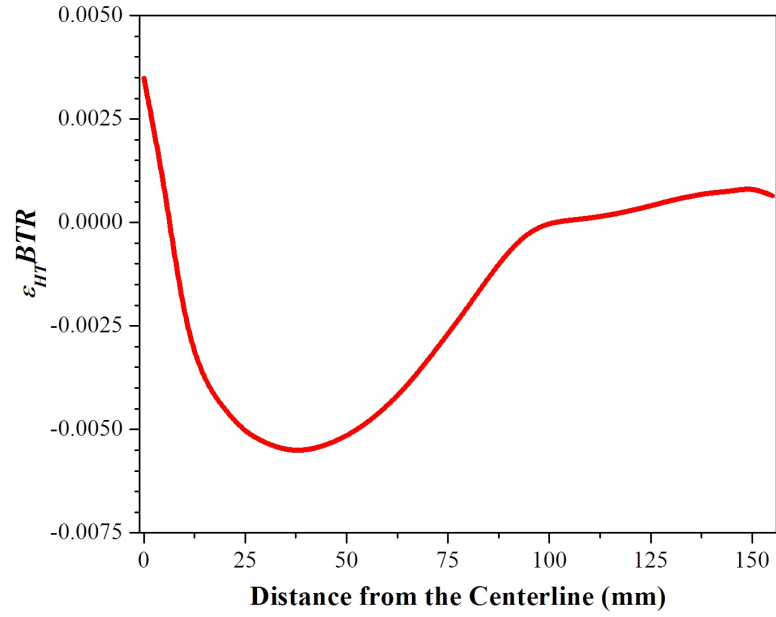
Figure 5.12: Variation of hot tearing strain as a function of distance from the centerline along the horizontal direction, 8 mm away from the bottom block

(a) x = 100 mm

(b) x = 200 mm
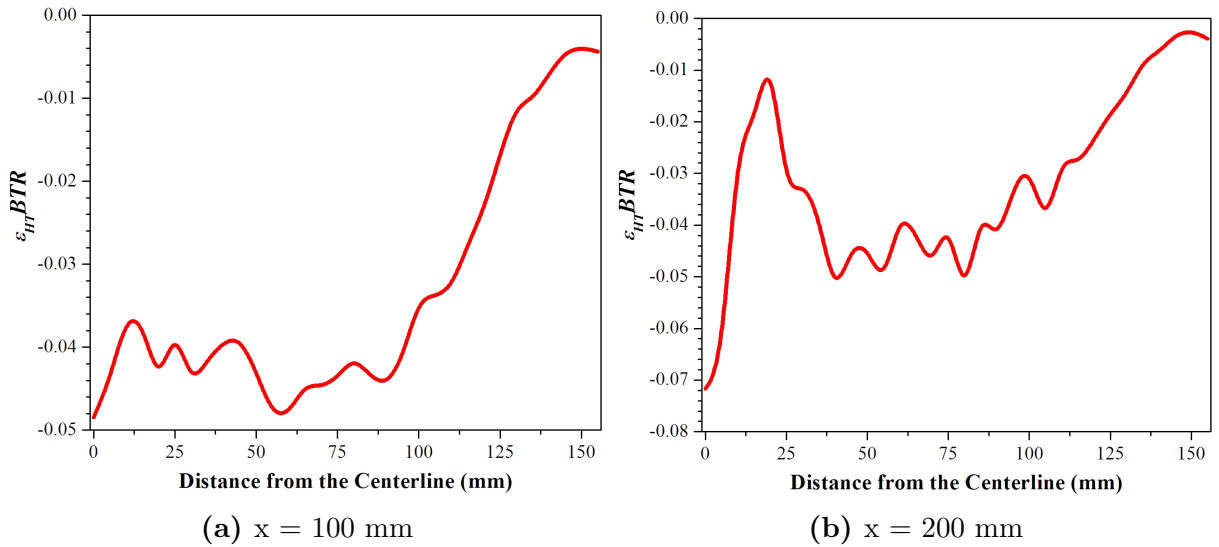
Figure 5.13: Variation of hot tearing strain in the horizontal direction as a function of distance from the centerline at different distances from the bottom block, where x = distance from the bottom block

5.5 Effects of Microstructural Features and Processing Parameters

Up to this point, we have limited our discussion to the results obtained from the base case. In this section, we will be exploring the other cases (B - E). Based on the results from these simulations, the effect of microstructural features on stress and strain predictions will be discussed in detail.

5.5.1 Effect on the Hoop-Stress

Effect of Grain Size

Figure 5.14 shows the variation of hoop stress along the horizontal direction at a height 8 mm from the bottom block and at $f_s = 0.98$ for three simulations with both variable $\bar{d}$ (Case A) and fixed $\bar{d}$ [cases D (175 μm) and E (300 μm)]. As can be seen, σ_H is compressive close to the base of the billet and then gradually shifts to the tensile regime further away. The hoop stress is maximum both in the tensile (at surface) and compressive (at center) for the simulation with case A. Conversely, the lowest stress is seen for the simulation of case A (variable grain size). Note that the grain size range is 175 - 275 μm for case A simulation (shown earlier through a contour plot). Finally, the stress levels for simulation of case D lies in between case A and E. The stresses generated in the casting body for these simulations vary with grain size, and there seems to be a direct relation between stress and grain size if we consider cases D and E only. But, the high stress generated for the case A needs more attention. The variable grain size is somehow changing the strength of the casting at $f_s = 0.98$, and resulting in a relative higher stress.

Figure 5.15 shows the variation in hoop stress at different heights of the billet along the centerline, taken at $f_s = 0.98$ for the three simulations A, D, and E. The highest tensile stress is reached at close to the top of the casting. Though the highest compressive stress is observed for case A, but the highest tensile stress is observed for case E, the lowest grain size simulation. The lowest tensile hoop stress observed for case E. In terms

of reaching the steady state from a mechanical point of view, both the fixed grain size simulations (D and E) reach the steady state much earlier (at around 300 mm) than the variable grain size simulation (at around 400 mm).

Effects of Coalescence Temperature and Casting Speed

Figure 5.16 is provided to demonstrate the effects of coalescence temperature and casting speed on hoop strain variation in the vertical direction at $f_s = 0.98$. In this figure, where the vertical variation of hoop stress along the centerline is shown, we can see that the highest stresses are observed for the case B simulation (Low T_{coal} of 580^oC). The low T_{coal} means that the coalescence temperature is much closer to the temperature at with the hoop stresses are taken (corresponding to $f_s = 0.98$) compared to higher assumed $T_{coal}=602^oC$ for the base case. So, the strength is much lower for the casting using case B parameters. The lowest stresses are seen for simulation with base case. But for case C (low speed), the stress never goes through a tensile zone. Moreover, the steady state is achieved for case C much earlier (around 150 mm) than case A and B. The early attainment of steady state is related to the casting speed by the depth of the sump. Weckman and Niessen (1982), Zheng et al. (2011) experimentally showed that the depth of the sump during DC casting of billets increases with the casting speed. An increase in depth of the sump thus delays the attainment of steady state. The early achievement steady state for the low casting speed indicates that it spends relatively less time in the transient startup state, which is believed to be the zone where the hot tears form. So, low speeds would have low hot tearing susceptibility, as compared to casting with high speed (base case).

5.5.2   Effect on Hot Tearing Strain

Effects of Grain Size

Figure 5.18 shows the variation of hot tearing strain for in the vertical direction along the centerline as a function of the distance from the bottom block for fixed (D and E)

and variable (A) grain size simulations. As can be seen from the figure, there is some variation of evolution of hot tearing strain due to variation in grain size. The maximum tensile strain arises at around 8 mm from the bottom block for all three simulations. Although it is not clear from the figure because of the scales used in Y axis, the highest tensile strain occurs for case E (highest grain size). The hot tearing strain in the startup region (up to 25 mm height) is shown in figure 5.19. The lowest strain is achieved for case E. Moreover, the maximum tensile strain for the fixed grain sizes are observed at 4 mm away from the bottom block, but the maximum strain achieved for the variable grain size simulation is at 8 mm away from the bottom block. Thus, the hot tearing susceptibility is observed for the highest grain size, but the minimum minimum hot tearing susceptibility is is observed for the variable grain size simulation with grain sizes in the range of 175 - 275 μm. The lowest grain size simulation (case D) shows maximum tensile strains with values in between case A and E. It is expected that a structure with larger grain size would exhibit higher strains, because it possesses lower strength in the semi-solid range. Conversely, using the same logic, the structure with smallest grain size (case D) should show the lowest strain and consequently lowest hot tearing tendency, because it has the highest strength in the semi-solid. Moreover, if larger grains exist in the semi-solid, the grain boundary area is less than with smaller grains. Consequently, the interdendritic liquid channels become wider for larger grains, which exacerbates the hot tearing problem. Either of these two reasons will contribute to higher resistance to hot tearing for smaller grains. But clearly, it is not the case. This could be due to two reasons. First, it could be due to decrease in differential thermal contractions imparted by the range of grain sizes spread across the billet cross section, which would lead to lower hot tearing susceptibility. Second, it could be due to a term called the 'over grain refinement' effect. This effect postulates that although grain refinement increases the hot tearing resistance in general, but grain refinement below 100 μm actually increases the hot tearing tendency in wrought aluminum alloys.

Figure 5.17 shows the horizonal variation of hot tearing strain at various distance from centerline at 8 mm away from the bottom block for the cases A, D, and E. The maximum tensile strain is shown at the center for all three simulations. The highest hot tearing strain is shown by case E ($d = 300\mu$m) and lowest strain is shown is shown for case D ($d = 75\mu$m). The strain for case A lies in between those of cases D and E. So, along this line, the largest grain size structure is the most susceptible to hot tearing, while the lower grain size structure has the lowest susceptibility. On the other hand, along the horizontal line at 4 mm away from the bottom block, the hot tearing tendency is highest for the largest grain size structure, but the lowest hot tearing susceptibility is shown not by the lowest grain size structure (case D) but by the variable grain size structure. So, the claim made in the previous paragraph that the hot tearing tendency is not the lowest for the lowest grain size simulation holds true for this line at 4 mm from the surface, but not for the horizontal line at 8 mm from the surface. But, in any case, if we consider the highest strain value for the three cases, and not the position, the lowest tendency to hot tear is for the variable grain size structure (case A).

Effect of Coalescence Point and Casting Speed

Figure 5.20 and 5.21 show the effect of variation in coalescence point and casting speed in the evolution in hot tearing strain. First, figure 5.21 shows the hot tearing strain in the vertical direction along the centerline, and second, the hot tearing strain in the radial direction at 8 mm from the bottom block is shown in figure 5.20. Beginning with a modification of the coalescence temperature from 602^oC to 580^oC (Case A to Case B), it can be seen that a reduction in coalescence temperature will increase the hot tearing strain. For the lower coalescence temperature, the semi-solid body is weaker at f_s=0.98, because it is relatively closer to the coalescence temperature at this f_s. Consequently higher strains are observed for simulation with case B.

It can also be seen that only a negligible amount of hot tearing strain is accumulated

when a slow casting speed of 40 mm/min (Case C) is used. In fact, the strain along the radial direction and along the centerline is always compressive for this simulation. For a slower casting speed, the material being cast is in contact with the mold and the spray water for a longer version of time. Thus, there is a small thermal gradient and hence a smaller differential thermal contraction. So, the simulation with lower casting speed is much more resistant to hot tearing, as found previously by Hao et al. (2010) as well as by Drezet and Rappaz (2001). This result will hold as long as the secondary water cooling conditions remain in the nucleate boiling regime. However, a lower casting speed decreases the length of the nucleate boiling zone of secondary cooling (Weckman and Niessen 1982) and tends to shift the secondary cooling regime from nucleate to film boiling. If the cooling conditions are such that film boiling occurs on the surface of the casting, heat transfer is drastically reduced and severe hot tears can form (Sengupta et al. 2005a). An interesting discussion could be commenced on the change of grain refinement scenario by variation of casting speed and its implications on hot tearing. The higher casting speed should increase the cooling rate and thus, decrease the grain size. As the results from the simulations show that smaller grain size tends to increase hot tearing resistance, also validated by previous experimental work on this topic. But, the hot tearing resistance here is shown to be higher for lower casting speeds. Thus, it seems that the reduction in differential thermal contraction overrides the effects of grain refinement in terms of hot tearing susceptibility. To summarize, the comparison of Cases A, B, and C in Figures 5.20 and 5.21 indicates that larger strains will accumulate in the semisolid when the casting conditions are such that the metal has a lower coalescence temperature and/or the casting speed is elevated.
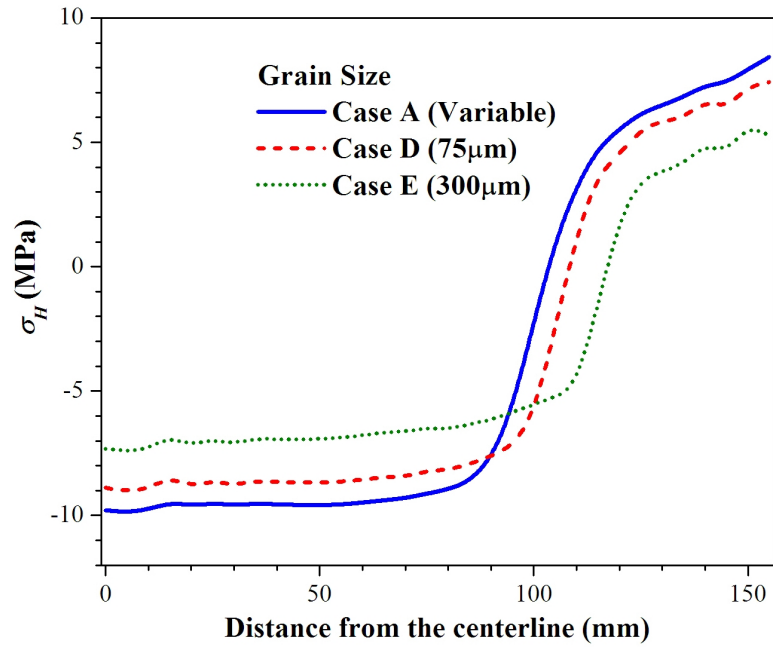
Figure 5.14: Variation of σ_H as a function of distance from the centerline along the horizontal direction, 8 mm away from the bottom block for cases A, D, and E
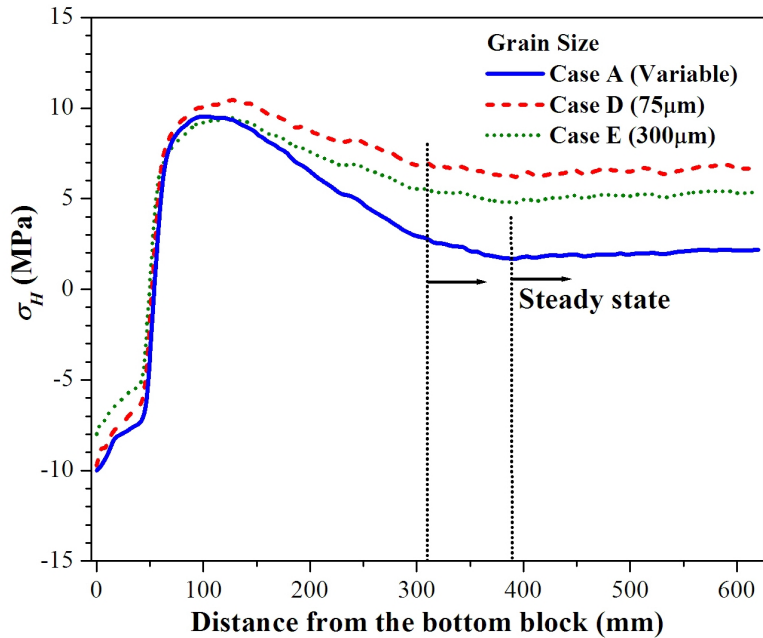
Figure 5.15: Variation of σ_H as a function of distance from the bottom block along the centerline for cases A, D, and E
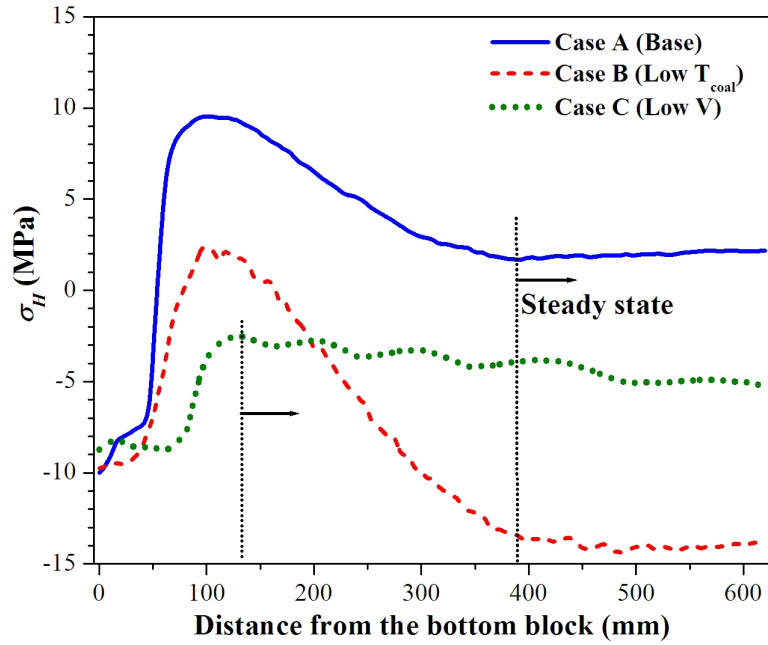
Figure 5.16: Variation of σ_H as a function of distance from the bottom block along the centerline for cases A, B, and C
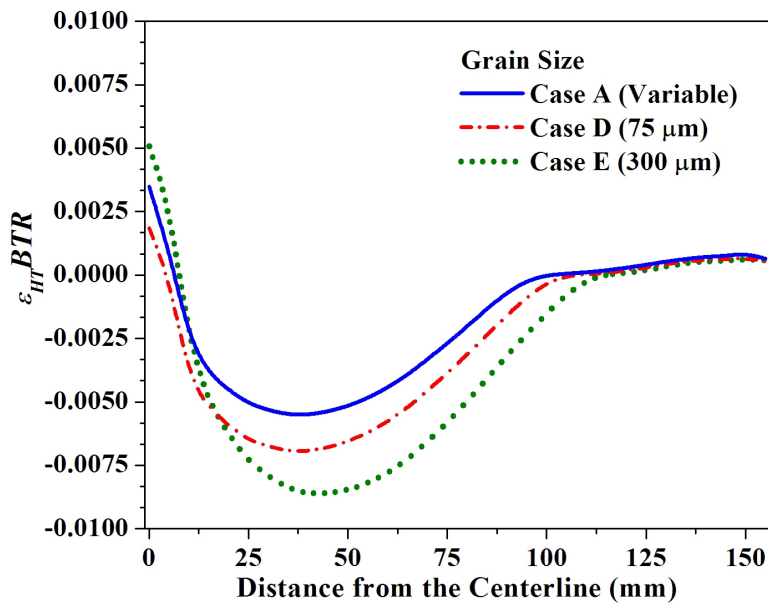
Figure 5.17: Variation of hot tearing strain as a function of distance from the centerline along the horizontal direction, 8 mm away from the bottom block for cases A, D, and E
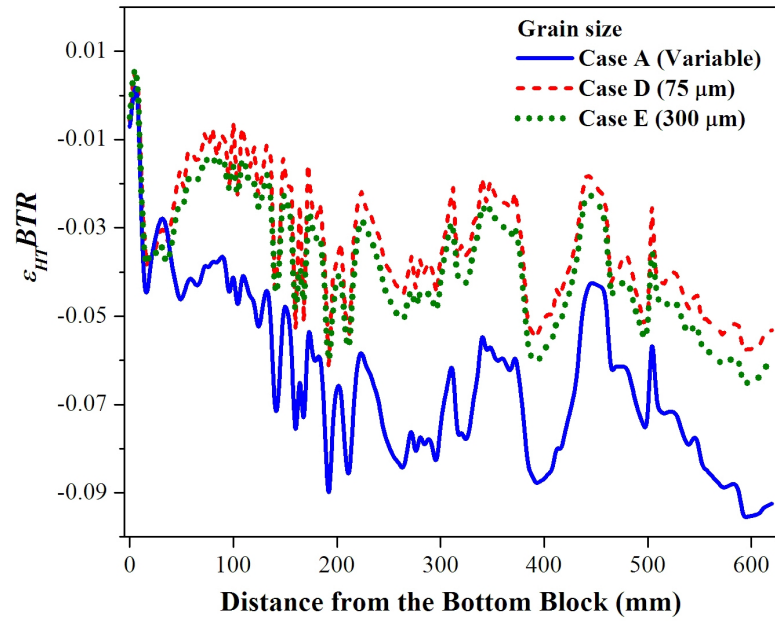
Figure 5.18: Variation of hot tearing strain as a function of distance from the bottom block along the centerline for cases A, D, and E
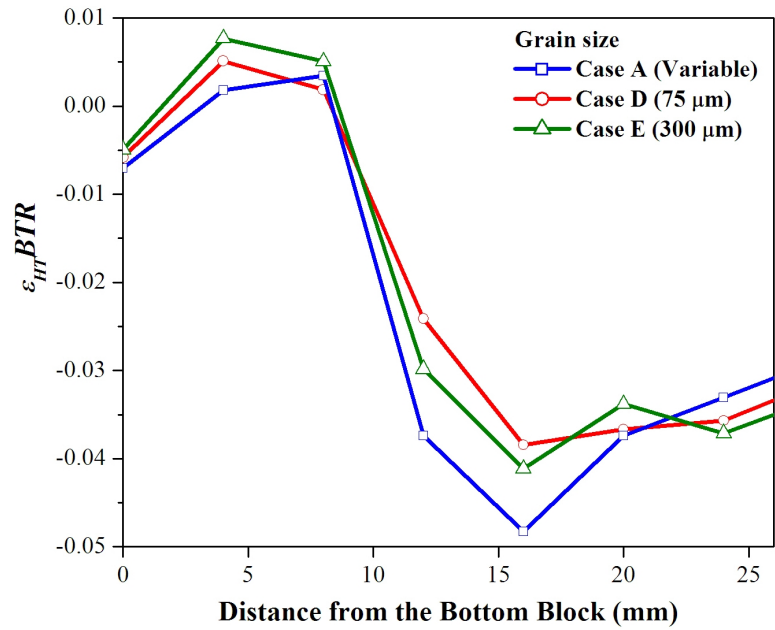
Figure 5.19: Variation of hot tearing strain as a function of distance from the bottom block along the centerline in the startup region for cases A, D, and E
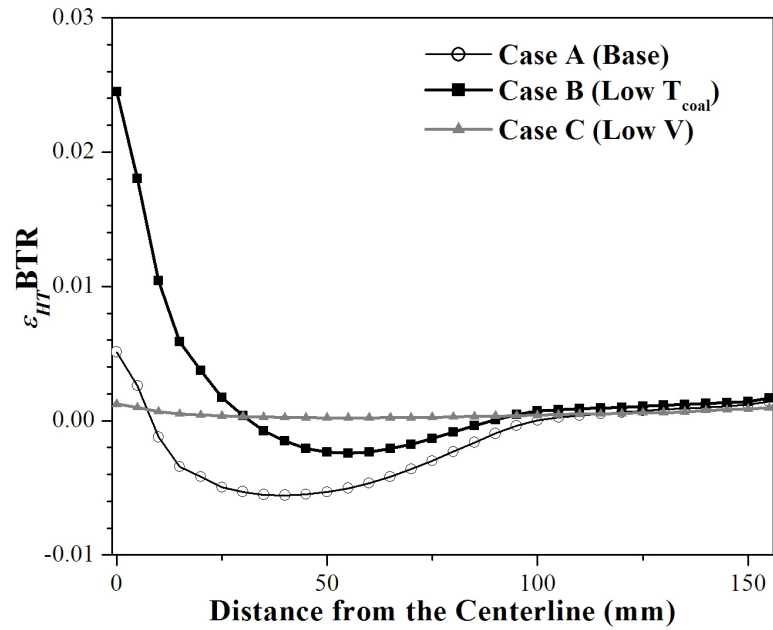
Figure 5.20: Variation of hot tearing strain as a function of distance from the centerline along the horizontal direction, 8 mm away from the bottom block for cases A, B, and C
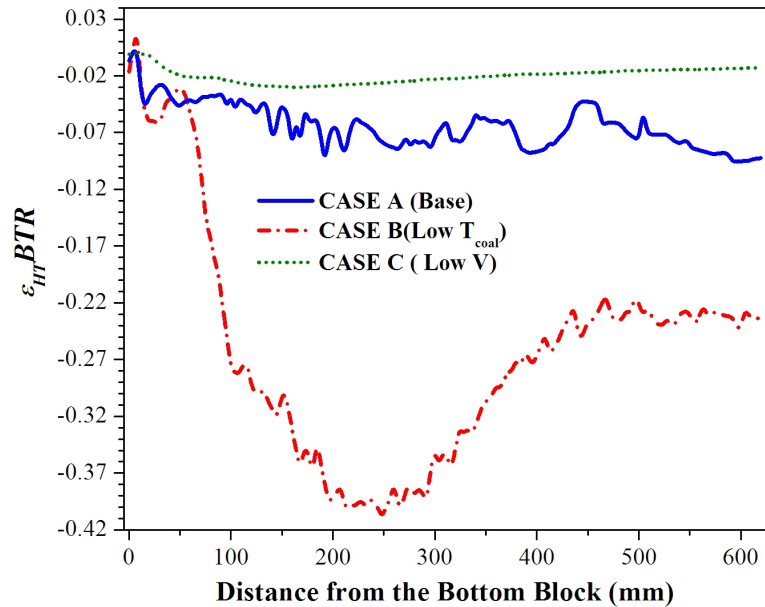
Figure 5.21: Variation of hot tearing strain as a function of distance from the bottom block along the centerline for cases A, B, and C

Chapter 6

Microstructural Analysis of an AA5182 DC Cast Ingot - Experimental Methods

6.1 Introduction

The development of a DC casting process model, and its use in predicting semi-solid deformation and hot tearing were presented in chapters 4 and 5, respectively. The model predictions indicated that grain refinement and solidification characteristics of the alloy, among others have a strong influence on hot tear formation. In order to conduct an experimental study of these factors, an experimental study was carried out to characterize the microstructure of an AA5182 DC cast ingot provided by Rio Tinto Alcan. In table 6.1, the casting parameters used for casting this ingot are summarized. The ingot had cross-sectional dimensions of $l = 1650$ mm, and $w = 510$ mm.

The purpose of this chapter is to describe the methodology used for studying the solidification characteristics of the alloy, the resulting microstructure, and also the effects of cooling on these characteristics. In addition, the methodology for measuring grain size including preparation of metallograpic samples is also reported. The results from these

Table 6.1: Process parameters used for casting the AA5182 ingot piece, obtained from Rio Tinto Alcan

Parameter	Value
Casting Speed	78 mm/min
Water Flow Rate	975 L/min
Casting Temperature	705^oC
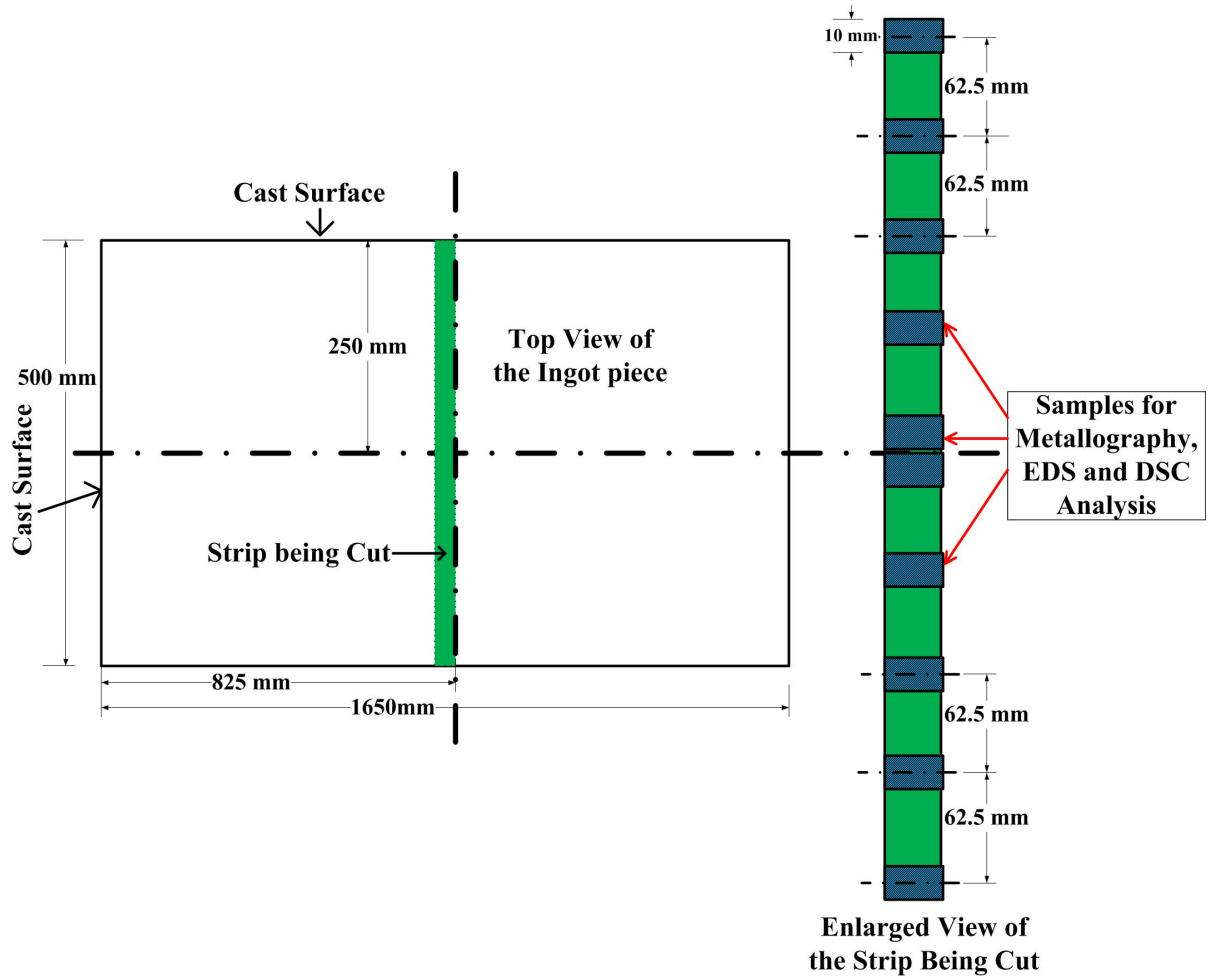
Figure 6.1: Locations in the ingot from where the samples were taken for characterization

experiments will be reported in the following chapter.

6.2 Sample Selection

A number of samples of dimensions 10 mm×10 mm×10 mm were taken along the centre-line of the rolling face, as shown in figure 6.1. For this analysis, a 125 mm section of the ingot was taken from the steady state region of the casting. Samples were then collected for grain size measurements, chemical analysis and for determination of the evolution in fraction solid with temperature.

6.3 Grain Size Measurements

For grain size measurements, metallographic samples were taken as shown in figure 6.1 from different positions along the centreline of the ingot's rolling face. First, the samples were mounted with a thermosetting resin. The mounted samples were then coarse ground, and then polished down to a 1 μm finish with colloidal silica in a automatic metallographic polisher. After cleaning in an ultrasonic cleaner, the samples were then electrochemically etched with Barker's reagent to reveal the grain boundaries. The choice of the etching reagent is important for aluminum alloys because they are very reactive and thus one of the hardest groups of metals to etch properly. Many etching reagents were tried for this project, from hydrofluoric acid (HF) to more caustic NaOH. These regents mostly revealed the general or dendritic structure of the alloy in question, but failed to reveal the grain boundaries. Barker's regent was found to be most effective in this regard. The etched samples were then viewed under polarized light with sensitive tint attachment in a 'Zeiss Axio' metallurgical microscope.

The grain size was measured by Jeffrie's procedure, a standard methodology described in the **ASTM E112**. In this method, a circle of appropriate size (usually 5000mm^2 or with a diameter of 79.8 mm) is drawn on a metallograph image. Magnification is selected so that the circle partially/fully inscribes at least 50 grains. The grain density (with no magnification) is then given by equation 6.1.

$$N_A = f(N_{inside} + \frac{N_{intercept}}{2}) \tag{6.1}$$

where N_{inside} is the number of grains completely inscribed by the circle, $N_{intercept}$ is the number of grains partially inscribed in the circle, and f is known as the Jeffries' multiplier, which is a function of magnification used. Finally, average grain size ($\bar{d}$) is estimated using a table provided in the **ASTM E112** guide that relates grain size with N_A.

6.4 Chemical Analysis

Chemical analysis was carried out using an Oxford Instruments X-max 80 mm^2 energy dispersive spectroscope (EDS) attached to a Tescan Mira 3 XMU scanning electron microscope (SEM). Each of the samples shown in figure 6.1 was analyzed using SEM-EDS. For each sample, an EDS signal was acquired on 10 to 12 rectangular subregions, each with a dimension of approximately 100μm$\times 100\mu$m. The compositions of each element from different locations within the same sample were then averaged to represent the bulk composition of that element within that sample.

6.5 Solidification Kinetics

Characterization of the solidification kinetics within the DC cast AA5182 ingot was carried out by performing Differential Scanning Calorimetry (DSC) measurements on a series of small specimens in a similar location to the specimens for grain size measurement and chemical analysis using a Netzsch STA 449 F3 apparatus. This DSC apparatus consists of two different furnaces - (a) SiC furnace operating between 25^oC and 1500^oC, and (b) Steel furnace operating between -150^oC to 1000^oC. Both furnaces were used as part of this study in order to achieve various heating and cooling rates, in combination with N$_2$ gas and liquid N$_2$. In this apparatus, small samples between 15 and 25 mg are heated and cooled at a controlled rate in a crucible. The thermocouple attached to the sample carrier
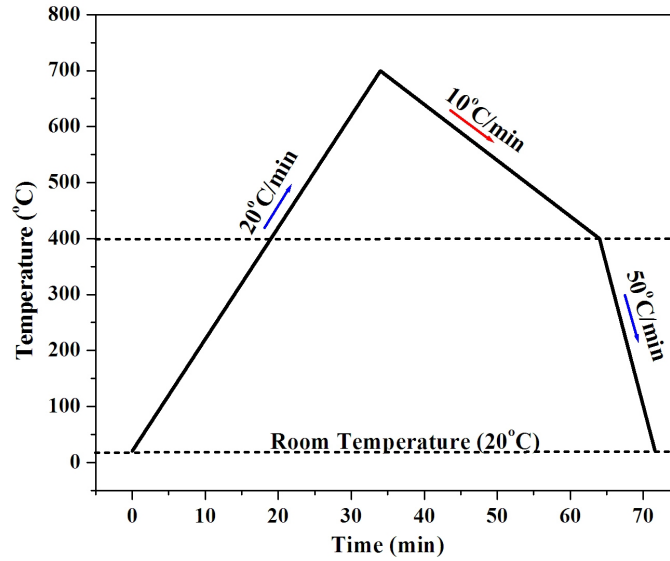
Figure 6.2: Typical thermal cycle for running solidification tests in DSC

records the change in temperature during heating and cooling as well as the change in temperature in a reference crucible in order to determine the amount of energy evolved of absorbed during the thermal cycling. This evolution of energy presents indications of phase changes and/or precipitation reactions and thus can provide knowledge of the solidification kinetics.

The specific testing procedure used for measuring the solidification kinetics of AA5182 was as follows. First, each sample was weighed and then placed into an alumina crucible within the sample carrier of the DSC. Second, the chamber was closed and then evacuated and purged with N_2 gas. This process of evacuation and purging was repeated 3 times to remove as much O_2 gas as possible. Third, the testing cycle was programmed into the software, requiring the operator to specify the evolution of temperature with time. The aluminum alloy in question, AA5182 has its solidus and liquidus between 500 and 700°C. Moreover, as the interest is in observing the solidification kinetics, only the cooling cycle is important and must be properly controlled properly. The samples were heated at a constant rate of 20°C/min to 700°C and the cooled to 400°C at different cooling rates. A typical thermal cycle applied to the equipment is shown in figure 6.2. To ensure that

the results were reproducible, at least 3 samples from each location were tested using this procedure. Moreover, samples from the same location were also tested at different cooling rates.

6.6 Summary

Microstructural features, chemical composition and the evolution in fraction solid of an alloy strongly influence the hot tearing phenomenon in casting. The experimental methodology for grain size measurements, chemical analysis and the determination of solidification kinetics of within an AA5182 have been described in this chapter. The experimental results for an as cast AA5182 ingot will be presented and analyzed critically in the following chapter.

Chapter 7

Microstructural Analysis of an AA5182 DC Cast Ingot - Results and Discussion

7.1   Introduction

In the previous chapter, the experimental methodology for analyzing the microstructural features of as-cast AA5182 (grain size, chemical composition, and solidification kinetics) was presented. In this chapter, the results from these experiments will be reported. The objective of this chapter is also to discuss and explain the results by comparing them with the theory and related work found in the literature. Finally, we relate the findings to the simulation results from chapter 5.

7.2   Grain Size Measurements

5 samples were analyzed, showing the variation in grain size from the centre of the ingot out towards the surface along the centerline of the rolling face. The quantitative measurements are shown in table 7.1, with the corresponding micrographs provided in figure 7.1. As can be seen, the grains are equiaxed dendritic throughout the cross-section, but the grain size does vary considerably. The grains are largest at the centre but gradually
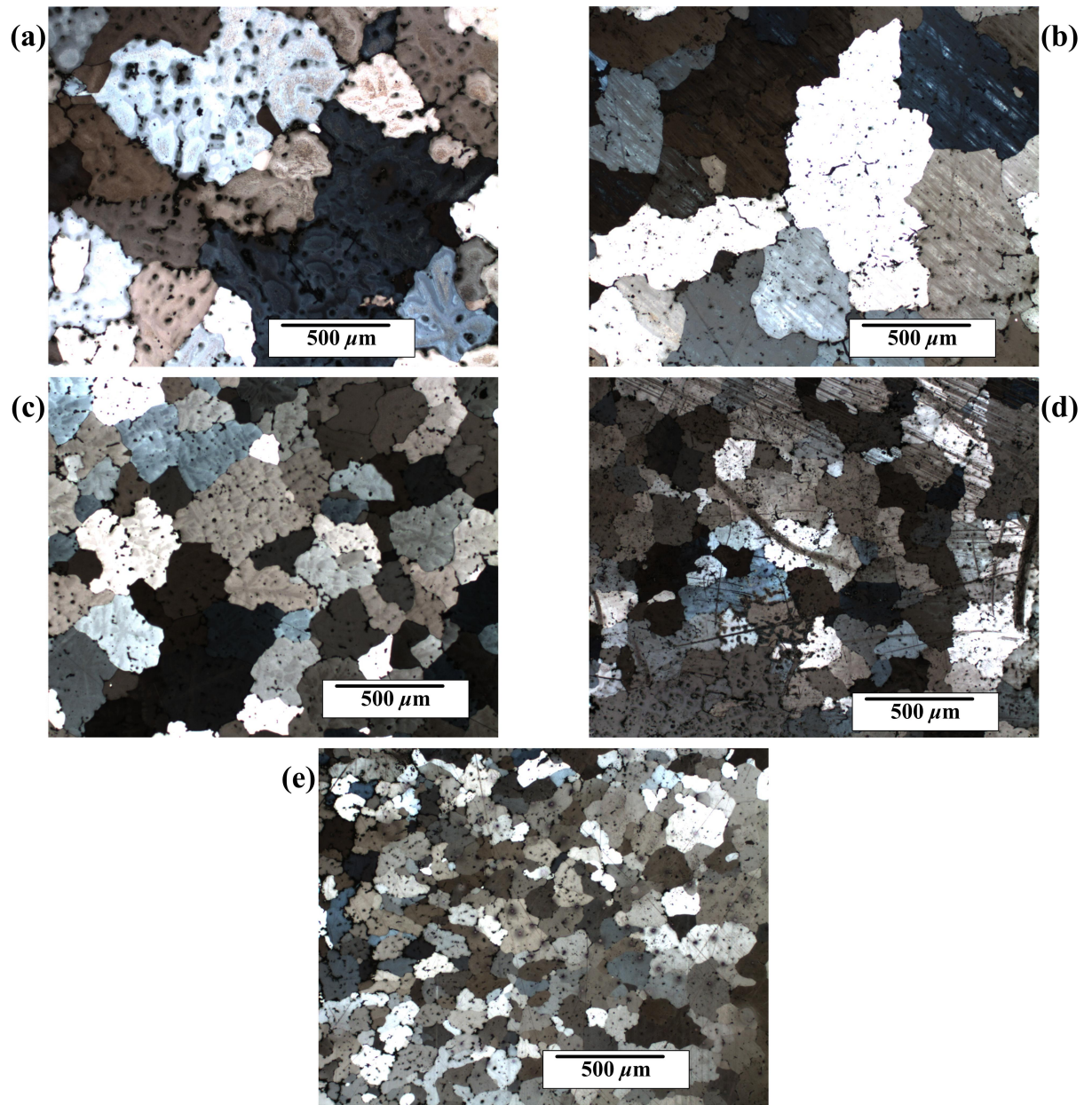
Figure 7.1: Optical micrographs of samples taken from (a) center (b) 62.5 mm from the center (c) 125 mm from the center (d) 187.5 mm from the center (e) at surface, at 50× magnification, viewed under cross-polarized light with sensitive tint attachment

Table 7.1: Average grain size ($\bar{d}$, measured by Jeffrie's Method) of samples taken at various distances from the center of the ingot

Distance from the centre (mm)	$\bar{d}$ (μm)	S.D.[a]
0.0 (centre)	514.30	30.84
62.5	394.16	27.09
125.0	257.24	28.98
187.5	257.03	35.14
250.0 (surface)	122.77	402.96

[a]Standard Deviation

decrease in size as the surface is approached. The qualitative observation made from the micrographs are evident in the measurements, i.e. the average grain size (514.30 μm) is more than 4 times larger than the value found at the surface (122 μm). The decrease in grain size from center to surface can be attributed to the variable cooling conditions experienced throughout the cross section of the ingot. At the surface, the rate of heat removal is high due to the primary (mould) interfacial cooling and secondary cooling by cooling water jets. This effect diminishes away from the surface, as the rate of heat removal is controlled rather by the rate of heat conduction through the casting body. This conduction rate is in turn controlled by the thermal conductivity (κ) through fully solid, fully liquid as well as through the semi-solid metal.

The results presented in table 7.1 and in figure 7.1 match well qualitatively with the microstructural studies made by various researchers on DC cast products (Erdegren et al. 2012, Nadella et al. 2008a, Suyitno 2005). Suyitno (2005), in his PhD work, observed microstructure of the DC cast billets and measured grain sizes for various compositions of Al-Cu alloys. Micrographs observed at the center of the billet in this work are similar to the ones shown in figure 7.1. In addition, grain size was reported to increase with increasing distance from the surface and with a decrease in Cu concentration. Nadella et al. (2008a) experimentally measured the grain size of DC cast Al-Mg billets from center to surface. It was found that grain size is maximum at the center of the billet.
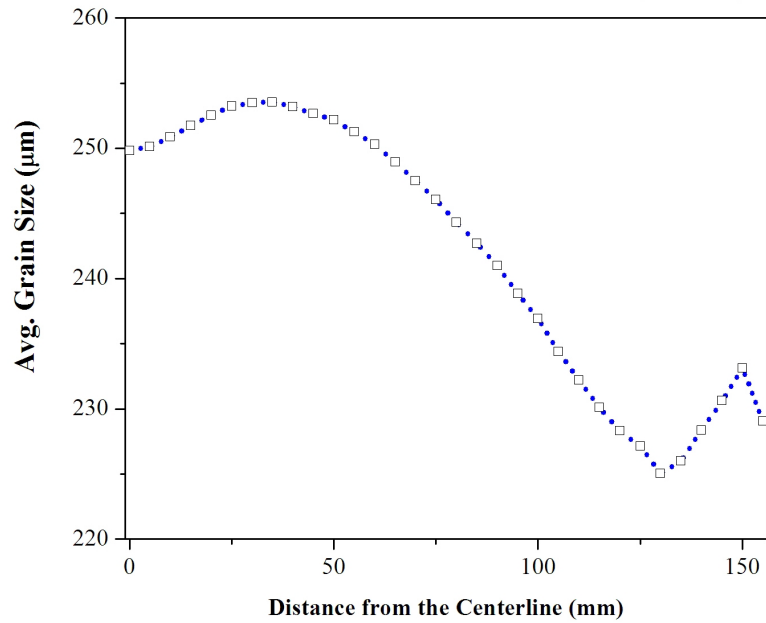
Figure 7.2: Variation of grain size as a function of distance center in a steady state region, obtained from simulation results of case *A*

Interestingly, grain size was found to be lowest in the sub surface region. Similar results were found by Nagaumi (2001) on a porosity and microstructure study of DC cast ingot of Al-4.4%Mg Alloy. Erdegren et al. (2012) arranged experiments in the laboratory to simulate the DC casting process in 6xxx series alloys. Measurements on the samples from these simulated experiments indicated that grain size increases monotonously from surface to center, which conforms well with our measurements.

Now, let us compare the microstructural measurements with the simulation results. For comparison, the base case (table 5.1) is selected where variation of grain size as a function of the cooling rate is incorporated. The grain size predictions from this simulation are shown in figure 7.2. In this figure, horizontal variation of grain size at different distances from the centre of the billet is shown. The horizontal line along which the grain sizes were extracted was at the steady stage region at 400 mm height from the bottom block, to match the fact that the experimental samples also came from the steady state region. The figure shows that the grain size generally decreases from the center to the surface. This is in agreement with the grain size measurements reported in this chap-

ter. Discrepancies between the simulation and the experimental measurements are most prominent in terms of the location of the maximum and minimum grain sizes. In the simulation, the maximum and minimum grain sizes occur in the area adjacent to the center and in the subsurface region, respectively. Conversely, the measured grain sizes show the maxima and minima at the centre and the surface, respectively. For the grain size measurements, distance between two samples was 62.5 mm. On the other hand, the simulated grain size predictions show minimum grain size at about 50 mm inside the surface. The lack of resolution in the variation of grain size (between 250 and 187.5 mm distance from the center) could be the reason why the minimum grain size is not shown experimentally at the subsurface region. Interestingly, the simulation results agree well with the experimental results found by Nagaumi (2001) and Nadella et al. (2008a) in terms of the location of maximum and minimum grain size. In addition, there is a size difference between the simulation billet (radius = 160 mm) and the ingot used for these experimental measurements (center to surface distance of 250 mm). The larger center to surface distance in the ingot should have important implications in terms of heat transfer from center to surface during the casting. As heat is only extracted from the surface during casting in the steady state region, a larger distance from the center to surface means heat has to travel a much longer path from center to dissipate into the surface. As the heat transfer is limited by the thermal conductivity of the alloy (same for both ingot and billet), the cooling rate at the centre of the ingot should be much lower for the ingot as compared to the billet during casting. The lower cooling rate at the centre may increase the grain size in this region. This is evident in the results, i.e. very large grains (514 μm) are seen experimentally at the centre of the ingot as opposed to that predicted by the simulation of the billet (260 μm). The smaller radius of the billet has resulted in a smaller grain size throughout the cross section compared to those of the ingot except at the surface. Furthermore, it seems that the range of grain size in the billet (400 μm) is about ten times larger than that of the ingot (40 μm). This variation in the range of grain size could be due to two reasons. First, it be attributed the the size

Table 7.2: Average compositions of major alloying elements in AA5182 with respect to distance from the center

Distance from the centre (mm)	Alloying Element (Weight %)		
	Mg	Mn	Cr
0 (centre)	3.445	0.368	0.191
62.5	3.998	0.399	0.178
125.0	4.009	0.396	0.181
187.5	4.113	0.385	0.178
250.0 (surface)	4.032	0.377	0.171

difference between the ingot and the billet and the resulting change of the heat transfer phenomenon. Second, it could be due to the effect of grain refinement. As the ingot has been heavily grain refined during casting, the high cooling rates at the surface activate a huge number of heterogeneous nucleating cites created by the grain refiners and result in smaller grain size at the surface (122 μm). The simulation of the billet does not account for any heterogeneous nucleation, and thus have a relatively large grain size at the surface (225 μm), and a small difference between the grain size at the centre and the surface.

7.3 Chemical Analysis

A compositional analysis of each of the experimental samples was carried out via SEM - EDS. The major alloying elements of AA5182 are Mg and Mn. Additionally, small amount of Cr (around 0.20%) was reported in the chemical analysis. The summary of chemical analysis from the center to the surface is shown in table 7.2.

The chemical analysis of samples taken from surface to center of the ingot revealed that there is significant macrosegregation. The macrosegregation of an alloying element in a particular location can be expressed as deviation from the nominal (average) composition (Nadella et al. 2008b), as shown in equation 7.1.

$$Deviation\ from\ the\ Nominal\ Composition\ =\ \frac{[X] - [X]_{nominal}}{[X]_{nominal}} \qquad (7.1)$$

where $[X]$ is the composition of element X and $[X]_{nominal}$ is the nominal composition of
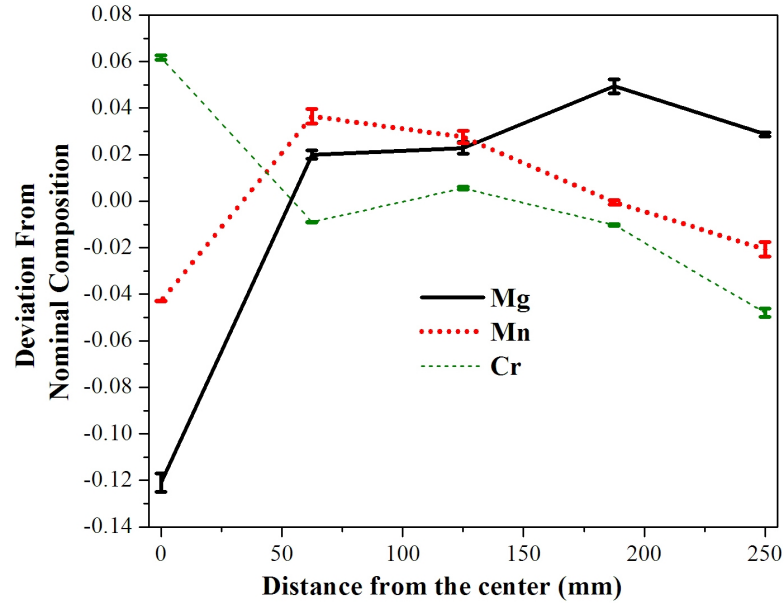
Figure 7.3: Distribution of relative concentration of different alloying elements as a function of distance from the centre

element X in the ingot. Using the data in table 7.2, the graphs in figure 7.3 are obtained, which show deviation from nominal composition of each alloying element at different distances from the centre. Values greater than zero of this deviation indicates 'positive' macrosegregation. Conversely, values less than zero indicate 'negative' macrosegregation.

As can be seen from figure 7.3, Mg has considerable negative macrosegregation at the centre of the ingot typically found in DC cast billets and ingots (Erdegren et al. 2012, Eskin et al. 2004). The centerline segregation can be explained by a phenomenon called the floating or showering crystals (Nadella et al. 2008b). Small particles of lower solute concentration detach from the first solidified shell and settle down at the centre causing this centreline macrosegregation . The particles settle since they have a higher density due to the lower Mg content and fall towards the base of the sump.

In addition, there is also positive segregation of Mg close to the the chill surface. This phenomenon is most likely due to the presence of liquid richer in solute within the

interdendritic channels close to the surface during solidification (Erdegren et al. 2012). Due to solidification shrinkage, liquid of higher concentration away from the surface is sucked back into these channels and this liquid solidifies with higher concentration of Mg. This results in a positive segregation of Mg at and close to the chill surface of the ingot.

Mn shows negative segregation at the centerline, which could also be explained the theory of floating crystals. Furthermore, positive segregation of Mn between the center and the surface is also reported similar to Mg. But, unlike Mg, Mn has negative segregation at the surface of the ingot, which is in contrary to the studies made by Eskin et al. (2004), Nadella et al. (2008b). One interesting work, which is on the contrary to our findings was done by Dons et al. (1999). In this work on DC cast Al-Si alloys showed that Mn somehow resists macrosegregation. Finally, the third element, Cr, shows a positive segregation at the centre, no segregation at the middle and negative segregation at the surface of the ingot. Positive segregation of Cr could be due to the accumulation of intermetallic compounds containing Cr at the center of the ingot, and a consequent depletion of Cr rich particles from the surface.

The process model for DC casting billet described in chapter 4 is a thermomechanical model, and does not take macrosegregation of the ingot into account. Thus, it is not possible to compare the macrosegregation results with the model predictions.

7.4   Solidification Kinetics

Solidification tests with the samples of alloy AA5182 were carried out in a differential scanning calorimeter (DSC). The output from DSC gives a curve of change in energy (amount of energy absorbed/ evolved) during heating/cooling as a function of temperature. These curves were analyzed in the software 'NETZCH Proteus', version 5 (companion to the NETZCH DTA unit). The region of interest of the solidification curves is between the solidus and liquidus temperatures. From a typical curve given by the DSC,
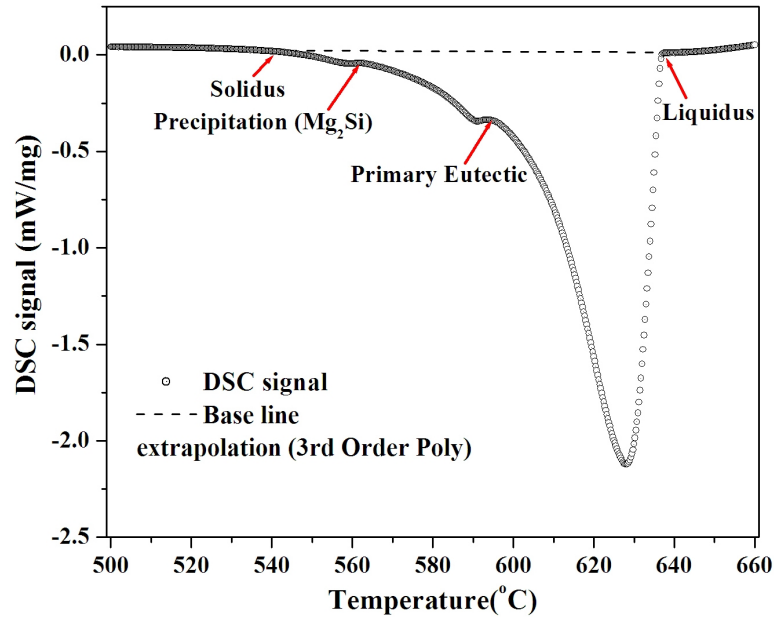
Figure 7.4: Solidification curve of a sample of AA5182 from the DC cast ingot piece, cooling rate = 10^oC/min

the liquidus and the solidification reactions are easily identifiable as sharp extremities in this curve. The alloy being investigated (AA5182) goes through the following reactions during solidification (Bäckerud et al. 1990):

- Start of solidification and formation of α-Al (T_{liq})

- R1 : Start of eutectic reaction : Liq $\rightarrow$ α-Al + Al$_6$(FeMn)

- R2 : Precipitation of Mg$_2$Si : Liq $\rightarrow$ Al + Mg$_2$Si

- R3 : Complex eutectic precipitation : Liq $\rightarrow$ Al + Al$_3$Fe + Mg$_2$Si + Al$_8$Mg$_5$

- End of solidification (T$_{sol}$)

A typical solidification curve for an ingot sample obtained from DSC is shown in figure 7.4. Note that the DTA signal is negative when there is an exothermic reaction (energy is released). Because the solidification phenomenon is an exothermic reaction, so the curve takes a downward path. The spikes in the curve are indicative of different solidification/precipitation reactions occurring at particular temperatures. Comparing

96
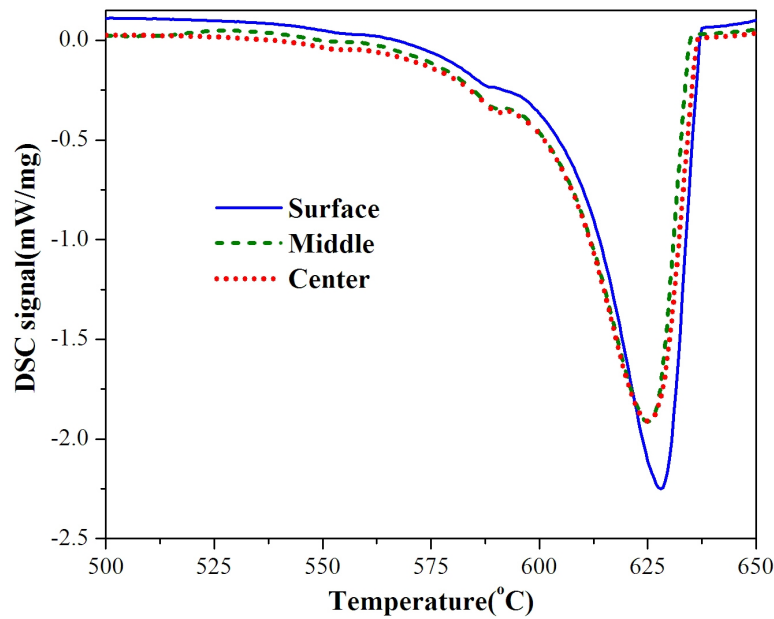
Figure 7.5: DSC curves of samples samples of as cast AA5182 taken from different locations of the ingot, cooling rate = 10^oC/min

the sequence of reactions mentioned above with the extremities observed in this curve, the liquidus point, the eutectic point and the point of Mg$_2$Si precipitation can be easily identified as shown in the figure. But the solidus can not be identified easily. To estimate the solidus point, a third order polynomial baseline was drawn with the points well above the liquidus point and well below the solidus point from the curve. The intersection point of this baseline with this curve is a good estimate of the solidus point (Bäckerud and Tamminen 1986), as shown in the figure.

7.4.1   Effect of Location

From the ingot described in chapter 6, 5 samples were taken between the centerline and the chill-surface for this study. DSC solidification tests were then run with these samples. Some of the results from these tests are summarized in figure 7.5. It is clear from the figure that the solidification behavior of the samples of the three positions : center, middle and the surface are different. There is a slight variation in liquidus, eutectic and precipitation reaction points due to variation in position. As the distance from the surface increases, all these points shift to lower temperatures, although there is virtually no difference of
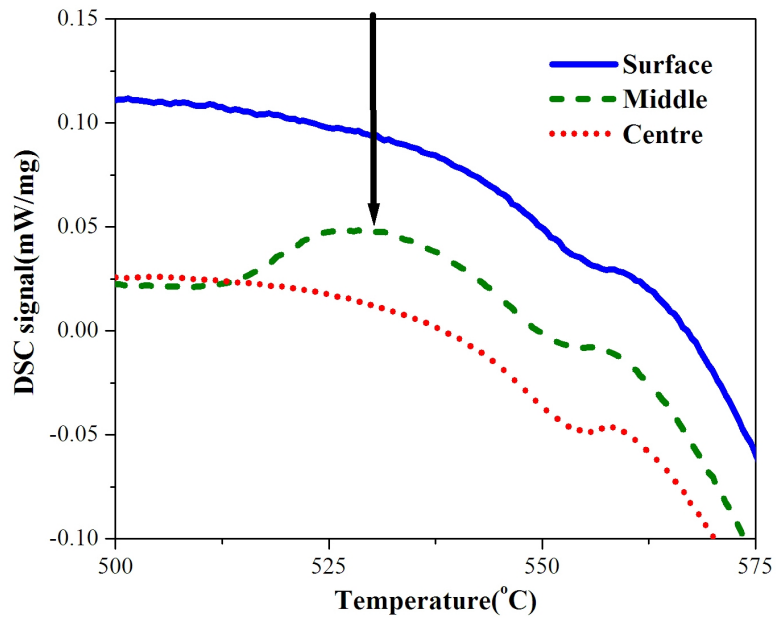
Figure 7.6: DSC curves of samples samples of as cast AA5182 taken from different locations of the ingot in the range of 500 to 575°C, cooling rate $= 10^o$C/min
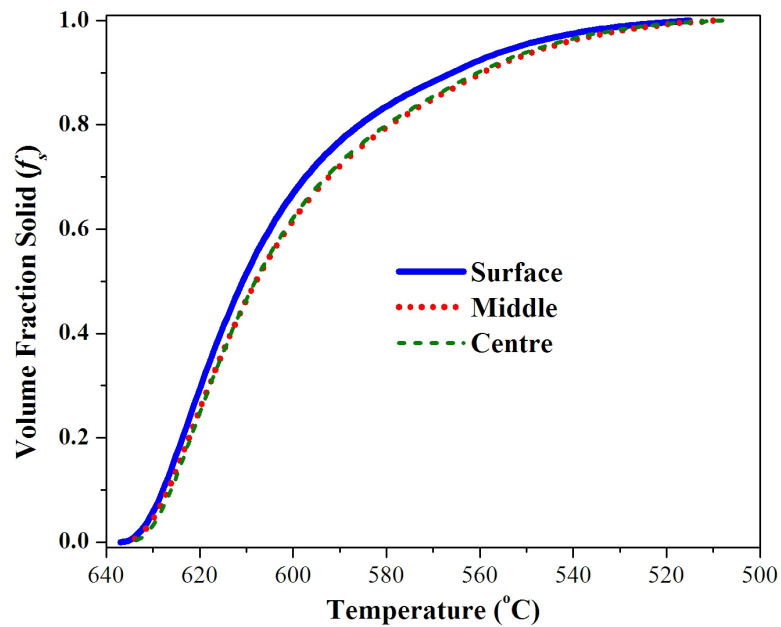
**Figure 7.7:** Solidification path of samples of as cast AA5182 taken from different locations of the ingot, cooling rate $= 10^o$C/min

Table 7.3: Comparison of averaged solidus, luquidus, and solidification reaction temperatures of as cast AA5182, experimental values correspond to a cooling rate of 10°C/min (L = Liquidus, S = Solidus, the standard deviation for each data point is shown in the parenthesis)

Source	L (^{o}C)	R1 (^{o}C)	R2 (^{o}C)	R3 (^{o}C)	S (^{o}C)
Exp. (Surface)	636.67(0.57)	N/A	591.17 (0.76)	557.67 (1.53)	514.67 (1.52)
Exp. (Middle)	636.33 (1.52)	N/A	591.25 (1.5)	561.33 (1.4)	509.90 (2.09)
Exp. (Centre)	634.87 (1.57)	N/A	592.10 (2.32)	564.5 (1)	508.33 (1.42)
Ref.1[a]	637	623	582	560	536
Ref.2[b]	632	621	586	557	470
Ref.3[c]	624	N/A	587	557	508

[a]Arnberg et al. (1996),Cooling rate = 18 K/min
[b]Bäckerud et al. (1990), Cooling rate = 18 K/min
[c]Thompson et al. (2004), Cooling rate = 30 K/min

the solidification curves for the 'middle' and the 'center' samples. The liquidus, solidus, the solidification reactions (R1, R2, R3) along with their range of variation within the same location are listed in table 7.3. This table also include the literature values of these points from different sources for the sake of comparison. As can be seen from the table, the points are reproducible, with the maximum standard deviation of 2.32. However, the R1 reaction could not be identified in the solidification curves obtained from DSC. The liqudus and the R2 point seem to be relatively invariant of the position. But R3 and solidus points vary with position. R3 temperature increases slightly from surface to center, and solidus point decreases considerably from as the distance from surface increases. The decrease in solidus temperature could be due to high negative macrosegregation of Mg and Mn in the center, and positive segregation of Mg at the surface. The change in solidus temperature with respect to position could have important influence on the formation of hot tears in DC casting, since it is believed that hot tears form in the last stage of solidification at temperatures close to solidus.

Moreover, there is a slight bump in the curve for the 'middle' sample at around 530°C, which is reproducible, and absent in samples from center/surface. This is not clear from figure 7.5, so the DSC curves for a narrower range is shown in figure 7.6, and the arrow in
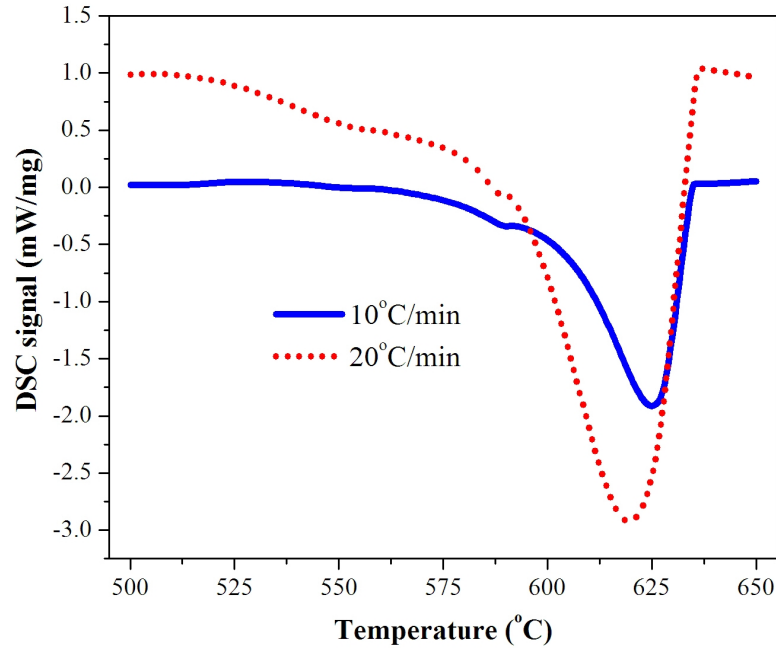
Figure 7.8: DSC curves of samples of as cast AA5182 taken from same location of the ingot tested at 2 cooling rates, 10 and 20°C/min.

this figure indicates the bump. This bump occurs at the last stage of solidification, and could have some influence on hot tear formation. Another noticeable difference among these curves is the area under the curve. This area under the curve is very important, since it is related to the evolution of fraction solid with temperature. Volume fraction solid vs temperature curves have been extracted from these solidification kinetics curves, as shown in figure 7.7. There is a clear difference in evolution of fraction solid at different distances from the center. The solidification path of the sample taken from center and the middle are almost identical, owning to similar solidification curves, while that of the sample at the surface is quite different.

7.4.2 Effect of Cooling Rate

Samples taken from the same location of the ingot were subjected to different cooling rates. The solidification curves for different cooling rates of samples taken from the same location showed interesting variations. An example is shown in figure 7.8. The liquidus, solidus, and reaction temperatures for these two cooling rates have been summarized in

100
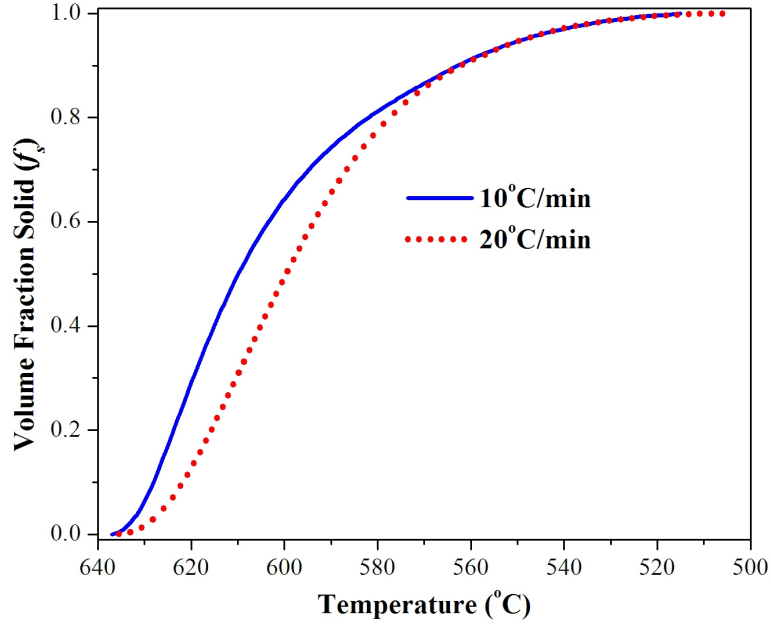
Figure 7.9: Solidification path of samples of as cast AA5182 taken from same location of the ingot tested at 2 cooling rates, 10 and 20°C/min

Table 7.4: Comparison of solidus, liquidus, and solidification reaction temperatures of as cast AA5182 between literature and experimental values in terms of cooling rate. (CR = Cooling Rate, L = Liquidus, S = Solidus, Ref.1=Bäckerud et al. (1990))

Source	CR (K/min)	L (^oC)	R2 (^oC)	R3 (^oC)	S (^oC)
Exp.	10	636.67 (0.57)	591.17 (0.76)	557.67 (1.53)	514.67 (1.52)
Exp.	20	637.17 (1.05)	590.33 (1.53)	556 (0.5)	504.83 (1.04)
Ref.1	18	632	586	557	470
Ref.1	54	632	584-581	556	470

table 7.4. This table also includes the temperature of each of these points found in the literature for 2 different cooling rates. First, the liquidus points occur almost at the same temperature for both cooling rates, but the reaction and solidus temperatures are shifted towards towards lower temperatures for a higher (20°C/min) cooling rate. This phenomenon can be explained by the well known theory that the phase diagram becomes depressed in terms of temperature at higher cooling rates, resulting in lowering of solidus, and other reaction temperatures. Comparing the the variation in solidus and liquidus temperatures from the experiments with the literature value (Bäckerud et al. 1990), we

can see that literature values of these temperatures are virtually invariant of cooling rate, while our experimental values show significant variations. This could be due to the fact that the literature values presented in the table deal with high cooling rates while the experiments conducted here deal with relatively low cooling rates. At these high values of cooling rates, the reaction temperatures may become insensitive to cooling rates, while at low temperature they may still be sensitive to cooling rate variation. Another main difference between the DSC curves in figure 7.8 is in the amount of energy released during solidification (i.e. area under the curve). Consequently, the solidification path for these two samples become very different, as shown in figure 7.9. This will have important implications for hot tearing.

7.5 Summary

The experimental results of grain size measurements, chemical analysis and solidification kinetics of as cast AA5182 have been reported. The grain size is found to increase substantially from surface to centre of the ingot. The grain size measurements are also compared with simulation results. There is qualitative agreement between trends in the variation between the predicted and measured grain size from centre to surface. The chemical analysis shows that there is substantial macrosegregation of Mg, Mn and Cr from centre to surface. Mg shows negative segregation at the centre and positive segregation at the surface. Mn shows negative segregation both at centre and surface, and positive segregation elsewhere. Cr shows segregation trends exactly opposite to Mg. Solidification kinetics experiments revealed that both location of the sample and cooling rate influence the liquidus, solidus, reaction temperatures, as well as the evolution in fraction solid of as cast AA5182. Solidus temperature of as cast AA5182 decreases (1) with increasing cooling rates for samples from the same location; and (2) with the increase in distance from the surface of the ingot for samples from different location. The macrosegregation phenomenon seen here should influence the semi-solid strength, because the strength of the solid network should vary with composition. This could alter the hot tearing behavior

of an alloy as a function of position. Moreover, the difference in solidification kinetics at different positions of the ingot influences the evolution in fraction solid as a function of temperature. This means that the critical points such as the solidus, liquidus and the coalescence temperature vary as a function of cooling rate and position. These may also alter the mechanical behaviour of the mush, and consequently can revise the hot tearing susceptibility.

Chapter 8

Conclusion and Perspectives

8.1 Conclusion

Hot tearing is known to occur in mushy alloys under strain, when the network of solid grains is not fully percolated and feeding by the intergranular liquid is difficult. Even though the general context for the formation of this defect is known, quantitative theories are difficult to formulate and their predictive capability remains limited. The problem of hot tearing is very complex because numerous physical phenomena come into play and interact with each other. Moreover, the properties of the mushy alloys are difficult to measure and model accurately. In addition to this, the geometry of the casting and boundary conditions that it experiences may become quite complicated to describe. For all of these reasons, assessing the problem at hand is only possible provided efficient numerical modeling tools are available.

Semi-continuous direct-chill (DC) casting of aluminium alloys suffers frequently from the hot tearing defect. This phenomenon takes place in the mushy state (i.e., at solid fractions, gs, lower than unity). In order to solve this problem, research moved towards the development of models for the prediction of the hot cracking sensitivity of any kind of alloy under given casting conditions. The current project involves the study of hot tearing during direct-chill (DC) casting of aluminum alloy AA5182 with respect to mi-

crostructural features and casting parameters. Hot tears are believed to occur in the semi-solid at high fraction solids during solidification. So, for a thermomechanical process model of DC casting to have predictive capabilities in terms of hot tear formation, it is very important to incorporate a robust description of semi-solid behaviour of the alloy. In this work, a previously developed axisymmetric DC casting thermomechancial model for round billets was improved by incorporating a semi-solid constitutive law for AA5182 which includes the microstructural features of the semi-solid body. Now-a-days, the DC cast alloys are heavily grain refined, and thus only the cooling rate has a bearing on determination of grain size within the casting. The process model for this project also includes the variation of grain size throughout the casting due to differential cooling conditions experienced by the casting body. The underlying assumptions and simplifications of the model are listed below:

- The model only considers nucleate boiling heat transfer regime of secondary cooling by the spray water jet. It does not take into account the film boiling regime of the cooling, where the heat transfer coefficient drops drastically.

- A fixed heat transfer rate at the billet-bottom block interface was assumed in the model.

- Fluid flow is ignored in this model. To account for the increased heat transfer by convection in the liquid, the effective thermal conductivity is increased artificially in the semi-solid and liquid state.

- A low constant yield stress is assumed above coalescence temperature to avoid false strain accumulation in the slurry.

- For the variable grain size case, the grain size is only a function of the average cooling rate between the liquidus and the coalescence temperature. Other factors of grain refinement are ignored.

- An invariant solidification path is used for the model.

- The effects of macrosegregation are ignored.

Using this DC casting process model, numerous simulations were run varying microstructural features and process parameters. A relative hot tearing criterion called the 'hot tearing strain' was proposed, which was calculated using the stress-strain predictions from the model. For observing the effect of grain size, coalescence temperature, and casting speed, 5 different scenarios (see table 5.1) were selected. The temperature, stress and strain fields along with the hot tearing strain were prepared along both horizontal direction (at various billet heights) and vertical direction (along the centreline).

Through the temperature fields in the vertical direction along the centreline and the surface, steady state and start up regions were identified. Along the centreline, the steady state was achieved at 400 mm from the bottom block, while at the surface it was at around 100 mm of casting. The steady state was also demonstrated mechanically, through the observation of variation of hoop-stress at $f_s = 0.98$ along the centreline. Note that, as with the temperature field, the hoop stress field also becomes invariant of location in the steady state region. The variation of hot tearing strain along the horizontal and vertical directions revealed that for round billets, hot tears are most likely to occur close to the centreline and and to the bottom block in the start up stage of the DC casting process. In addition, the area close to the surface and the bottom block is also found to be susceptible to hot tearing, but to a lesser extent compared to the area close to the centreline. Once the startup state is over, the hot tearing susceptibility diminishes into the steady state region.

When the relative hot tearing susceptibility for various grain sizes, coalescence temperatures and casting speeds were compared, the following conclusions could be made:

1. Hot tearing susceptibility is shown to vary with grain size. The hot tearing susceptibility generally decreases with decreasing grain size, owing to the higher strength of the casting body in the semi-solid region for smaller grains. The lowest hot tearing susceptibility is shown for the variable grain size simulation (Case A). But, when

the lowest grain size is approached (75 μm), the hot tearing susceptibility actually increases.

2. The hot tearing susceptibility is very sensitive to casting speed. Decreasing casting speed decreases the hot tearing susceptibility, provided that the secondary cooling by water jet remains in the nucleate boiling regime. If the heat transfer mode shifts to the film boiling region, the heat transfer coefficient is drastically reduced and severe hot tears may form.

3. The choice of mechanical coalescence temperature is a critical factor when assessing hot tearing susceptibility. For a lower assumed coalescence temperature, the hot tearing susceptibility is drastically increased , and vice versa. Thus, for a good semi-solid stress-strain predictions, it is critical to choose the appropriate coalescence temperature.

In addition to simulating the DC casting process, grain size measurements, chemical analysis, and DSC experiments were carried out on the samples collected from an as cast (DC cast) ingot of AA5182. The grain size measurements from the samples taken along the centerline of the rolling face indicated that the grain size decreases steadily from centre to surface, owing to the different cooling conditions experienced across the cross-section of the ingot. The chemical analysis of the samples revealed that there is considerable macrosegregation of Mg and Mn from center to surface of the ingot. The DSC solidification kinetics experiments on the smaples of as cast AA5182 demonstrated that the solidus, liquidus and the reaction temperatures vary both as a function of the cooling rate and distance from the centre of the ingot.

By comparing the experimental results from the as cast AA5182 with the predictions and underlying assumptions of the simulation, the following conclusions could be made :

1. The measured grain size from as cast AA5182 and the predicted grain size from the simulation of round billets agree qualitatively. The larger size of the ingot (250

mm) as compared to the billet (radius = 160 mm), induced larger grain sizes and and higher variation of grain size across the grain sizes. This comparison validates, at least qualitatively the assumption of variation of grain sizes based on the cooling rate in the semi-solid region.

2. There is a considerable amount of macrosegregation of alloying elements along the cross section of the casting. The model does not account for the this macrosegregation. The amount of alloying elements locally determine the semi-solid strength. Thus, if macrosegregation is present in the casting, the strength in the semi-solid region would vary as a function of position. This could alter the hot tearing susceptibility of the cast structure.

3. The solidification kinetics tests of the samples reveals that there is considerable difference in solidus, liquidus and solidification reaction temperatures within the ingot as a function of both the location and the cooling rate. Although the process model includes cooling rate induced variation of grain size, it assumes the solidification path (f_s vs. Temp) to be invariant of the cooling rate and also composition (i.e. location). The evolution in fraction solid is one of the most important factors in determining the semi-solid mechanical behaviour and thus most of the constitutive laws include the fraction solid (f_s) term. The temperatures at which solidus and liquidus occur are factors in determining the semi-solid mechanical behaviour, as it is a strong function of temperature. Therefore, any variation in the solidification path, and the liquidus and solidus temperatures will strongly influence the strength of the semi-solid mush and thus have important implications on the hot tearing susceptibility.

8.2 Perspectives

From the above discussion, it is clear that the process model is capable of capturing some aspects of solidification (such as grain size variation). The model is also able to predict

hot tearing susceptibility in DC casting in terms of microstructural features and casting parameters with relative accuracy. Having said that, the model is rather simplistic is some aspects, ignoring factors that effect the semi-solid mechanical behaviour such as macrosegregation and the variation in solidification kinetics. Another drawback of this model is that it does not account for the film boing regime of heat transfer during cooling by water jets. Thus, for this model to be more accurate, the following modifications could be applied to the model:

1. A macrosegregation model could be included into the model to account for the variation in alloy properties with composition.

2. A more accurate model for variable grain size could be included.

3. A set of solidification paths for the alloy which include the effects of grain size, chemical composition and cooling rate effects could be incorporated.

References

Alankar, A. and Wells, M.A. 2010. Constitutive behavior of as-cast aluminum alloys AA3104, AA5182 and AA6111 at below solidus temperatures. Materials Science and Engineering A-Structural Materials Properties Microstructure and Processing, **527** (29-30):7812–7820.

Arnberg, L., Bäckerud, L., and Chai, G. 1996. Solidification Characteristics of Aluminum Alloys, Volume 3 : Dendrite Coherency. Number v. 3 in Solidification Characteristics of Aluminum Alloys, AFS/Skanaluminium.

Bäckerud, G.C. and Tamminen, J. 1986. Solidification characteristics of aluminium alloys. Solidification characteristics of alumnium alloys, AFS/Skanaluminium.

Bäckerud, L., Chai, G., and Tamminen, J. 1990. Solidification Characteristics of Aluminum Alloys. Number v. 2 in Solidification Characteristics of Aluminum Alloys, AFS/Skanaluminium.

Backuerud, L., Chai, G., and Tamminen, J. 1990. Solidification Characteristics of Aluminum Alloys,Volume 2:Foundry Alloys. 3rd edition, AFS Skanaluminium, Stockholm,Sweden.

Bagnoud, C. and Plata, M. 2000. Coupled 2-D fluid flow -thermal-structural numerical simulation of the direct-chill ingot casting process. Modeling of Casting, Welding and Advanced Solidification Processes IX, Aachen, Germany, 753–760.

Benum, S., Mortensen, D., Fjaer, H., Overlie, H., and Reiso, O. 2002. On the mechanism of surface cracking in DC cast 7xxx and 6xxx extrusion ingot alloys. Light Metals 2002:967–974.

Boender, W., Burghardt, A., van Klaveren, E.P., and Radenberg, J. 2004. Numerical Simulation of DC casting; Interpreting the results of a thermo-mechanical model. Light Metals - Warrendale - Proceedings, **39**:679–684.

Braccini, M., Martin, C., Suery, M., and Brchet, Y. 2000. Relation between mushy zone rheology and hot tearing phenomena in Al-Cu alloys. Modeling of Casting, Welding, and Advanced Solidification Processes IX, Shaker Verlag, GmbH, Aachen, Germany, 18–24.

Campbell, J. 1991. Castings. 2nd edition, Butterworth-Heinemann.

Caron, E. and Wells, M. 2006. Effect of advanced cooling front (ACF) phenomena on film boiling and transition boiling regimes in the secondary cooling zone during the direct-chill casting of aluminum alloys. Materials Science Forum.

Chai, G.C., Backerud, L., Rolland, T., and Arnberg, L. 1995. Dendrite Coherency during Equiaxed Solidification in Binary Aluminum-Alloys. Metallurgical and Materials Transactions A-Physical Metallurgy and Materials Science, **26** (4):965–970.

Chang, Y., Yan, X., Xie, F., and Chen, S. 2004. Phase formation and solidification path analysis of multicomponent aluminum alloys. Minerals, Metals and Materials Society, 184 Thorn Hill Rd, Warrendale, PA 15086-7514, USA, 18.

Clyne, T. and Davies, G. 1981. The influence of composition on solidification cracky susceptibility in binary alloy systems. The british foundryman:65–73.

Colley, L., Wells, M., and Maijer, D. 2004. Tensile properties of as-cast aluminum alloy AA5182 close to the solidus temperature. Materials Science and Engineering A-Structural Materials Properties Microstructure and Processing, **386** (1-2):140–148.

Collier, J.G. and Thome, J. 1994. Convective boiling and condensation. 3rd edition, Oxford University Press, Walton Street, Oxford OX26DP, England.

Commet, B., Delaire, P., Rabenberg, J., and Storm, J. 2003. Measurement of the onset of hot cracking in DC cast billets. Light Metals 2003:711–717.

Dobrzanski, L.A., Maniara, R., Sokolowski, J., and Kasprzak, W. 2007. Effect of cooling rate on the solidification behavior of AC AlSi7Cu2 alloy. Journal of Materials Processing Technology, **191** (1-3):317–320.

Dons, A., Pedersen, L., and Arnberg, L. 1999. The origin of 'anomalous' microsegregation in Al-Si foundry alloys - modelling and experimental verification. Materials Science and Engineering A-Structural Materials Properties Microstructure and Processing, **271** (1-2):91–94.

Drezet, J. and Eggeler, G. 1994. High Apparent Creep Activation-Energies in Mushy Zone Microstructures. Scripta Metallurgica Et Materialia, **31** (6):757–762.

Drezet, J. and Phillion, A.B. 2010. As-Cast Residual Stresses in an Aluminum Alloy AA6063 Billet: Neutron Diffraction Measurements and Finite Element Modeling. Metallurgical and Materials Transactions A-Physical Metallurgy and Materials Science, **41A** (13):3396–3404.

Drezet, J. and Rappaz, M. 1996a. Modeling of ingot distortions during direct chill casting of aluminum alloys. Metallurgical and Materials Transactions A-Physical Metallurgy and Materials Science, **27** (10):3214–3225.

Drezet, J. and Rappaz, M. 2001. Prediction of hot tears in DC-cast aluminum billets. Light Metals 2001:887–893.

Drezet, J., Rappaz, M., and Krahenbuhl, Y. 1996a. Modelling of thermomechanical effects during direct chill casting of AA1201 aluminium alloy. Aluminium Alloys: their Physical and Mechanical Properties, Pts 1-3, **217**:305–310.

Drezet, J., Rappaz, M., and Krahenbuhl, Y. 1996b. Modelling of thermomechanical effects during direct chill casting of AA1201 aluminium alloy. Aluminium Alloys: their Physical and Mechanical Properties, Pts 1-3, **217**:305–310.

Drezet, J., Burghardt, A., Fjaer, H.G., and Magnin, B. 2000a. Thermomechanical effects in DC casting of aluminium alloy: a numerical benchmark study. Solidification and Gravity 2000, **329-3**:493–499.

Drezet, J., Rappaz, M., Grun, G., and Gremaud, M. 2000b. Determination of thermophysical properties and boundary conditions of direct chill-cast aluminum alloys using inverse methods. Metallurgical and Materials Transactions A-Physical Metallurgy and Materials Science, **31** (6):1627–1634.

Drezet, J.M. and Rappaz, M. 1996b. Ingot Distortions and Residual Stresses in Direct Chill Casting of Aluminium Alloys. Proceedings of the 4th European Conference on Residual Stresses,Cluny,France, Société Française de Métallurgie et des Métaux, 357–366.

Drezet, J.M., Rappaz, M., Carrupt, B., and Plata, M. 1995. Experimental Investigation of Thermomechanical Effects during Direct Chill and Electromagnetic Casting of Aluminum-Alloys. Metallurgical and Materials Transactions B-Process Metallurgy and Materials Processing Science, **26** (4):821–829.

Droste, W.E., Grun, G.U., Schneider, W., and Drezet, J.M. 2002. Thermo-mechanical modeling to predict shrinkage, shape and mold openings for DC-cast rolling ingots. Light Metals 2002:703–708.

EAA 2005. Market report. European Aluminum Association.

Easton, M., Wang, H., Grandfield, J., StJohn, D.H., and Sweet, E. 2004. An analysis of the effect of grain refinement on the hot tearing of aluminium alloys. Materials Forum, **28**:224–229.

Easton, M., StJohn, D., and Sweet, L. 2010. Grain Refinement and Hot Tearing of Aluminium Alloys - How to Optimise and Minimise. Aluminium Cast House Technology Xi, **630**:213–221.

Easton, M.A. and StJohn, D.H. 2001. The effect of alloy content on the grain refinement of aluminium alloys. Light Metals 2001:927–933.

Emley, E. 1976. Continuous Casting of Aluminum. International Metals Reviews, **21**:75 – 115.

Erdegren, M., Ullah, M.W., and Carlberg, T. 2012. Simulation of surface solidification in direct-chill 6xxx aluminum billets. 3rd International Conference on Advances in Solidification Processes, **27**:012013.

Eskin, D., Suyitno, and Katgerman, L. 2004. Mechanical Properties in the Semi-Solid Sate and Hot Tearing of Aluminum Alloys. Progress in Materials Science, **49**:629–711.

Eskin, D.G. and Katgerman, L. 2009. Solidification phenomena related to direct chill casting of aluminium alloys: fundamental studies and future challenges. Materials Technology, **24** (3):152–156.

Eskin, D.G., Du, Q., and Katgerman, L. 2008. Scale rules for macrosegregation during direct-chill casting of aluminum alloys. Metallurgical and Materials Transactions A-Physical Metallurgy and Materials Science, **39A** (5):1206–1212.

Farup, I. and Mo, A. 2000. The effect of work hardening on thermally induced deformations in aluminium DC casting. Journal of Thermal Stresses, **23** (1):71–89.

Feurer, U. 1976. Methematisches Moedell der Warmribneigung von binaren Aluminiumlegierungen Giesserei-Forschurng:75–80.

Fjaer, H. and Mo, A. 1990. Alspen-a Mathematical-Model for Thermal-Stresses in Direct Chill Casting of Aluminum Billets. Metallurgical Transactions B-Process Metallurgy, **21** (6):1049–1061.

Fjaer, H., Mortensen, D., Hakonsen, A., and Sorheim, E. 1999. Coupled Stress, Thermal and Fluid Flow Modeling of the Start-up Phase of Aluminum Sheet Ingot Casting. Light Metals 1999:743–748.

Grandfield, J. and McGlade, P. 1996. DC Casting of Aluminium: Process Behaviour and Technology. Materials Science Forum, **20**:29–51.

Grandfield, J., Easton, M., Davidson, C., StJohn, D., and Rinderer, B. 2005. The effect of grain refinement on hot tearing of AlMgSi Alloy 6060. Proceedings of the 2nd International Light Metals Technology Conference 2005: 8 - 10 June 2005, St. Wolfgang, Austria, (Editor) H. Kaufmann, ARC Leichtmetallkompetenzzentrum Ranshofen GMBH, 1003–1009.

Granger, D. 1998. Microstructure Control in Ingots of Aluminum Alloys with an Emphasis on Grain Refinement. Light Metals 1998:941–952.

Grasso, P. 2004. Coalescence and mechanical behaviour of semi-solid aluminium alloys in relation to hot tearing. Ph.D. thesis, EPFL, Lausanne.

Grealy, G.P., Davis, J.L., Jensen, E.K., Tondel, P.A., and Moritz, J. 2001. Advances for DC ingot casting: Part 1 - Introduction and metal distribution. Light Metals 2001:805–811.

Haaften, W.V., Magnin, B., Kool, W., and Katgerman, L. 2002. Constitutive behavior of As-cast AA1050, AA3104, and AA5182. Metallurgical and Materials Transactions A-Physical Metallurgy and Materials Science, **33** (7):1971–1980.

Hao, H., Maijer, D., Wells, M., Phillion, A., and Cockcroft, S. 2010. Modeling the Stress-Strain Behavior and Hot Tearing during Direct Chill Casting of an AZ31 Magnesium Billet. Metallurgical and Materials Transactions A, **41**:2067–2077.

Heymes, F., Commet, B., DuBost, B., Lassince, P., Lequeu, P., and Raynaud, G.M. 1997. Development of new Al alloys for distortion free machined aluminium aircraft components.

Jeng, S. and Chen, S. 1996. Determination of the solidification characteristics of the A356.2 aluminum alloy. Aluminium Alloys: their Physical and Mechanical Properties, Pts 1-3, **217**:283–288.

Jiang, H., Kierkus, W.T., and Sokolowski, J.H. 1999. Determining dendrite coherency point characteristics of Al alloys using single-thermocouple technique. AFS Transactions, **68**:169–172.

Lalpoor, M., Eskin, D., and Katgerman, L. 2009. Cold-Cracking Assessment in AA7050 Billets during Direct-Chill Casting by Thermomechanical Simulation of Residual Thermal Stresses and Application of Fracture Mechanics. Metallurgical and Materials Transactions A, **40**:3304–3313.

Larouche, A., Caron, Y., and Kocaefe, D. 1998. Impact of water heat extraction and casting conditions on ingot thermal response during DC casting. Minerals, Metals and Materials Society, 184 Thorn Hill Rd, Warrendale, PA 15086-7514 USA.

Li, S. 2010. Hot Tearing in Cast Aluminum Alloys: Measures and Effects of Process Variables. Ph.D. thesis, Worchester Polytechnic Institute.

Lin, S., Aliravci, C., and Pekguleryuz, N.I.O. 2007. Hot-tear susceptibility of aluminum wrought alloys and the effect of grain refining. Metallurgical and Materials Transactions A-Physical Metallurgy and Materials Science, **38A** (5):1056–1068.

Lu, Y.L., Li, M., and Li, X. 2008a. Experimental investigation and modelling of microstructural variables of Al-4Cu-Mg alloy. Materials Science and Technology - London, **24** (7):815–821.

Lu, Y.L., Li, M.Q., and Li, X.C. 2008b. Experimental investigation and modelling of microstructural variables of Al-4Cu-Mg alloy. Materials Science and Technology, **24** (7):815–821.

Ludwig, O., Drezet, J., Martin, C., and Suery, M. 2005a. Rheological behavior of Al-Cu alloys during solidification: Constitutive modeling, experimental identification, and numerical study. Metallurgical and Materials Transactions A-Physical Metallurgy and Materials Science, **36A** (6):1525–1535.

Ludwig, O., Drezet, J.M., Meneses, P., Martin, C., and Suery, M. 2005b. Rheological behavior of a commercial AA5182 aluminum alloy during solidification. Materials Science and Engineering: A, **413–414**:14–175.

Magnin, B., Maenner, L., Katgerman, L., and Engler, S. 1996. Ductility and rheology of an Al-4.5Cu alloy from room temperature to coherency temperature. Materials Science Forum, **217-222**:1209–1214.

Markoli, B., Boncina, T., and Zupanic, F. 2010. The Solidification Path of the Complex Metallic Al-Mn-Be Alloy RID A-5029-2008 RID A-7009-2009. Croatica Chemica Acta, **83** (1):49–54.

Mathew, J. and Brody, H. 1976. Analysis of Heat Transfer in Continuous Casting Using Finite Element Method. Nuclear Metallurgy, **20**:978–990.

Matsuda, K., Nagai, S., Miyate, Y., Maehara, H., and Tsukuda, I. 1996. Cold Cracking in DC Casting. Proceedings of Sixth International Aluminum Extrusion Technology Seminar: May 14-17, 1996, Chicago, Illinois, Aluminum Association and Aluminum Extruders Council (U.S.), 525–528.

M'Hamdi, M., Mo, A., Mortensen, D., and Fjaer, H. 2002. Modelling of air gap development and associated surface macrosegregation in DC casting of aluminium sheet ingots. Light Metals 2002:695–701.

Mirkovic, D., Grbner, J., and Schmid-Fetzer, R. 2008. Solidification paths of multicomponent monotectic aluminum alloys. Acta Materialia, **56** (18):5214 – 5222.

Mo, A. and Holm, E.J. 1993. On the use of Constitutive Internal Variable Equations for Thermal-Stress Predictions in Aluminum Casting (Reprinted from Journal of Thermal-Stresses, Vol 14, Pg 571-587, 1991). Modeling Identification and Control, **14** (1):43–58.

Mondolfo, L.F. 1976. Aluminum alloys: structure and properties. 1 edition, Butterworths, Waltham, Massachusetts, USA.

Moriceau, J. 1975. Thermal Stresses in DC Casting of Al Alloys. In Rentsch R,ed, Light Metals 1975:119–133.

Nadella, R., Eskin, D., Du, Q., and Katgerman, L. 2008a. Macrosegregation in direct-chill casting of aluminium alloys. Progress in Materials Science, **53** (3):421 – 480.

Nadella, R., Eskin, D., and Katgerman, L. 2008b. Effect of Grain Refinement on Structure Evolution, Floating Grains, and Centerline Macrosegregation in Direct-Chill Cast AA2024 Alloy Billets. Metallurgical and Materials Transactions A, **39**:450–461.

Nagaumi, H. 2001. Prediction of porosity contents and examination of porosity formation in Al-4.4Mg DC slab. Science and Technology of Advanced Materials, **2** (1):49.

Nagaumi, H., Aoki, K., Komatsu, K., and Hagisawa, N. 2000. Internal crack in DC casting billet of high strength Al-Mg-Si alloys. Aluminium Alloys: their Physical and Mechanical Properties, Pts 1-3, **331-3**:173–178.

Pellini, W. 1952. Strain Theory of Hot Tearing. Foundry:125–137.

Phillion, A., Lee, P., and Cockcroft, S. 2008. A three-phase simulation of the effect of microstructural features on semi-solid tensile deformation. Acta Materialia, **56**:4328–4338.

Phillion, A.B., Cockcroft, S.L., and Lee, P.D. 2009. Predicting the constitutive behavior of semi-solids via a direct finite element simulation: Application to AA5182. Modelling and Simulation in Materials Science and Engineering, **17** (5).

Prokhorov, N.N. 1962. Resistance to Hot Tearing of Cast Metals during Solidification. Russian Castings Production, **2**:172–175.

Rappaz, M., Drezet, J., and Gremaud, M. 1999. A new hot-tearing criterion. Metallurgical and Materials Transactions A, **30**:449–455.

Sengupta, J., Maijer, D., Wells, M.A., Cockcroft, S.L., and Larouche, A. 2001. Mathematical modelling of the thermomechanical behavior of a 5182 aluminum ingot during the start-up phase of the DC casting process: The role of bottom block. Light Metals 2001:879–885.

Sengupta, J., Maijer, D., Wells, M., Cockcroft, S., and Larouche, A. 2003. Mathematical modelling of water ejection and water incursion during the start-up phase of the DC casting process. Light Metals 2003:841–847.

Sengupta, J., Cockcroft, S.L., Maijer, D.M., Wells, M.A., and Larouche, A. 2004. On the development of a three-dimensional transient thermal model to predict ingot cooling behavior during the start-up phase of the direct chill-casting process for an AA5182 aluminum alloy ingot. Metallurgical and Materials Transactions B: Process Metallurgy and Materials Processing Science, **35** (3):523–540.

Sengupta, J., Cockcroft, S., Maijer, D., and Larouche, A. 2005a. Quantification of temperature, stress, and strain fields during the start-up phase of direct chill casting process by using a 3D fully coupled thermal and stress model for AA5182 ingots. Materials Science and Engineering A-Structural Materials Properties Microstructure and Processing, **397** (1-2):157–177.

Sengupta, J., Thomas, B., and Wells, M. 2005b. The use of water cooling during the continuous casting of steel and aluminum alloys. Metallurgical and Materials Transactions A-Physical Metallurgy and Materials Science, **36A** (1):187–204.

Singer, A. and Cottrel, S. 1946. Properties of the Al-Si Alloys at temperatures in the region of the solidus. Journal Institute of Metals:33–54.

Stefanescu, D. 1988. The new metals hand book:Volume 15, Casting. ASM International.

Suyitno 2005. Hot Tearing and Deformation in Direct Chill Casting of Aluminum Alloys. Ph.D. thesis, Delft University of Technology.

Suyitno, Kool, W., and Katgerman, L. 2002. Micro-Mechanical Model of Hot Tearing at Triple Junctions in DC Casting. Materials Science Forum, **396 - 402**:179–184.

Suyitno, Kool, W., and Katgerman, L. 2005. Hot tearing criteria evaluation for direct-chill casting of an Al-4.5 Pct Cu alloy. Metallurgical and Materials Transactions A-Physical Metallurgy and Materials Science, **36A** (6):1537–1546.

Thevoz, P., Gaumann, M., and Gremaud, M. 2002. The Numerical Simulation of Continuous and Investment Casting. Journal of Materials - e.
URL: *http://www.tms.org/pubs/journals/jom/0201/thevoz/thevoz-0201.html*

Thompson, S., Cockcroft, S., and Wells, M. 2004. Effect of cooling rate on solidification characteristics of aluminium alloy AA5182. Materials Science and Technology, **20** (4):497–504.

Twite, M., Spittle, J., and Brown, S. 2004. The Tensile Properties of Semi-Solid Aluminum Alloys. International Journal of Forming Processes, **7** (1-2):233–260.

Veldman, N.L.M., Dahle, A.K., John, D.H.S., and Arnberg, L. 2001. Dendrite coherency of Al-Si-Cu alloys. Metallurgical and Materials Transactions A-Physical Metallurgy and Materials Science, **32** (1):147–155.

Weckman, D.C. and Niessen, P. 1982. A Numerical-Simulation of the Dc Continuous-Casting Process Including Nucleate Boiling Heat-Transfer. Metallurgical Transactions B-Process Metallurgy, **13** (4):593–602.

Williams, A., Croft, T., and Cross, M. 2003. Modeling of ingot development during the start-up phase of direct chill casting. Metallurgical and Materials Transactions B, **34**:727–734.

Wiskel, J.B. and Cockcroft, S.L. 1996. Heat-flow-based analysis of surface crack formation during the start-up of the direct chill casting process .1. Development of the inverse heat-transfer model. Metallurgical and Materials Transactions B-Process Metallurgy and Materials Processing Science, **27** (1):119–127.

Won, Y., Yeo, T., Seol, D., and Oh, K. 2000. A new criterion for internal crack formation in continuously cast steels. Metallurgical and Materials Transactions B-Process Metallurgy and Materials Processing Science, **31** (4):779–794.

Yamanaka, A., Nakajima, K., Yasumoto, K., Kawashima, H., and Nakai, K. 1992. New Evaluation of Critical Strain for Internal Crack Formation in Continuous-Casting. Revue De Metallurgie-Cahiers D Informations Techniques, **89** (7-8):627–633.

Yu, K.O. 2002. Modeling for casting and solidification processing. Marcel Dekker, New York, iD: 48056320.

Zheng, X.W., Dong, J., Zhou, N., Fu, P.H., Yao, S.S., and Ding, W.J. 2011. Effect of process parameters on structure and macrosegregation upon direct chill casting of Mg-Nd-Zn-Zr alloy. Materials science and technology, **28**:275–281.

Zhi-ming, D., Gang, C., Jun, L., and Shui-sheng, X. 2010. Tensile properties of as-deformed 2A50 aluminum alloy in semi-solid state. Transactions of Nonferrous Metals Society of China, **20** (9):1597–1602.